AERODYNAMIC ANALYSIS OF VERTICAL AND HORIZONTAL AXIS WIND TURBINES

By

Anwelli Soala Okpue

A THESIS

Submitted to
Michigan State University
in partial fulfillment of the requirements
for the degree of

MASTER OF SCIENCE

Mechanical Engineering

2011

ABSTRACT

AERODYNAMIC ANALYSIS OF VERTICAL AND HORIZONTAL AXIS WIND TURBINES

By

Anwelli Soala Okpue

The power generated by horizontal axis and vertical axis wind turbines is strongly dependent on the aerodynamic performance of the turbines. This includes the lift and drag forces generated by the individual blades and interactions between them in a rotating configuration; as well the aerodynamic effects of the turbine's structure and the terrain. To maximize the efficiency of wind turbines, experimental and computation analysis of the blade and system is normally needed. This research is part of larger efforts at Michigan State University to develop sustainable low speed wind energy systems and is focused on the aerodynamic modeling of vertical and horizontal axis wind turbines. The main objective is to better understand the effects of various parameters on the performance of these turbines. A computational model was developed as part of this research for studying the aerodynamics of vertical axis turbines. The model is refined via experimental data and other computational results available in literature. A parametric study was conducted with this model. The effects of parameters like the tip speed ratio, airfoil shape/type, Reynolds number are investigated in detail. The aerodynamics of variable pitch vertical axis wind turbines is also studied. Our results indicate that a significant improvement in aerodynamic efficiency of vertical axis wind turbines is possible by variable pitching.

ACKNOWLEDGMENTS

I would like to express my sincerest gratitude to those who made this work possible. My thanks go out to the Department of Mechanical Engineering at Michigan State University for the financial support provided during the course of my study and research efforts. I am very grateful to my Graduate Advisor, Dr. Farhad Jaberi for his wisdom, enthusiasm, and patience. Also for the countless other advice I have received from him in developing me professionally and personally. I will also like to thank the members of my Graduate Advisory Committee, Drs. Farhang Pourboghrat and Brian Feeny, for their helpful advice and suggestions. I especially wish to thank my Dad for his courage and support, my Mom for her continued prayers and encouragement, and my brother, Nduka for always being there for me in his special way, my extended family and friends, especially Bola Ndifontah, for their faith, support, and encouragement. Finally, and most of all, I thank my Lord and Redeemer, Jesus Christ, in Whom, by Whom, and for Whom I and all things consist.

Table of Contents

List of Tables

List of Figures

Chapter 1: Introduction

Currently wind turbines generate less than 2% of the total electric energy in the US. The DOE aims to produce 20% of electric energy used in the US from wind in the next few decades. This represents more than a tenfold increase in production, and it will require extensive investments as well as research and development in wind turbines, energy storage systems and electric grid integration techniques. These machines have economic incentives, as well as reducing the US's energy dependence on fossil fuels which both pollutes the atmosphere, and are neither renewable nor sustainable. Sustainability issues arise because as societies grow, there is a corresponding increase in energy consumption. In addition, the supply of fossil fuels is subject to other external factors such as politics and other world events, thus creating an issue of national security. In order to meet this goal of energy independence, it is important to produce more efficient turbines which can compete with other forms of energy production systems, and that is why this research is necessary.

There are two general configurations of wind turbines: horizontal axis wind turbine (HAWT) and vertical axis wind turbine (VAWT). Within these classifications there are various designs that have been proposed over the years. As the name implies, the HAWT has its main shaft (i.e. the shaft which connects the rotor to the generator) in the horizontal axis. These turbines are made of several blades (two or more) erected atop a tower with all the main components (generator, gear-box, controls) sitting at the top of the tower. The HAWT can also be classified as either upwind or downwind turbines. The difference being that the rotor blades are oriented either facing or backing the wind. The VAWT configuration has its main shaft oriented in a vertical direction. For this turbine, the main components are at ground level. Modern VAWTs have three main types: Darrieus type, H-Rotor type, and Savonius type turbines. The Darrieus and H-Rotor type

turbines are lift force driven turbines, as they rely on the generation of a lift force on their blades to generate torque which is converted to power by the generator. Savonius type turbines on the other hand are drag force driven turbines. These turbines are essentially two cups or half-drums, oriented in opposing directions and connected to a central shaft. One cup catches the wind, rotates the shaft and brings the opposing cup into the wind's direction which further turns the shaft, thus forming a couple moment. As this process is repeated by the incoming wind, torque is generated which can then be used to do work.

In general, lift type turbines are more efficient that drag type turbines. Power coefficient for lift turbines vary between 30% and 45%, while drag type turbines are usually not above 25%. These types of turbines are suitable for low torque applications and they are commonly used for wind speed instruments such as wind vanes or anemometers (Kirke 1998) ; i.e. applications where efficiency is not the primary concern.

Currently, HAWTs are the most prevalent type of wind turbines being used all over the world to generate electricity (both onshore and offshore). VAWTs are the less commonly used systems; they have primarily been used to generate small amounts of power (in the order of kilowatts). The major reason for VAWTs being less prevalent is the fact that they are known to have lower maximum efficiencies compared to HAWT. Table 1-1 compares the advantages and disadvantages of HAWTs and VAWTs.

Table 1-1: Comparing HAWT and VAWT by highlighting their advantages and disadvantages

Horizontal Axis Wind Turbine (HAWT)	
Advantages	• Higher efficiency due to variable blade pitching capability. • Established manufacturing know-how and market acceptability.
Disadvantages	• Increased costs associated with transportation of tall towers and long blades. • Installation requires very tall and expensive cranes, and skilled operators. • Massive tower and heavy foundation required to support blades, gearbox, and generator. • Complex design of twisted blades is difficult and expensive to fabricate. • Large size may disrupt the landscape and create local opposition. • Requires yaw control to turn the blades and nacelle toward the wind. • A distance of 5 rotor diameters siting is needed in order to minimize wake effects. • Difficult, expensive, and frequent maintenance required.

Table 1-1 (cont'd)

Vertical Axis Wind Turbine (VAWT)	
Advantages	• Smaller tower and support structure, since bearings are mounted near the ground. • The generator and gearbox are installed near the ground which reduces the cost of the foundation and support structure. • Suitable for low speed winds, due to lower wind startup speed. • May be built at locations where tall structures are prohibited. • Can take advantage of locations where landscape increases wind speed near the ground. • May have a lower noise signature. • Needs less space than HAWT to generate the same amount of power. • Straight blades are much easier and economical to fabricate or extrude. • Lower overall maintenance and transportation costs.
Disadvantages	• Lower aerodynamic efficiency compared to HAWT. • Blade fatigue failure due to change in stress sign during each revolution. • May require dismantling the entire structure to fix the generator or gearbox.

To enhance the performance of wind turbines, either a taller tower or a larger rotor must be used. However, roughly speaking, tower costs increase with the height to the fourth power, while the

rotor costs increase with diameter cubed; meanwhile rotor power grows only with the diameter squared (Jose 2010). The challenge is therefore to improve the efficiencies and power of the current existing systems without growing the production, installation and transportation costs.

This research intends to explore the aerodynamics of wind turbines by using computer models. The focus is on VAWTs. For aerodynamic analysis of HAWTs, FAST (Fatigue, Aerodynamics, Structure and Turbulence) is used. This computer code was developed by National Renewable Energy Laboratory (NREL) for studying two or three bladed turbines. For VAWTs, a computational model I developed based on the cascade theory is used.

Chapter 2 describes the computational/ empirical models commonly used for the aerodynamic analysis of wind turbines. They include the streamtube momentum models, the vortex model and the cascade model. Details of the model used in this research are presented, and its implementation is discussed. *Chapter 3* presents the results involving the model/ code validation. Additionally, in this chapter results describing the effects of various parameters on the performance of VAWT are presented. The effects of parameters such as: Reynolds number, airfoil shape, solidity, and wind shear are considered. Issues related to torque and self-start are also discussed. *Chapter 4* explores how a variable blade pitching technique can be used to improve the turbine's performance, as well as to resolve the problem of self-start associated with VAWTs. A parametric study is also performed for the HAWTs and the results presented in *Chapter 5.* Conclusions and recommendations concerning the operation, and optimization of VAWT and HAWT are given in *Chapter 6.*

Chapter 2: Theory

2.1 VAWT

In this section the analytical/ computational models employed for VAWT and HAWT are described.

The model used in this research for the aerodynamic analysis of VAWTs is based on the ***Cascade Theory.*** This theory is widely used in the field of turbomachinery for calculating the dynamic forces induced by the flow over blades in turbines and compressors. The cascade refers to an array of blades around the hub of the rotor. The model assumes the airfoils to be unwrapped into an array of blades having uniform pitch and spacing between them (see Figure 2-1). In turbomachinery applications, this modeling approach has been used to map pressure and velocity distributions over the airfoils passages, and to obtain other basic quantities and characteristics that are required in turbomachinery studies, such as: the inlet flow angle, mach number, true Reynolds number, etc. Also since the unwrapped configuration simplifies the problem, it is suitable for design purposes as well as carrying out parametric studies.

The use of cascade theory for vertical axis wind turbine simulation was first proposed by Hirsch and Mandal (Hirsch and Mandal 1987). Figure 2-2 shows the blade array configuration used to simulate a three blade VAWT. Based on the theory, the particular type of cascade configuration being used is a linear or rectilinear cascade. In computer simulation the cascade of blades are represented as airfoils with the same shape, vis-à-vis the same aerodynamic properties such as lift, drag and pitching moments.

The cascade theory as applied to VAWT further simplifies the problem by considering one of the blades as the reference blade, and by assuming the flow conditions on other blades to be equal to

that on the reference blade. To investigate the relationship between blade forces (forces which are generated due to energy exchange from the fluid to the turbine) and the flow properties, a control surface is drawn around each airfoil with two identical streamlines along the longitudinal lengths of the airfoil, and two parallel lines in front and behind the airfoil; the two parallel lines form the upstream and downstream of the blade and represent the inlet and outlets of the control surface. The continuity and momentum equations are applied to the control volume (Scholz. n.d.). Details of the theory are given in a later section.

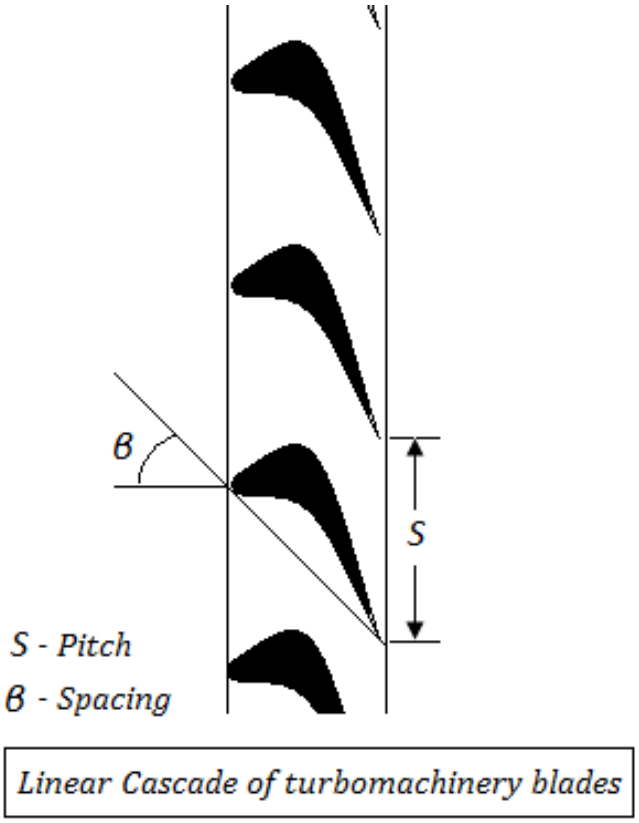

Figure 2-1: The general configuration of a linear cascade model (Swamy and Kumaran 2009)

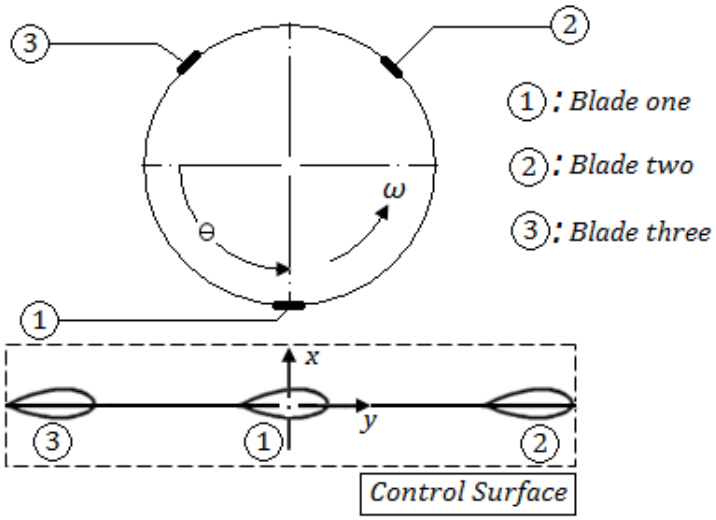

Figure 2-2: The orientation of blades in the linear cascade model for a VAWT

2.1.1 Other Simulation Models

Blade Element Momentum (BEM) Model - A popular simulation model for VAWT is the Blade Element Momentum (BEM) model. This model is the basis of various models such as: Single Streamtube Model (Templin 1974) , Multiple Streamtube Model (Wilson and Lissaman 1974), and the Double-multiple Streamtube Model (I. Paraschivoiu 1981). In these models, the flow velocities induced by the turbine blades in the flow's path is obtained based on the principle of conservation of momentum. The aerodynamic forces are tied to the momentum exchange and are calculated as the rate of change of momentum of the fluid, i.e. the overall change in velocity multiplied by the mass flow rate. The *Actuator Disk Theory* is then applied for computing the turbine/ flow variables.

Actuator Disk Theory - The aim of a turbine in the wind's path is to extract kinetic energy from the wind. To model this extraction an actuator disk is placed in the flow's path. The actuator disk is simply a plane in the wind's path over which changes in velocity and pressure can be

represented. The concept of the actuator disk theory is more intuitively understood for horizontal axis wind turbines which when viewed from a plan or side view have the form of a "disk" in the flow's path (see Figure 2-3). This disk is surrounded by a streamtube which is an imaginary tube around the disk; only the air flowing through the tube is considered in the analysis. Upstream of the disk the streamtube has a cross-sectional area smaller than that of the disk and an area larger than the disk in the downstream. The mass flow rate is the same everywhere, i.e.:

$$\rho_\infty A_\infty V_\infty = \rho_d A_d V_d = \rho_w A_w V_w \qquad \text{Eq. 2.1}$$

In the above equation, subscripts "∞", "*d*", and "*w*" represent quantities upstream of the disk, at the disk, and in the wake downstream of the disk. The velocity change experienced by the air as it passes through disk is equated to the rate of change of momentum; this rate of change of momentum is representative of the aerodynamic force used to rotate the turbine.

In the HAWT, this tube in broken up into various annular sections and analysis is carried out over these sections. For applying the actuator disk theory to a VAWT, the disk is oriented in the horizontal direction. The entire height of the turbine is broken into equal segments, and a separate actuator disk is applied to each segment. A streamtube is also drawn around the circular path traced by the turbine as shown in Figure 2-4. In the case of a multiple streamtube model the streamtube surrounding the turbine, is divided into smaller rectangular "streamtubes" stretched over the diameter of the turbine (Figure 2-5) (similar to the annular section of the HAWT). Here the term streamtube refers to the rectangular strips. These streamtubes are fixed, and the turbine blade is assumed to rotate around a circular path, cutting these streamtubes. Whenever the blade cuts the stationary streamtube, the actuator disk theory is applied to solve for the momentum change and force.

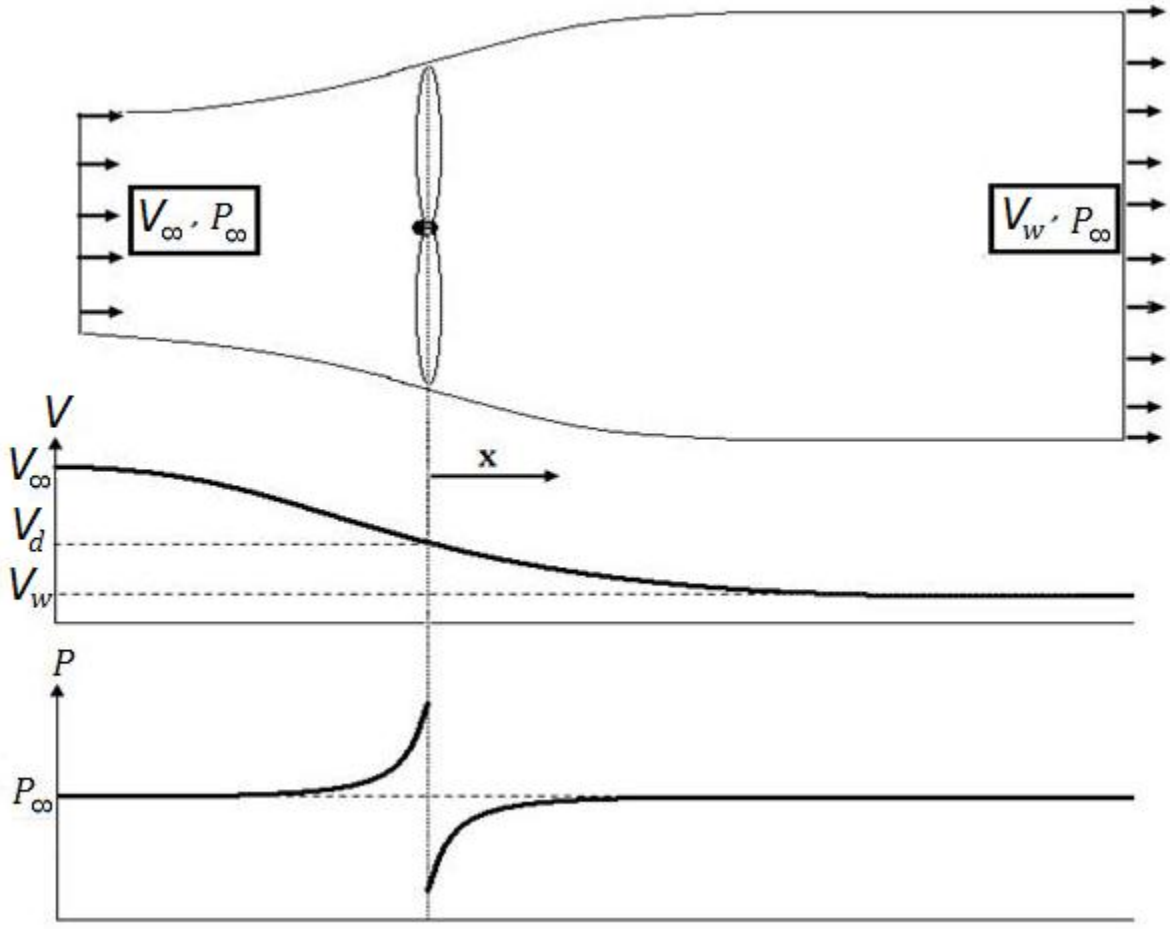

Figure 2-3: The side view of the streamtube around the actuator disk for a HAWT (dashed line drawn through the blade) and the velocity and pressure distribution upstream and downstream of the disk

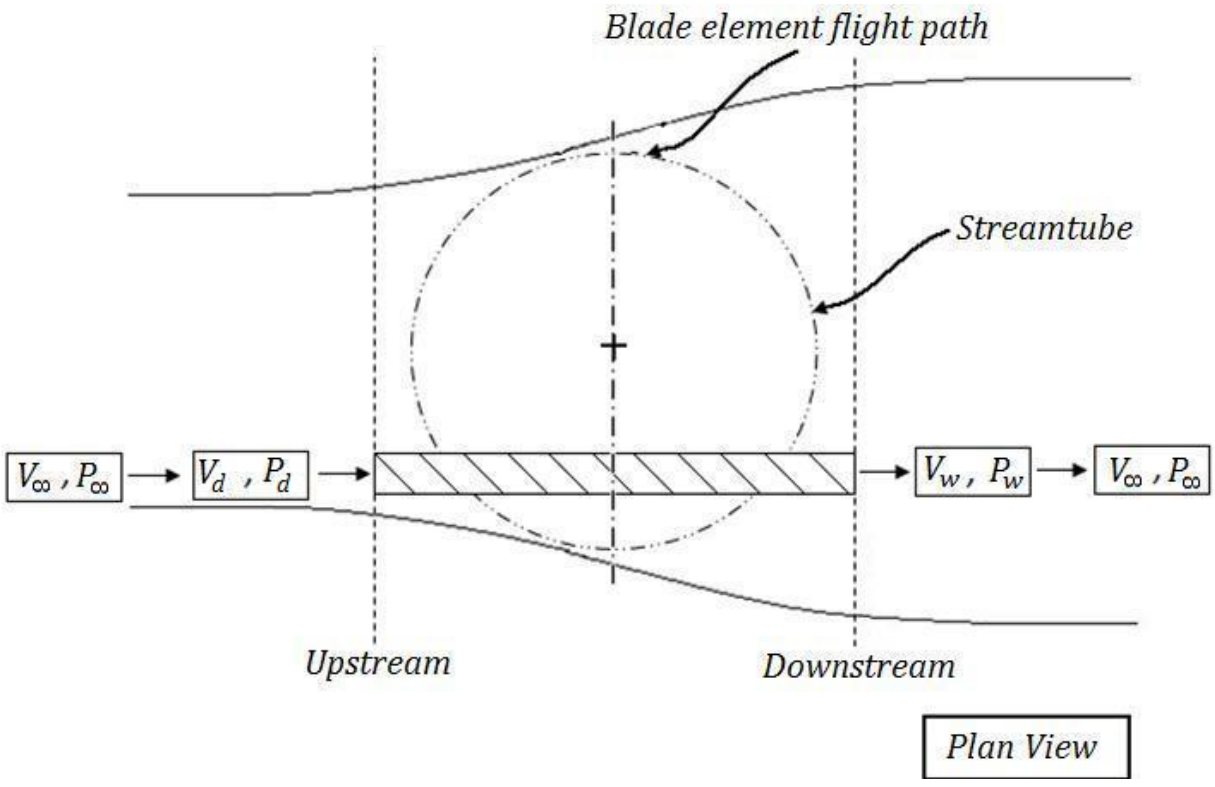

Figure 2-4: A typical streamtube used in the analysis of VAWTs

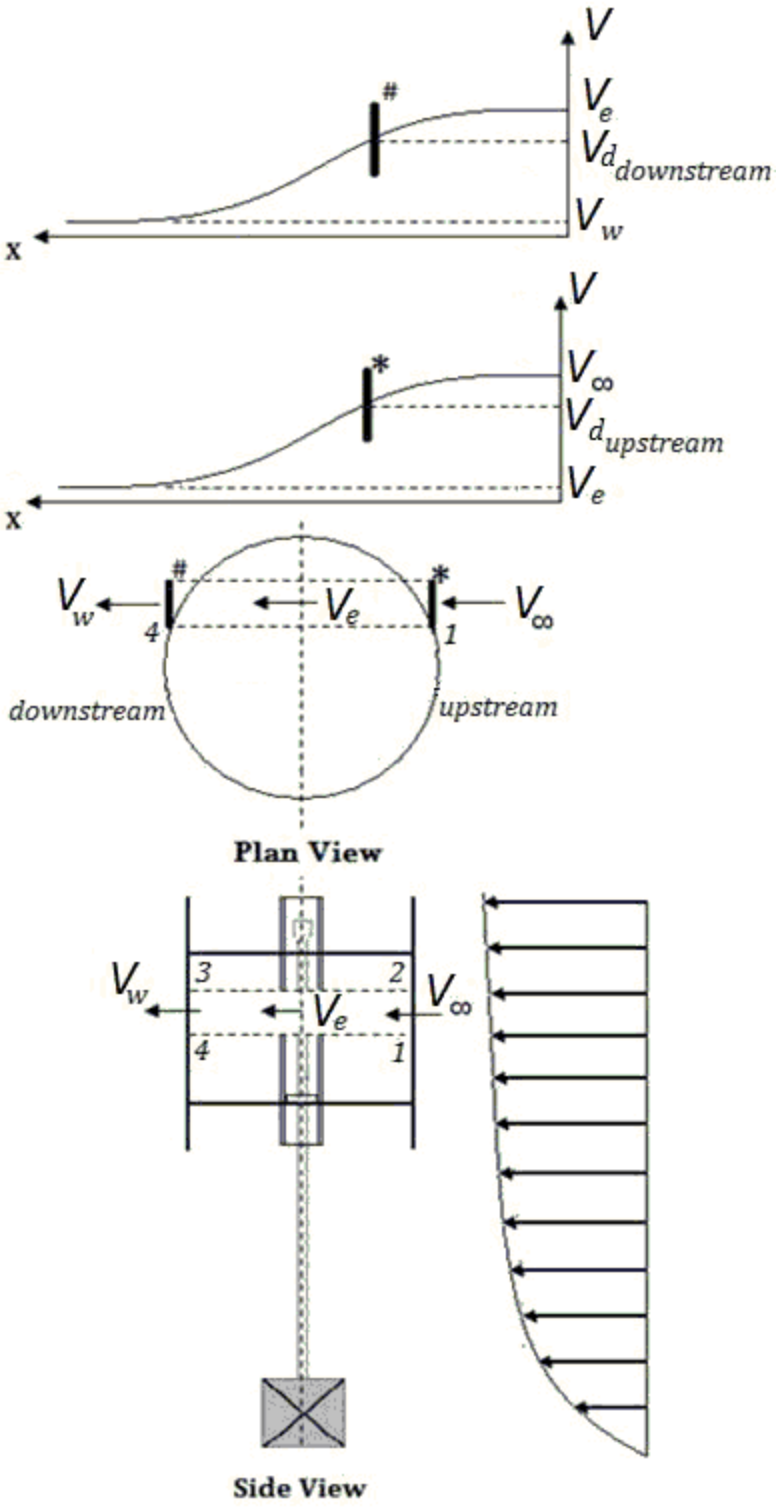

Figure 2-5: Rotor element replaced by the actuator disk

The multiple streamtube model is a modification of an earlier single streamtube model, and it was introduced because of the shortcomings of the earlier model. The earlier version was sufficient in predicting the performance of a very lightly loaded wind turbine. However, it always predicts higher power when compared to experimental results. It also does not adequately predict the wind velocity variations across the rotor (Islam, S.K. and Ting 2008). It was conceived that, by dividing the single streamtube into multiple streamtubes along the diameter of the turbine, the predictive capabilities could be improved. From the results obtained, it has been confirmed that better comparisons to experimental data were achieved by applying this model.

To perform the analysis via the double multiple streamtube model, the turbine is broken up into two sections: the upstream and downstream sections. The free-stream velocity is the input for the upstream section, and the wake velocity calculated from this section is used as the input to calculate the variables in the downstream section. The general simulation procedure then follows similar methodologies as with other streamtube models.

General Momentum Theory as Applied for Wind Turbines - The air that goes through the streamtube undergoes an overall change in velocity, $V_\infty - V_w$, and therefore the rate of change of momentum is equal to this change in velocity multiplied by the mass flow rate.

$$\textit{Rate of change of momentum} = (V_\infty - V_w)\rho A_{cs} V_d \qquad \text{Eq. 2.2}$$

where V with subscript *"∞"*, *"d"*, and *"w"* represents the velocity at points in the free-stream, at the turbine, and in the wake of the flow; also A_{cs} is the cross-sectional area of the disk and ρ is the density of the fluid. The force causing this change of momentum comes entirely from the pressure difference across the actuator disk because the system is otherwise completely

surrounded by air at atmospheric pressure which produces a net zero force (Burton, et al. 2001). Therefore,

$$(P_d^+ - P_d^-)A_{cs} = (V_\infty - V_w)\rho A_{cs} V_d \qquad \text{Eq. 2.3}$$

To obtain the pressure difference$(P_d^+ - P_d^-)$, the Bernoulli's equation is applied for a streamline over the length of a rectangular streamtube at its inlet and outlet. At the inlet we have,

$$\tfrac{1}{2}\rho_\infty V_\infty^2 + \rho_\infty g h_\infty = \tfrac{1}{2}\rho_d V_d^2 + P_d^+ + \rho_d g h_d \qquad \text{Eq. 2.4}$$

Assuming the flow to be incompressible ($\rho_\infty = \rho_d$) and horizontal ($h_\infty = h_d$) then,

$$\tfrac{1}{2}\rho V_\infty^2 + P_\infty = \tfrac{1}{2}\rho V_d^2 + P_d^+ \qquad \text{Eq. 2.5}$$

Similarly, at the outlet of the streamtube,

$$\tfrac{1}{2}\rho V_w^2 + P_\infty = \tfrac{1}{2}\rho V_d^2 + P_d^- \qquad \text{Eq. 2.6}$$

Subtracting these equations we obtain:

$$(P_d^+ - P_d^-) = \tfrac{1}{2}\rho(V_\infty^2 - V_w^2) \qquad \text{Eq. 2.7}$$

From Equation 2.3,

$$\tfrac{1}{2}\rho(V_\infty^2 - V_w^2)A_{cs} = (V_\infty - V_w)\rho A_{cs} V_d \qquad \text{Eq. 2.8}$$

Therefore, we have:

$$V_w = (1-2a)V_\infty \qquad \text{Eq. 2.9}$$

where the axial induction factor, *a*, is given as:

$$a = 1 - \frac{V_d}{V_\infty} \qquad \text{Eq. 2.10}$$

The axial induction factor is a non-dimensional quantity which is used during simulation to express the decrease in velocity from the free-stream at the rotor.

The force the turbine exerts on the air becomes:

$$F = (P_d^+ - P_d^-)A_{cs} = 2\rho A_{cs} V_\infty^2 a(1-a) \qquad \text{Eq. 2.11}$$

This force is that at the actuator disk and is related to the power extraction at this location. The force extraction is concentrated at the actuator disk, with the characteristic velocity V_d. After the geometries and initial conditions have been specified an initial guess is made for the induction factor, *a*, after which the various variables are calculated. Using an iterative approach the process is repeated until the results converge. Details of the method can be found elsewhere in R. Templin 1974, Strickland 1976, and I. Paraschivoiu 1981.

Vortex Model - The vortex model is based on the potential theory of lifting bodies. The potential theory is used to calculate the amount of circulation on the blade span, which by the Kutta-Joukowski theorem (Equation 2.13) can be related to the lift on the blade; the theory prescribes that the aerodynamic lift generated on the blade is due to the bound vorticity distributions (Brownlee n.d.). This model is based on the assumption that the induced velocity field is due to the combined effects of the bound and wake vorticity distribution. The bound vorticity distribution results from the distribution of circulation on the blade due to the vorticity

contained in the boundary layers of the wing. The wake vorticity distribution results from the distribution of circulation in the wake of the blade section. The shed wake vorticity ultimately stems from the bound vorticity distribution which flows from the blade tips. This model breaks the entire turbine into nodes.

In applying the model, we start by finding the fluid's relative velocity, $\vec{V}_r$. This relative velocity is due to the presence of three velocity components: the free-stream, $\vec{V}_\infty$, the rotational velocity, $R\omega\vec{e}_t$, and the induced velocity, $\vec{V}_i$, produced by the bound and wake vorticity distribution:

$$\vec{V}_r = \vec{V}_\infty - R\omega\vec{e}_t + \vec{V}_i \qquad \text{Eq. 2.12}$$

The first two velocities are known inputs, so the key to using this method is calculating the induced velocity, $\vec{V}_i$. At the first iteration, the induced velocity is set to zero at every node, and the relative velocity is calculated based on the free-stream, and the rotational velocity. Along with the relative velocity, the angle of attack is calculated, and by using the C_L and C_D data obtained by experiment for a specific airfoil, the lift force can be calculated. Then by applying Equation 2.13, the bound vorticity distribution is obtained and used to find the trailing wake vorticity distribution. With these variables found, the induced velocity can be updated, and the iteration proceeds until the convergence of vorticity distribution.

$$L = \rho h V_\infty \Gamma \qquad \text{Eq. 2.13}$$

2.1.2 Cascade Theory as Applied for VAWT Simulation

The cascade theory at its core is based on the momentum principle; it however incorporates some of the ideas of potential theory. Recall that a turbine is used to extract energy from the flowing

fluid in order to utilize this energy to do useful work, i.e. generate electricity. Drag forces on aerodynamic bodies tend to reduce the amount of energy that is transferred from the fluid to the body hence making them less efficient; as a result the work generated by such forces (drag) are considered losses. Therefore for lift driven turbines the aim is to reduce this energy loss on the rotating aerodynamic components that aid power generation. For such systems we always want to foster a large enough lift force which produces torque.

To achieve this objective most modern wind turbines are made of airfoils. When the airfoil moves relative to air, the air follows the curvature of the airfoil's profile and is accelerated downwards. The result of this downward acceleration is the pressure increases under the airfoil and the pressure decreases above it. At this early development of the flow, the fluid mass tries to curl around the pointed trailing edge from the bottom surface to the top surface as shown in Figure 2-6. A consideration of inviscid, incompressible flow indicates that the theoretical velocity becomes very large at sharp corners. A stagnation point develops on the upper surface of the profile towards the trailing edge, along with a very strong vortical structure, known as the *starting vortex*, see Figure 2-7. The strength of this structure is obtained from the sharp velocity gradients being formed due to the tendency of the flow to curl upwards, and the net downward flow over the airfoil. However, these conditions cannot exist for an extended period of time, so in an actual flow the stagnation point on the top surface moves further towards the trailing edge. In addition to eliminating the starting vortex from the profile, a circulation, Γ, must be created about the airfoil profile which has equal strength but opposite in direction when compared to the starting vortex. According to Thomson's theory, the circulation does not change in time. This circulation is important so that the bifurcation streamline is displaced until it occurs at the trailing edge. The condition that allows smooth flow to form around the airfoil's trailing edge is

known as the Kutta's trailing edge condition. This stage of flow development is illustrated in Figure 2-8. The final step in lift generation comes after the initial transient process dies out, and the steady flow is reached. The circulation which causes this kind of flow also increases the flow velocity at the upper airfoil surface, and a corresponding reduction in the lower surface's velocity; in accordance with Bernoulli's equation this corresponds to a low pressure distribution on the top surface and higher pressures on the lower surface, so that a net upward resultant force with a line of action perpendicular to the relative flow direction is formed. This resultant force is the lift that is used to drive the turbine. The lift generated by the airfoil can be related to the amount of circulation via the Kutta – Jourkowski theorem (as given in Equation 2.13):

$$L = \rho h V_{\infty} \Gamma \qquad \text{Eq. 2.14}$$

The flow visualizations obtained from PIV data (Anderson Jr. 2001) confirm the evolution of flow illustrated in Figure 2-6 to Figure 2-8.

Figure 2-6: Early development of flow around an airfoil

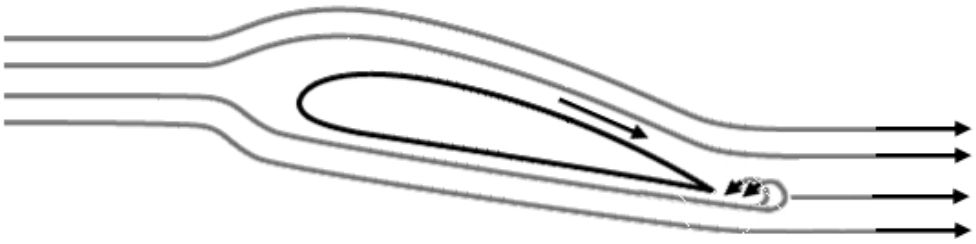

Figure 2-7: Development after the starting vortex has been formed

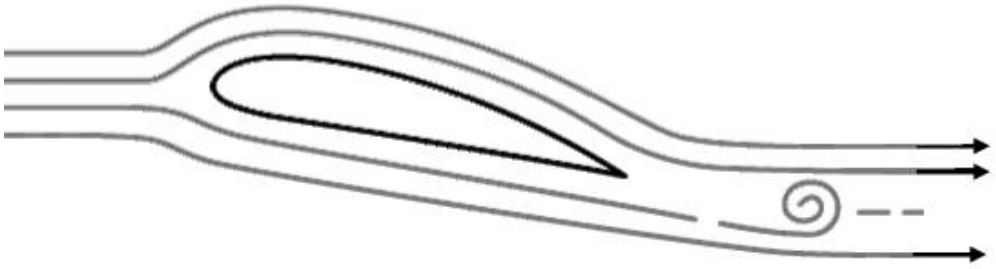

Figure 2-8: Smooth flow over the airfoil

A key point in understanding the cascade model is to understand how circulation is generated. Consider an arbitrary inviscid, incompressible flow over an airfoil starting from rest (hence no initial aerodynamic forces). The circulation around path C_1 at a given time t_1 is defined as $\Gamma_1 = -\oint_{C_1} \vec{V} \cdot \vec{ds}$. As the fluid elements within C_1 move downstream, at a later time, t_2, they form another curve, C_2, around which the circulation is $\Gamma_2 = -\oint_{C_2} \vec{V} \cdot \vec{ds}$. These fluid elements have the same amount of energy and circulation at t_1 and t_2. A flow at rest has zero velocity everywhere, and hence circulation around curve C_1 is zero. Figure 2-9 shows path C_2 at a later time downstream of the flow field after a smooth steady flow over the airfoil has been established. The fluid elements within C_2 are the same as those in C_1, however, because of the influence of the flow field, the path C_2 is different and is made of points *abcda* as shown in Figure 2-9. Kelvin's theorem gives the rate of change of circulation of a path from one location to another. According to this theorem, the circulation, Γ_2, within C_2 (which forms a closed path around the airfoil and the starting vortex) is the same as those in C_1. Since the airfoil was at rest

initially, i.e. a non-lifting surface with a circulation of zero around C_1; then based on Kelvin's theorem, $\Gamma_2 = \Gamma_1 = 0$. Now let C_2 be divided into two parts: C_4 a curve formed by points *abda* (around the airfoil) and C_3 a curve formed by tracing points *bcdb* (around the starting vortex). The circulation around the starting vortex is Γ_3, and Γ_4 is the circulation around the airfoil. By observation, the direction of Γ_3 is in the counterclockwise direction to the circulation around the airfoil. The circulation in C_4 is what we are interested in, and is the one that generates the lift. However, since C_3 and C_4 are made from one curve, C_2, the value of Γ_4 can be simply found from the equation: $\Gamma_3 + \Gamma_4 = \Gamma_2$. Since it has been established that Γ_2 is equal to zero, we can conclude that $\Gamma_4 = -\Gamma_3$, i.e. the circulation around the airfoil is equal and opposite to the that around the starting vortex.

In summary, a circulation equal in magnitude and opposite in direction to the circulation around the starting vortex has to be formed around the airfoil to ensure that the overall value of circulation is maintained.

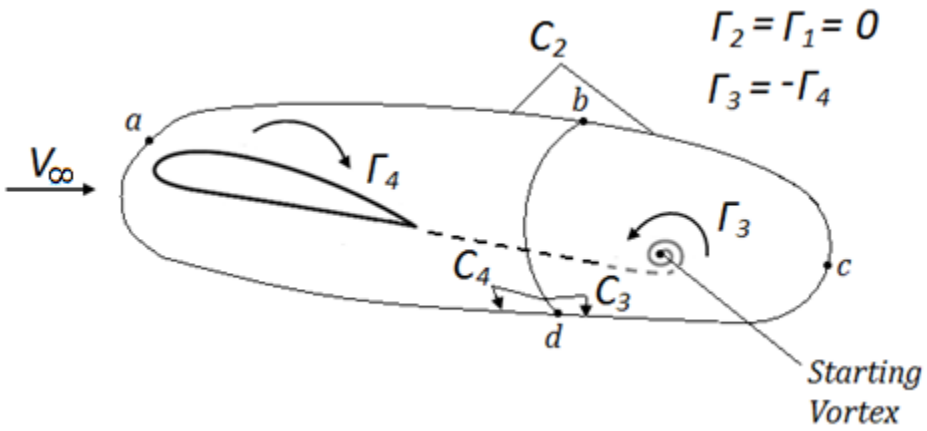

Figure 2-9: The curve C_2 around the airfoil involving points *abcda* (Anderson Jr. 2001)

The first step taken in modeling using the cascade theory is that, for any turbine with *N* number of blades, a reference blade is selected, and based on the free-stream velocity, RPM, and angular position, the angle of attack, α, and local relative velocity, W_0, are calculated as:

$$\alpha_0 = \tan^{-1}\left[\frac{\sin\theta\cos\phi}{\mu\left(\frac{R\omega}{V_\infty}/\frac{V_d}{V_\infty}\right)+\cos\theta}\right] \qquad \text{Eq. 2.15}$$

$$\frac{W_0}{V_\infty} = \frac{V_d}{V_\infty}\sqrt{\left[\mu\left(\frac{R\omega}{V_\infty}/\frac{V_d}{V_\infty}\right)+\cos\theta\right]^2+\sin^2\theta\cos^2\phi} \qquad \text{Eq. 2.16}$$

V_d in the equations above represents the induced velocity at the turbine blade, ω is the rotational speed of the turbine, R is the radius at the equatorial plane of the turbine, μ is the non-dimensional turbine radius (*r*/*R*) (*r* is the radius from the turbine axis to the local blade element), Θ is the angular position of the blade element, and ϕ is the blade angle normal to the equatorial plane. The calculations are performed on one of the blades (the reference blade), after the turbine has been unwrapped into the cascade configuration as shown in Figure 2-10.

The characteristics of blades 2 to N are assumed to be similar to those of the reference blade (assume blade one). For the control surface around the reference blade (Figure 2-11), the inflow, W_1, and outflow, W_2, velocities are the velocities calculated from W_0 and V_Γ (velocity due to circulation). We use W_1 and W_2 to compute the tangential force:

$$\delta F = \dot{\delta m}\left(W_1 \cos\alpha_1 - W_2 \cos\alpha_2\right) \qquad \text{Eq. 2.17}$$

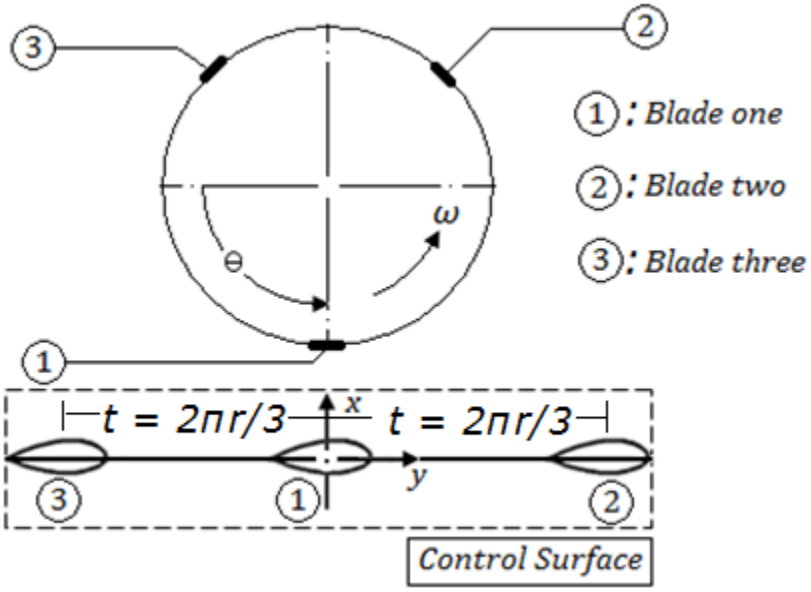

Figure 2-10: The unwrapped configuration of the turbine in the cascade theory

Equation 2.17 is simply an expression of the momentum balance which relates the force to the change in velocity. In addition, the elemental mass flow rate balance is given as: $\dot{\delta m} = \rho t W_1 \sin\alpha_1 \delta s = \rho t W_2 \sin\alpha_2 \delta s = \rho t W_x \delta s$. "*t*" represents the blade spacing, i.e. the ratio between the number of blades and the radius of the turbine ($2\pi r$/N) and δs represents the incremental height of the blade element under consideration.

Circulation around the blade profile is defined as the integral of the velocity vector:

$$\Gamma = \oint_s \vec{w} \cdot d\vec{s} \qquad \text{Eq. 2.18}$$

where "*w*" represents the velocity vector. The cascade theory models the circulation around the airfoil as the integral around the path *abcd* (Figure 2-12).

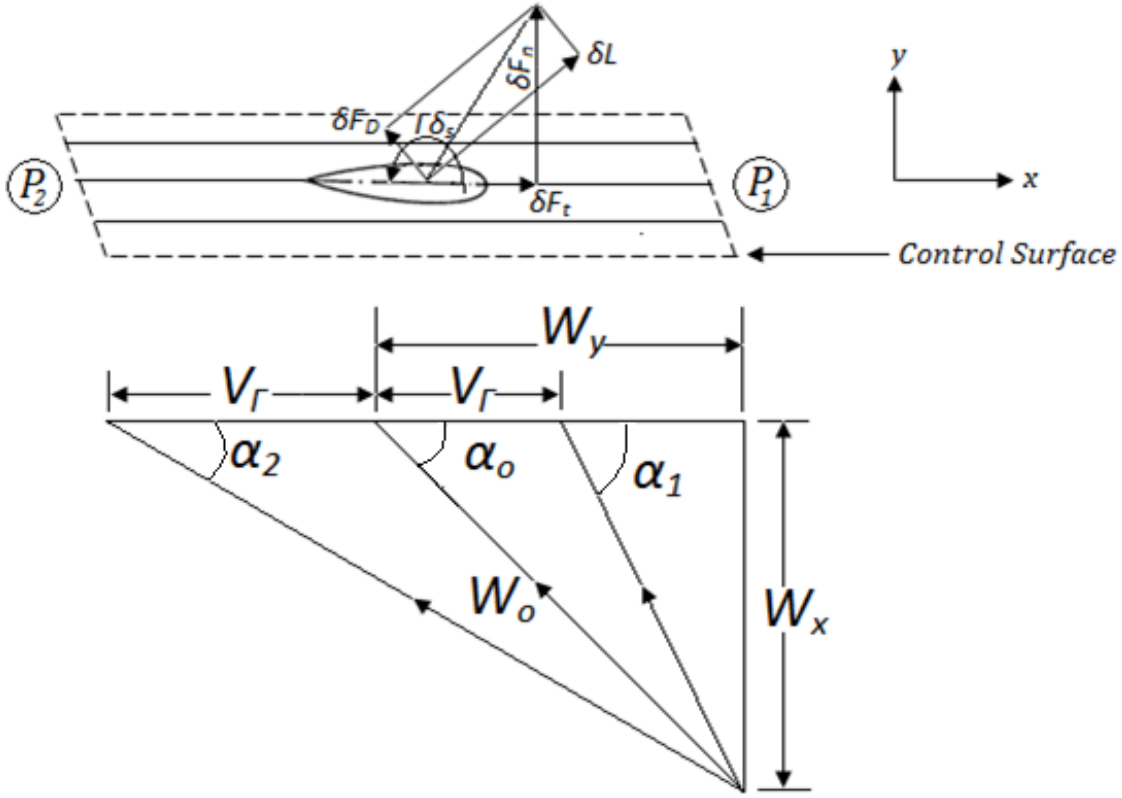

Figure 2-11: The control surface around the reference blade

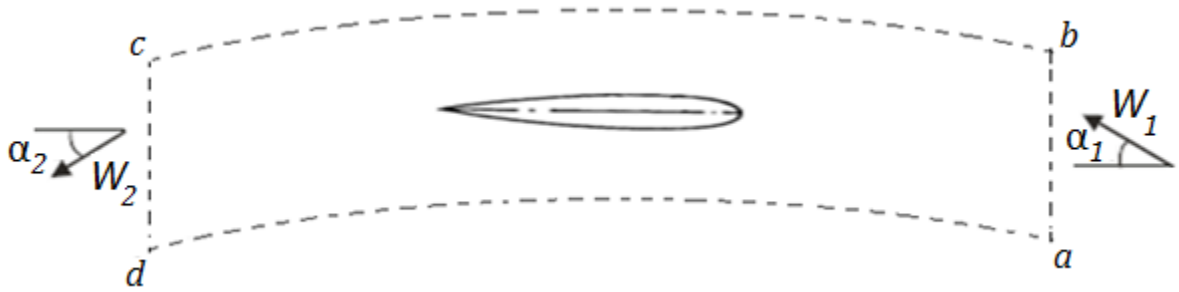

Figure 2-12: The path around the airfoil used to compute the circulation in the cascade theory (Bhimarasetty and N. 2010)

The net circulation around the path *abcd* with parallel lines *bc* and *ad* and *ab* and *cd* is:

$$\Gamma = t(W_1 \cos\alpha_1 - W_2 \cos\alpha_2) \qquad \text{Eq. 2.19}$$

where α_1 and α_2 are angles that W_1 and W_2 make with the horizontal axis, and t is the spacing distance of the two streamlines along the longitudinal length of the profile. Magnitudes of W_1 and W_2 must be different since they represent the inlet and outlet flow velocities, and since the turbine extracts kinetic energy from the flow, the outflow velocity will certainly be lower than the inlet velocity. Hence the circulation around the path can be represented by (from Figure 2-12):

$$\Gamma = \int_b^a \vec{W} \cdot d\vec{s} + \int_c^b \vec{W} \cdot d\vec{s} + \int_d^c \vec{W} \cdot d\vec{s} + \int_a^d \vec{W} \cdot d\vec{s} \qquad \text{Eq. 2.20}$$

Since the second and fourth terms in the RHS of Equation 2.20 cancel each other the circulation around the blade is represented by:

$$\Gamma = \int_b^a \vec{W} \cdot d\vec{s} + \int_d^c \vec{W} \cdot d\vec{s} \qquad \text{Eq. 2.21}$$

A comparison between Equations 2.17 and 2.19 indicated that the elemental tangential force can be expressed as a function of the circulation as: $\delta F_t = \rho W_x \Gamma \delta s$.

Alternatively, the flow through the control surface generates a net normal and tangential force on the airfoil which is found by applying the momentum conservation in the *y* direction, and are equal to the difference in momentum of the flow at the inlet and outlet of the cascade. This is represented by the following equations:

$$\delta F_t = \dot{m}_1 W_1 \cos\alpha_1 - \dot{m}_2 W_2 \cos\alpha_2 \quad \text{Eq. 2.22}$$

$$\delta F_n = \dot{m}_1 W_1 \sin\alpha_1 - \dot{m}_2 W_2 \sin\alpha_2 + t(P_1 - P_2)\delta s \quad \text{Eq. 2.23}$$

where the elemental mass flow rate is given as: $\delta \dot{m} = \rho t W_1 \sin\alpha_1 \delta s = \rho t W_2 \sin\alpha_2 \delta s = \rho t W_x \delta s$

thus, δF_t and δF_n can be expressed as:

$$\delta F_t = \rho t[W_1 \sin\alpha_1 W_1 \cos\alpha_1]\delta s - \rho t[W_2 \sin\alpha_2 W_2 \cos\alpha_2]\delta s \quad \text{Eq. 2.24}$$

$$\delta F_n = \rho t[W_1 \sin\alpha_1 W_1 \sin\alpha_1]\delta s - \rho t[W_2 \sin\alpha_2 W_2 \sin\alpha_2]\delta s + t(P_1 - P_2)\delta s \quad \text{Eq. 2.25}$$

The pressure difference also generates a force which is normal to the control surface. If the overall cascade loss is accounted for by a total pressure loss term, ΔP_{ov}, then for an incompressible flow, the Bernoulli equation can be applied to obtain an expression for this pressure difference between the cascade inlet and outlet:

$$P_1 - P_2 = \rho \frac{W_2^2 - W_1^2}{2} + \Delta P_{ov} \quad \text{Eq. 2.26}$$

Therefore,

$$P_1 - P_2 = \rho(W_2 \cos\alpha_2 - W_1 \cos\alpha_1)\left[\frac{W_1 \cos\alpha_1 + W_2 \cos\alpha_2}{2}\right] + \Delta P_{ov} \quad \text{Eq. 2.27}$$

By simplifying Equations 2.24 and 2.25 via Equations 2.19 and 2.27, the expressions for the normal and tangential forces are obtained as:

$$\delta F_t = \rho \Gamma W_x \delta s \quad \text{Eq. 2.28}$$

and

$$\delta F_n = -\rho\Gamma\left[\frac{W_1\cos\alpha_1 + W_2\cos\alpha_2}{2}\right]\delta s + t\Delta P_{ov}\delta s \qquad \text{Eq. 2.29}$$

The formulations in Equations 2.28 and 2.29 indicates that the tangential force does not depend on the pressure loss ΔP_{ov}, and the normal force is made of two parts, the part due to inviscid flow, and the part due to pressure loss.

$$\delta F_{n,id} = -\rho\Gamma\left[\frac{W_1\cos\alpha_1 + W_2\cos\alpha_2}{2}\right]\delta s \qquad \text{Eq. 2.30}$$

and

$$\delta F_{n,V} = t\Delta P_{ov}\delta s \qquad \text{Eq. 2.31}$$

The lift force of a frictionless cascade flow, L_{id}, is computed by the following equation:

$$\delta L_{id} = \sqrt{\delta F_t{}^2 + \delta F_{n,id}^2} = \left[\rho\Gamma\sqrt{W_x^2 + \left(\frac{W_1\cos\alpha_1 + W_2\cos\alpha_2}{2}\right)^2}\right]\delta s \qquad \text{Eq. 2.32}$$

The velocity squares under the square root are the components of W_0**.** Hence the validity of the Kutta-Joukowski theorem $(\delta L_{id} = \rho\Gamma W_0\delta s)$ for the blade in a cascade is proved.

W_0 is considered to be the "free-stream" velocity with respect to the cascade and is made of the fluid velocity, V_∞, and $R\omega$, the rotational velocity of the turbine. The flow velocities upstream of the cascade, $-(W_1\cos\alpha_1 - W_2\cos\alpha_2)/2 = \Gamma/2t$, and downstream of the cascade,

$(W_1 \cos\alpha_1 - W_2 \cos\alpha_2)/2 = -\Gamma/2t$, have been superimposed on the free-stream velocity in order to calculate the inlet and outlet velocities of the cascade (W_1 and W_2). The ratio $\Gamma/2t$, has the units of *m/s*, and hence is referred to as the circulation velocity V_Γ. Based on the vector diagram of the flow velocities in Figure 2-11, the resulting force diagram is of the form shown in Figure 2-13.

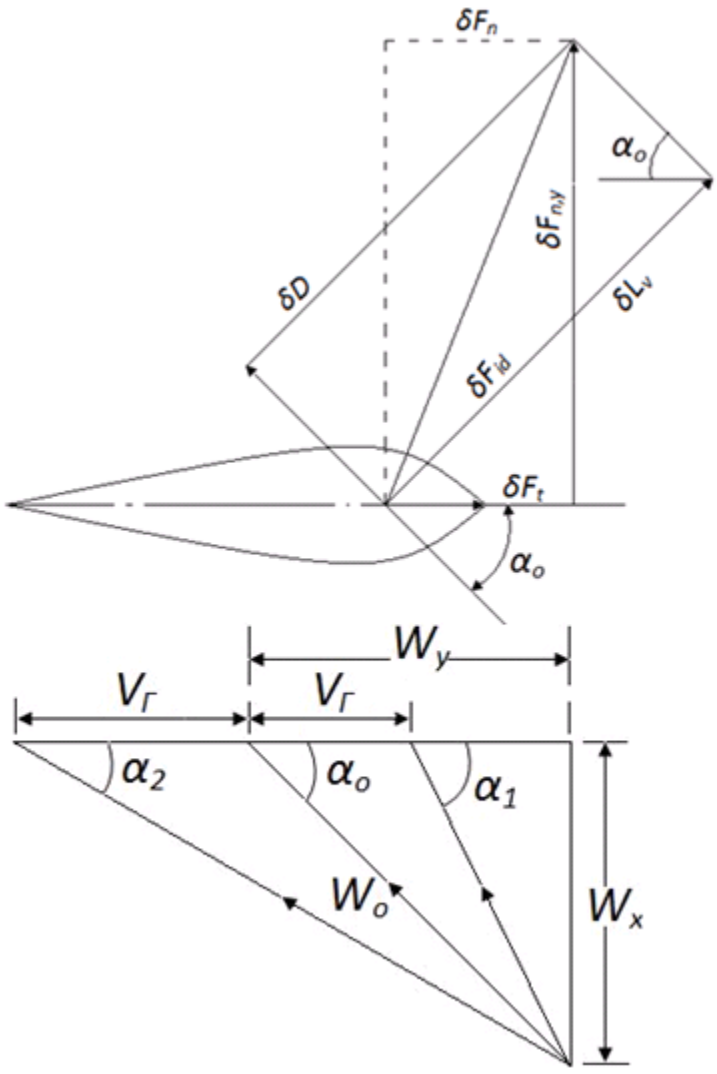

Figure 2-13: The blade forces on the airfoil

In the above force diagram, the force components δD and δL_V are normal to the direction of W_0 and are computed from the following equations:

$$\delta D = \delta F_{n,V} \sin \alpha_0 = t \Delta P_{0V} \sin \alpha_0 \delta s \qquad \text{Eq. 2.33}$$

and

$$\delta L_V = -\delta F_{n,V} \cos \alpha_0 = -t \Delta P_{0V} \cos \alpha_0 \delta s \qquad \text{Eq. 2.34}$$

Evidently, the pressure loss, ΔP_{0V}, contributes to drag the, δD, and lift force loss, δL_V. In an accelerating cascade the pressure energy is transformed into kinetic energy of the rotating blades. The total lift on the blades is given by the relation:

$$\delta L = \delta L_{id} + \delta L_V = \rho \Gamma W_0 \delta s - t \Delta P_{0V} \cos \alpha_0 \delta s \qquad \text{Eq. 2.35}$$

On the other hand, the lift force can be expressed as (Figure 2-13):

$$\delta L = \frac{\delta F_t}{\sin \alpha_0} - \delta D \cot \alpha_0 \qquad \text{Eq. 2.36}$$

By introducing $\varepsilon = \delta D / \delta L$ and substituting $\delta F_t = \rho W_\chi \Gamma \delta s$ into Equation 2.36, one can express the elemental lift force as:

$$\delta L = \rho W_0 \frac{\Gamma}{(1 - \varepsilon \cot \alpha_0)} \delta s \qquad \text{Eq. 2.37}$$

Also recalling the definition of lift coefficient:

$$\delta L = \frac{1}{2} C_L \rho W_0^2 C \delta s \qquad \text{Eq. 2.38}$$

From Equations 2.37 and 2.38, one can obtain an expression for the circulation and hence the circulation velocity:

$$\frac{V_\Gamma}{V_\infty} = \frac{1}{8\pi} C_L \left(\frac{NC}{R} \right) \frac{1}{\mu} \frac{W_0}{V_\infty} (1 - \varepsilon \cot \alpha_0) \qquad \text{Eq. 2.39}$$

The expressions for W_1 and W_2 and their corresponding angles α_1 and α_2 are found, from at Figure 2-13,

$$\frac{W_1^2}{V_\infty^2} = \frac{W_x^2}{V_\infty^2} + \frac{(W_y - V_\Gamma)^2}{V_\infty^2} \qquad \text{Eq. 2.40}$$

$$\frac{W_2^2}{V_\infty^2} = \frac{W_x^2}{V_\infty^2} + \frac{(W_y + V_\Gamma)^2}{V_\infty^2} \qquad \text{Eq. 2.41}$$

$$\alpha_1 = \tan^{-1} \left[\frac{W_x / V_\infty}{(W_y - V_\Gamma)/V_\infty} \right] \qquad \text{Eq. 2.42}$$

$$\alpha_2 = \tan^{-1} \left[\frac{W_x / V_\infty}{(W_y + V_\Gamma)/V_\infty} \right] \qquad \text{Eq. 2.43}$$

The elemental tangential and normal forces are represented as a function of W_1, W_2, α_1 and α_2 (similar to Equations 2.22, and 2.23)

$$\delta F_t = \delta \dot{m} (W_1 \sin \alpha_1 - W_2 \cos \alpha_2) \qquad \text{Eq. 2.44}$$

$$\delta F_n = \delta \dot{m} (W_1 \sin \alpha_1 - W_2 \sin \alpha_2) + t(P_1 - P_2) \delta s \qquad \text{Eq. 2.45}$$

Additionally, the normal force due to drag is:

$$\delta F_{n,v} = \frac{\delta D}{\sin \alpha_0}, \qquad \text{Eq. 2.46}$$

which is related to the pressure loss, ΔP_{0V}, as (Equation 2.31):

$$\delta F_{n,v} = t \Delta P_{0V} \delta s \qquad \text{Eq. 2.47}$$

Also recalling the definition of drag coefficient, the elemental drag force, δD can be represented as (C_D represents the drag coefficient):

$$\delta D = \frac{1}{2} C_D \rho W_0^2 C \delta s \qquad \text{Eq. 2.48}$$

Therefore the pressure loss term can be reexpressed as:

$$\frac{\Delta P_{0V}}{\rho V_\infty^2} = \frac{1}{4\pi} \times \frac{C_D}{\sin \alpha_0} \left(\frac{NC}{R} \Big/ \mu \right) \frac{W_0^2}{V_\infty^2} \qquad \text{Eq. 2.49}$$

To complete the formulation, we need an expression for the wake velocity. For this, the Bernoulli equation is used to find the absolute velocity at inlet (V_∞) and outlet (wake, V_w) of the cascade. Here the assumption is made that the pressure difference is the same as calculated before. Also it is assumed that the static pressure is unchanged with elevation, and therefore cancels each other. Consequently,

$$P_1 - P_2 = \frac{\rho}{2} \left(V_\infty^2 - V_w^2 \right) \qquad \text{Eq. 2.50}$$

Substituting Equations 2.27 and 2.49 into the Equation 2.50, the wake velocity V_w, can be expressed as:

$$\frac{Vw}{V_\infty} = \sqrt{1 - \left(\frac{W_2^2}{V_\infty^2} - \frac{W_1^2}{V_\infty^2}\right) - \frac{1}{2\pi}\left(\frac{NC}{R}\Big/\mu\right)\frac{C_D}{\sin\alpha_0} \times \frac{W_0^2}{V_\infty^2}} \qquad \text{Eq. 2.51}$$

The cascade model is an iterative model. The induced velocity V_d of the wind turbine is what is iterated for and it is based on the parameters like: the solidity, wind speed, number of blades, the blade spacing, RPM, the height and radius of the turbine, lift and drag coefficients, etc. From one iteration to the next, V_d is updated using the following a relationship between the free-stream velocity and wake velocity:

$$\frac{V_d}{V_\infty} = \left(\frac{V_w}{V_\infty}\right)^{K_i} \qquad \text{Eq. 2.52}$$

where K_i is found from experimental data, and is a function of solidity, σ :

$$K_i = 0.425 + 0.332\sigma \qquad \text{Eq. 2.53}$$

The values of F_t , F_n , V_w, α_0, etc are obtained at each angular position for all angles between Θ = 0˚ and 360˚. Finally, the torque is computed from F_t by averaging over all angular or azimuthal positions for all blades,

$$\tau = N \int_0^H \int_{0^\circ}^{360^\circ} \delta F_t \, d\theta \, ds \qquad \text{Eq. 2.54}$$

The power and power coefficient (*Cp*) are then calculated as:

$$Power = \tau \cdot RPM \qquad \text{Eq. 2.55}$$

$$C_p = \frac{Power}{0.5\rho V_\infty^3 HD} \qquad \text{Eq. 2.56}$$

The cascade model is formulated in such a way that the entire turbine is broken up into two segments (two half circles), the upstream half and the downstream half. The model is formulated to be applied separately for the two segments of the turbine. Even though the formulations for these two segments are similar, there are some differences.

First, in simulating the downstream half of the turbine, there are three possibilities for the inflow velocity:

1. The free-stream velocity. This is not a reasonable assumption because it will over-estimate the amount of energy available to generate power in this segment of the turbine. There has to be a balance between the energy transferred to the wind turbine from the wind to that removed from the flow. Thus, the wake velocity for any segment should be less than that of inflow velocity.

2. Use the wake velocity calculated for the upstream as the inflow velocity for the downstream segment. This is done in most of our simulations and is a logical choice. At every segment the wake velocity is obtained from analysis of the blade at that upstream segment and then used for the corresponding downstream segment.

3. Use the averaged upstream wake velocity of flow past over blades for the downstream segment of the turbine. Although this approach may also lead to either an over- or

underestimation of results when compared to an actual turbine, it was employed to ensure numerical stability when performing simulations at low free-stream velocities or high tip speed ratios ($TSR = R\omega/V_\infty$). Although the cascade model handles turbines at higher TSRs better than BEM models, because it is still based on momentum principles, thus has similar issues. One of these issues is the non-convergence of the iteration for V_d**.** In cases where the inflow velocity is low, (e.g. V_∞ = 3 m/s) at some point the lowest wake velocity may reach to 1 m/s at a certain angle. If this velocity is applied as the inflow velocity for the downstream segment, the iteration may not converge. By averaging the upstream wake velocities, the overall input velocity would be higher and convergence problems can be avoided.

The results (for efficiency, power and torque) that are obtained with the averaged wake velocity are within 5% of those predicted by the original method. The basic elements of the cascade model are shown in Figure 2-14, where the flowchart used in the simulation is shown.

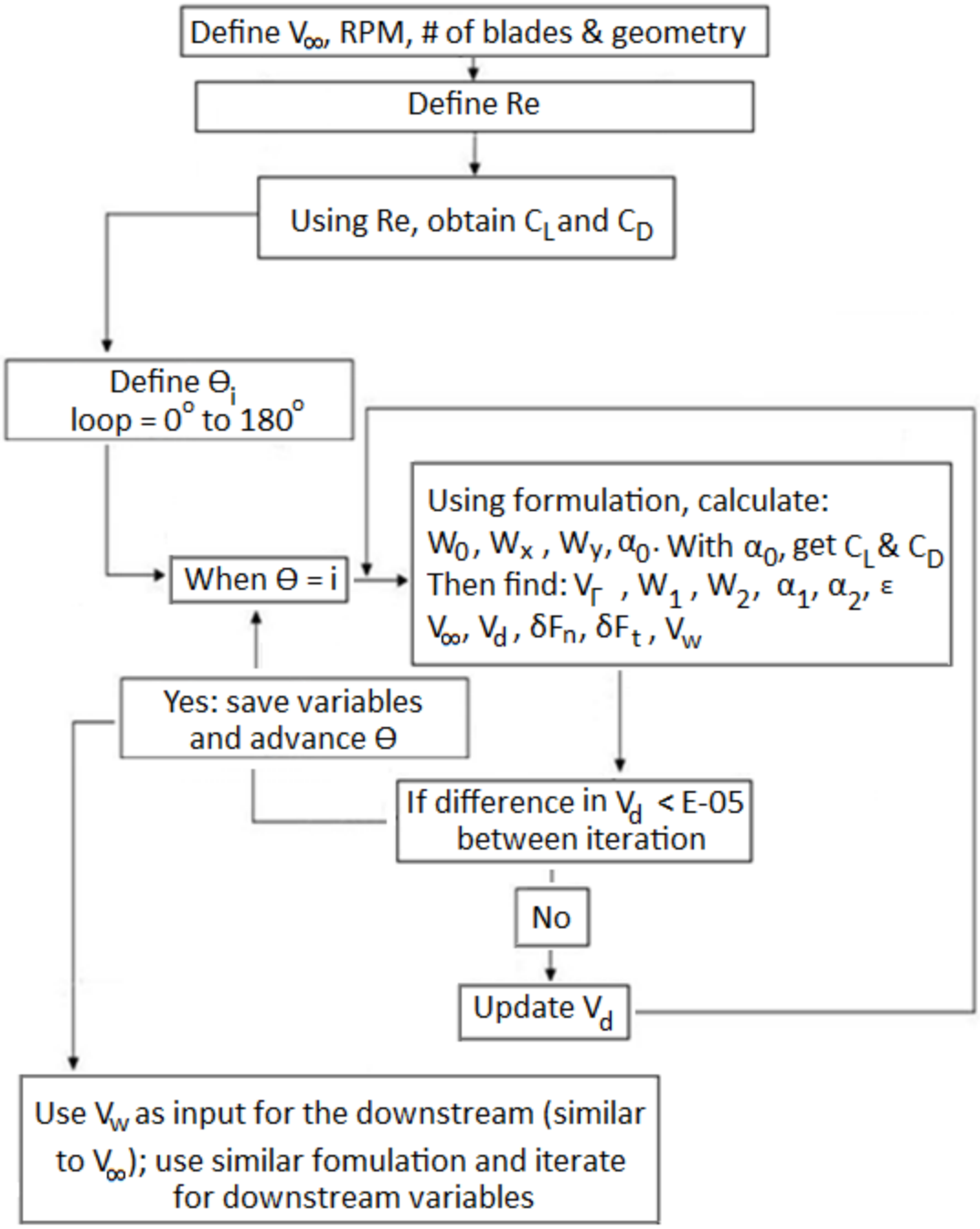

Figure 2-14 : Flowchart of simulations based on the cascade model.

2.2 FAST for HAWT

As stated previously, FAST stands for: Fatigue, Aerodynamics, structures, and Turbulence; it is a code developed by the National Renewable Energy Laboratory (NREL) for wind turbine analysis. It can be used to model both two and three bladed, horizontal-axis wind turbines. FAST models the wind turbine as a combination of rigid and flexible bodies. The aerodynamic module or subroutine in FAST is AeroDyn, and it is used in calculating the aerodynamic loads. Some key points about AeroDyn are:

- AeroDyn performs aerodynamic calculations on an element-by-element basis along the blade span for wind turbines using either: *Generalized Dynamic Wake (GDW) model or the Blade Element Momentum (BEM) method.* The GDW method takes considerably less time to run compared to the BEM method because the BEM method iterates for the induction factors used in calculating the loads on the blade element.

- The outputs from AeroDyn are: Velocity (*x*, *y*, and *z* components at the outmost blade element), angle of attack for each element, the dynamic pressure at the center of each element, C_L, C_D, C_{Norm}, C_{Tang}, blade pitch, axial induction factor, the tangential induction factor, and Reynolds Number.

- The accuracy of AeroDyn/ FAST prediction is highly dependent on the accuracy of the C_L and C_D values used. The values of C_L and C_D for every angle of attack are obtained from experimental data.

- AeroDyn uses a blade element method (BEM) similar to that described above for a VAWT. This BEM method is however customized for horizontal axis turbines. Like the

BEM method for VAWTs, this technique also uses an iterative process in which two variables: *a* and *a'* (axial and tangential induction factors) are iterated.

- When AeroDyn is using the BEM method it accounts for losses due to tip-loss, hub-loss, and losses due to $a > 0.4$ by applying the appropriate loss factor. However, in the GDW method these losses have already been factored into the calculations. An advantage of the GDW is that the induced velocities in the rotor plane are determined from a set of first-order differential equations, which are solved by a non-iterative technique; AeroDyn uses the fourth-order Adams-Bashford-Moulton (Press et al. 1982) predictor-corrector method.

- AeroDyn accepts either of two wind models: Hub-height wind profile, or a Full-Field Turbulence model.

Some key variables/ parameters of AeroDyn/ FAST are:

1. **Dynamic pressure** ($\frac{1}{2}\rho V^2$) - Defined based on ρ, the air density, and V is the total velocity at the element.

2. **Reynolds Number** - Defined based on the chord length and relative absolute local velocity.

3. **Element or Section Pitch** - The angle between the element's chord and the plane of rotation. It is a combination of the element twist angle and the blade pitch angle.

4. **Axial Induction Factor** - The extraction of kinetic energy from the air that passes over the wind turbine causes a reduction in the velocity. This factor is used to calculate the Betz limit, and the BEM equations are derived as a function of this factor. The ratio of

this reduction of velocity at the rotor plane to that of the air velocity far away from the wind turbine is defined as:

$$a = 1 - \frac{V_d}{V_\infty} \qquad \text{Eq. 2.57}$$

where $V_d = V_\infty(1 - a)$, $V_\infty a$ is the induced velocity at the rotor. As the induction factor increases from zero, the wind speed behind the rotor slows down.

5. **Tangential Induction Factor** - This similar to the axial induction factor. However, it is used to represent the effects of the induced rotational velocity in the wake as a result of the interaction of the free-stream with the rotating blade. After the wind passes through the rotating blade there is some induced rotation in the flow in an opposite direction. The tangential induction factor is the ratio of the, ω, induced rotational velocity in the wake to the rotational velocity of the blade, Ω:

$$a' = \frac{\omega}{\Omega} \qquad \text{Eq. 2.58}$$

From this we can see that the induced velocity of the flow across the blade is $a'\Omega r$ (r is the rotor location).

A 2-D wind turbine can be represented as having two velocity components: axial velocity at the turbine, V_d and rotational or tangential V_{rot}. These two velocities can be represented by a single velocity V_{rel} which has an inflow angle ϕ:

$$\tan\phi = \frac{V_d}{V_{rot}} \qquad \text{Eq. 2.59}$$

The axial velocity is the velocity of the air at the blade, and is computed from the free-stream and induced velocities as:

$$V_d = (1-a)V_\infty \qquad \text{Eq. 2.60}$$

The rotational velocity is obtained from the turbine blade and wake rotation:

$$V_{rot} = (\omega + \Omega)r \qquad \text{Eq. 2.61}$$

Equation 2.58 suggests that:

$$V_{rot} = (1+a')\Omega r \qquad \text{Eq. 2.62}$$

Hence the inflow angle is:

$$\tan\phi = \frac{(1-a)V_\infty}{(1+a')\Omega r} \qquad \text{Eq. 2.63}$$

The BEM method used in FAST iterates for *a* and *a'* until convergence is achieved.

The BEM method has some limitations. It assumes that the airflow field around the airfoil is always in equilibrium and that the passing flow accelerates instantaneously to adjust to the changes in the vorticity in the wake. It also assumes that the forces acting on the blade element are essentially two-dimensional. It does not model the blades experiencing large deflections out of the rotor plane. One of the major limitations of the original BEM theory is that there is no influence of vortices shed from the blade tips on the induced velocity. Lastly, when the induction factor is greater than about 0.4, the basic theory becomes invalid. This occurs with turbines operating at high tip speed ratios.

The GDW method also has its limitations. As with most wake models, the generalized dynamic wake was developed for lightly loaded rotors and assumes that the induced velocities are small relative to the mean flow. This assumption leads to instability of the method at low wind speeds when the turbulent wake conditions are approached.

Chapter 3: Vertical Axis Wind Turbines

3.1 Validation

To validate the cascade model for VAWT, two cases were simulated, and their results compared against those presented by other researchers. First, the results from this current study are compared with those generated from simulations done by the group at the Institut de Recherche d'Hydro-Quebec (IREQ) led by Ion Paraschivoiu. Those simulations are based on the double-multiple streamtube model and were conducted with the software called CARDAA (I. Paraschivoiu 1981). Figure 3-1 and Figure 3-2 summarize the results of this comparison. They show power versus V_∞, and *Cp* versus TSR for a 6 m straight blade VAWT. The parameters of this turbine are listed in Table 3-1 below.

There is good correlation between the results, especially at low wind speeds or low TRSs. It was also observed that the Reynolds number (Re) is important in these simulations because it determines the lift and drag coefficients used, and hence the amount of torque generated by the turbine blades. This study used tabular interpolation of experimental values of C_L and C_D as a function of angle of attack (α) and Re to calculate the different variables.

The Reynolds number in this study is based on the local flow conditions at the blade, i.e. the relative velocity based on the rotational speed and the free-stream velocity and is defined as:

$$\mathrm{Re} = \frac{CW}{\nu_\infty} \qquad \text{Eq. 3.1}$$

where W is the relative velocity and is defined as:

$$W = V\sqrt{\left[\mu\left(\frac{R\omega}{V_\infty}/\frac{V}{V_\infty}\right)+\cos\theta\right]^2+\sin^2\theta\cos^2\phi}, \qquad \text{Eq. 3.2}$$

and C represents the chord length of the airfoil and v is the kinematic viscosity.

Table 3-1: The geometry and parameters of the simulated VAWT

Parameter	Value
Rotor diameter	6.0 m
Rotor Height	6.0 m
Blade length	6.0 m
Blade chord length	0.2 m
Airfoil type	NACA 0015
Number of blades	2
Rotor ground clearance	3.0 m
Simulation RPM	125

Since Re is based on the local conditions, for W in the formulation above, V is the induced velocity calculated at every azimuth angle.

The code by Paraschivoiu has been validated against experimental data (mainly for Darrieus shaped turbines, see Figure 3-3) and therefore its results can be considered suitable for comparison.

The next comparison was done with the results presented by Migliore et. al., who conducted experiments on a 3 m straight blade turbine at West Virginia University (Migliore, W.P. and J.B. 1980). Figure 3-4 shows *Cp* versus TSR for this turbine. The author states that, this experiment was carried out based on a Reynolds number of 131,000; however it is unclear how a single fixed value was used to characterize the TSRs experienced by the turbine. According to the author, Re for this experiment is defined as $Re = R\omega C/v$. It is also stated that Re given is *"for Re at which max Cp occurred."* This and other geometric information are the only available information about these tests. From this information, the RPM was calculated and set constant and the wind velocity was calculated for each TSR. However, since only the Re at maximum *Cp* was presented for the entire test case, without having the instantaneous V_∞ or ω, at best any simulation to match these results will be dependent on selecting the right Reynolds number which characterizes the average flow conditions experienced by this turbine. Figure 3-4 shows that by using a Reynolds number of 69,000, the results become very close.

The code developed here based on cascade theory offers an efficient way of studying the effects of various parameters on the power output of VAWTs as well as their efficiencies. A turbine with input parameters as in Table 3-1 is analyzed in the following sections. The goal is to gain a better understanding of the characteristics of a straight bladed VAWT and to give insight as to how they can be optimized.

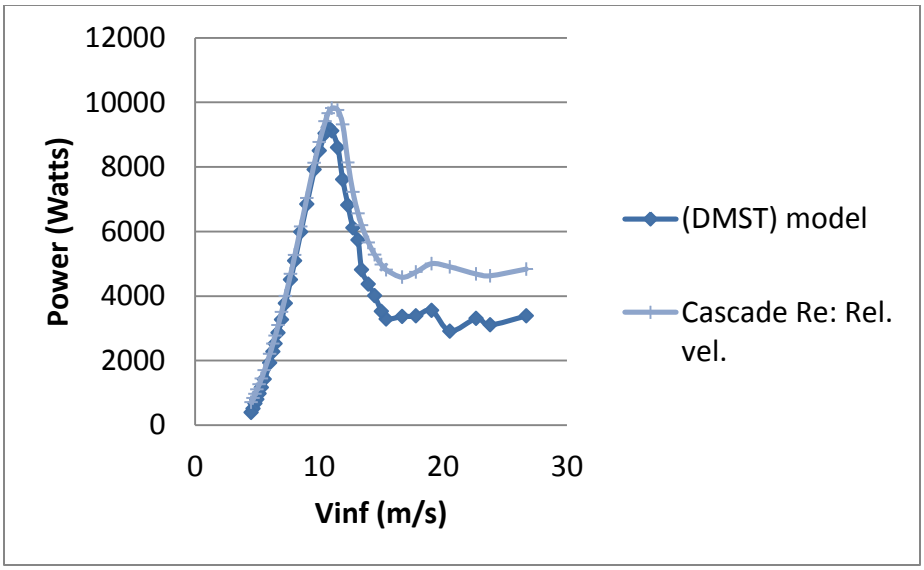

Figure 3-1: Power vs. V_{∞}, obtained from the CARDAA (DSTM model) and the cascade model.

"For interpretation of the references to color in this and all other figures, the reader is referred to the electronic version of this thesis."

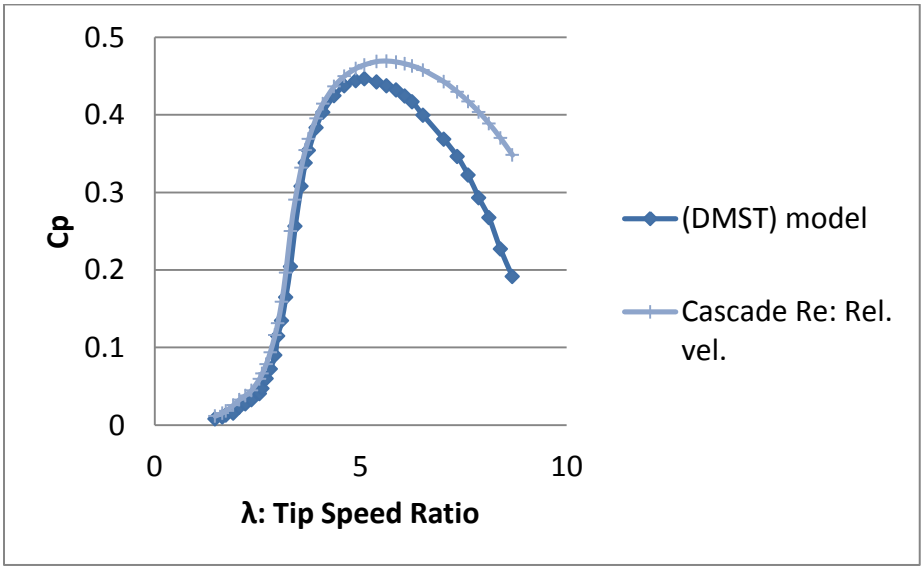

Figure 3-2: *Cp* vs. TSR, obtained by the CARDAA (DSTM) and cascade models.

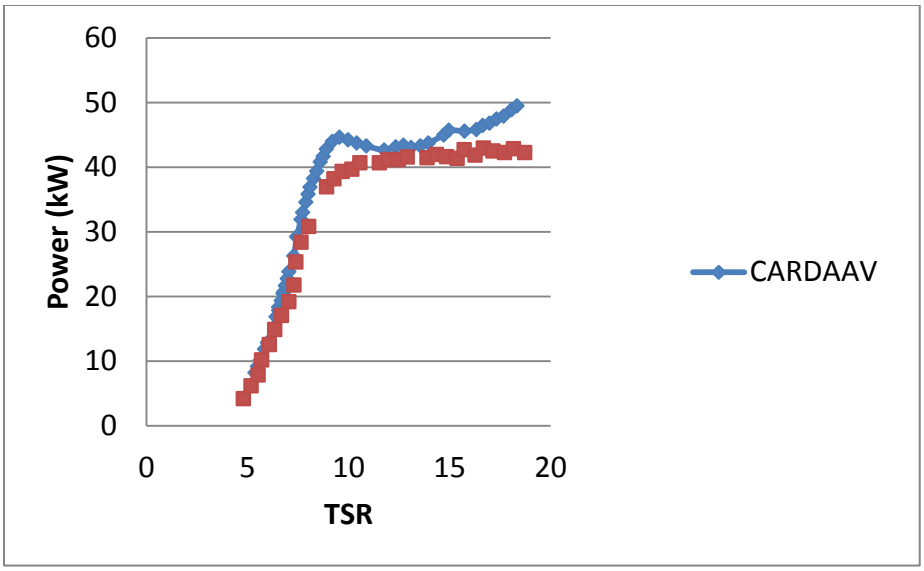

Figure 3-3: The results from the CARDAA code compared with experimental results of a 17 m SANDIA Darrieus VAWT

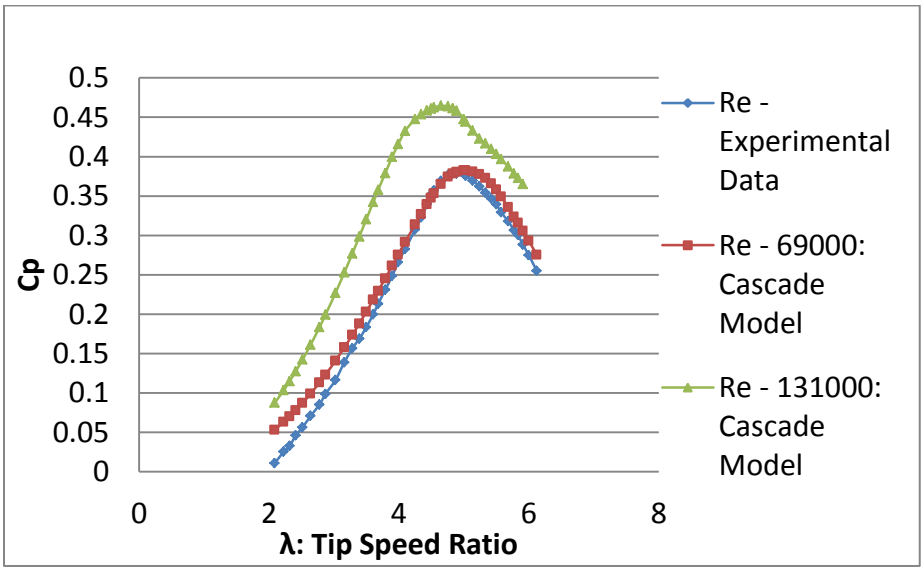

Figure 3-4: *Cp* vs. Tip speed ratio for a 3 m expereimental turbine

3.2 Results and Discussion

In this section the effects of various parameters on the VAWT performance are discussed.

3.2.1 Tip Speed Ratio

The tip speed ratio (TSR), λ, is a nondimensional quantity which gives the ratio of rotational speed to the free-stream velocity V_∞:

$$\lambda = \frac{R\omega}{V_\infty}, \qquad \text{Eq. 3.3}$$

where R is the radius of the turbine, ω is the turbine's rotational speed, in *radians/second*, and V_∞ is the free-stream velocity of the wind. In a Darrieus turbine with curved blades, the radius is taken at the turbine equator (the section along the span with the largest radius), λ_{eq}.

The coefficient of power, Cp is simply calculated by dividing the power extracted by the turbine in the wind's path with the total power available in the wind.

$$Cp = \frac{P_{Turbine}}{\frac{1}{2}\rho V_\infty^3 HD} \qquad \text{Eq. 3.4}$$

Plots of Cp versus λ are good indicators of how a particular turbine performs under various inflow and rotational conditions and are shown in the following sections. This becomes particularly important in experiments because the rotational velocity and the wind velocity are constantly changing, and since both quantities are inherently tied to each other (i.e. a change in the wind velocity may change the RPM if no load is applied to the system), the tip speed ratio provides an effective way of summarizing their effects on the power output of the turbine.

3.2.2 Effects of Reynolds number

The importance of selecting the right Re cannot be over-emphasized. In this section the global effects of Re will be studied based on how it affects power generation for the turbine. The classic definition of Re takes into account the flows density, the velocity of the flow, a length scale which is descriptive of the surface over which the fluid flows, and the fluid's viscosity. The characteristic length takes on various forms depending on the shape of the body, and what sections interacts with the fluid, in the case of a wind turbine this characteristic length can be the chord length. The wind turbine community has several methods of calculating the Re:

1. Some researchers have used the Reynolds number based on wind speed, Re_w, defined as:

$$\mathrm{Re}_w = \frac{V_\infty C}{\upsilon_\infty} \qquad \text{Eq. 3.5}$$

   This is a common definition used for flows over an airfoil. This definition was used in the Sandia experiment to generate lift and drag coefficients data, and this data was used in our study. For VAWT simulations, characterizing the flow based only on the free-stream velocity, viscosity, and the chord length may not provide an adequate description of the flow because it does not consider the rotational velocity.

2. Another definition of Reynolds number specific to wind turbines, known as the turbine speed Reynolds number, Re_t, uses the chord length and rotational velocity:

$$\mathrm{Re}_t = \frac{R\omega C}{\upsilon_\infty} \qquad \text{Eq. 3.6}$$

3. The definition based on the local relative velocity and chord length is, $\mathrm{Re}_{V_{relative}}$:

$$\mathrm{Re}_{V_{relative}} = \frac{WC}{\upsilon_\infty} \qquad \text{Eq. 3.7}$$

W is the relative velocity defined as:

$$W = V\sqrt{\left[\mu\left(\frac{R\omega}{V_\infty}/\frac{V}{V_\infty}\right)+\cos\theta\right]^2+\sin^2\theta\cos^2\phi} \qquad \text{Eq. 3.8}$$

and *V* is the induced relative velocity calculated at every azimuth angle.

An argument can be presented that any of these definitions is in-line with how the airfoil experiments are conducted, or the turbine operated. The results obtained with different Re are presented next.

Figure 3-5 shows *Cp* versus TSR for three Re values. In these simulations, the RPM was fixed at three values of 105, 115, and 125; and the wind velocities were varied between 4.5 to 26 m/s (10 to 60 mph); the RPM is changed so that Re_t = 4.5E+5, 4.9E+5, and 5.4E+5. This method was also used by scientists at the Sandia National Laboratories when reporting experimental effects of Re on a 17 m Darrieus turbine (Worstell 1978). Simulation results presented in Figure 3-5 show that for the chosen values of Re, there is not much difference in *Cp* at very low TSRs. However, at TSR $\geq$ 2.0 the efficiency of the turbine increases with Re_t. The results in Figure 3-5 also suggest that for a given turbine, at a certain inflow velocity, the turbine can be adjusted for the peak performance by varying the RPM to attain the optimum TSR (or vice versa if V_∞ is fixed).

As has been emphasized earlier, the accuracy of any empirical model is dependent on the C_L and C_D data used. Although the C_L and C_D data were from experimental testing of the actual NACA 0015 airfoil, they represent static test results and do not include the rotational effects experienced by the turbine* (Migliore, W.P. and J.B. 1980), nor the effects of dynamic stall resulting from the constantly changing angle of attack. These factors drastically change the "effective" angle of attack and hence the lift and drag coefficients which ultimately affect the torque generated at each azimuth angle.

The three definitions of Re indeed yield very different results. We use different methods in which the flow is simulated, either with Re averaged over all TSRs, found at each angular position, or use Reynolds number calculated at every TSR: (1) Re_t, (2) Re_w averaged over all TSR, (3) Re_w changed at every TSR, (4) Re based on the local flow velocities, (5) Constant Re_w using the V_∞ value which gives maximum *Cp*, (6) Re based on the absolute relative velocity:

$$\mathrm{Re}_{V\ absolute} = \frac{C\sqrt{(R\omega)^2 + V_\infty^2}}{\nu_\infty}.$$

For sake of comparison, the case conducted by Paraschivoiu will be taken as a reference case.

* In the current analysis the flow is considered as rectilinear, however, according to Migliore et el, from experimental work done on a straight bladed VAWT, the curvilinear effects on the turbine blade significantly affect the behavior of the turbine when compared to one immersed in a rectilinear flow. Their experiments show that the turbine blade relative inflow velocity and angle of attack are unique everywhere on the chord.

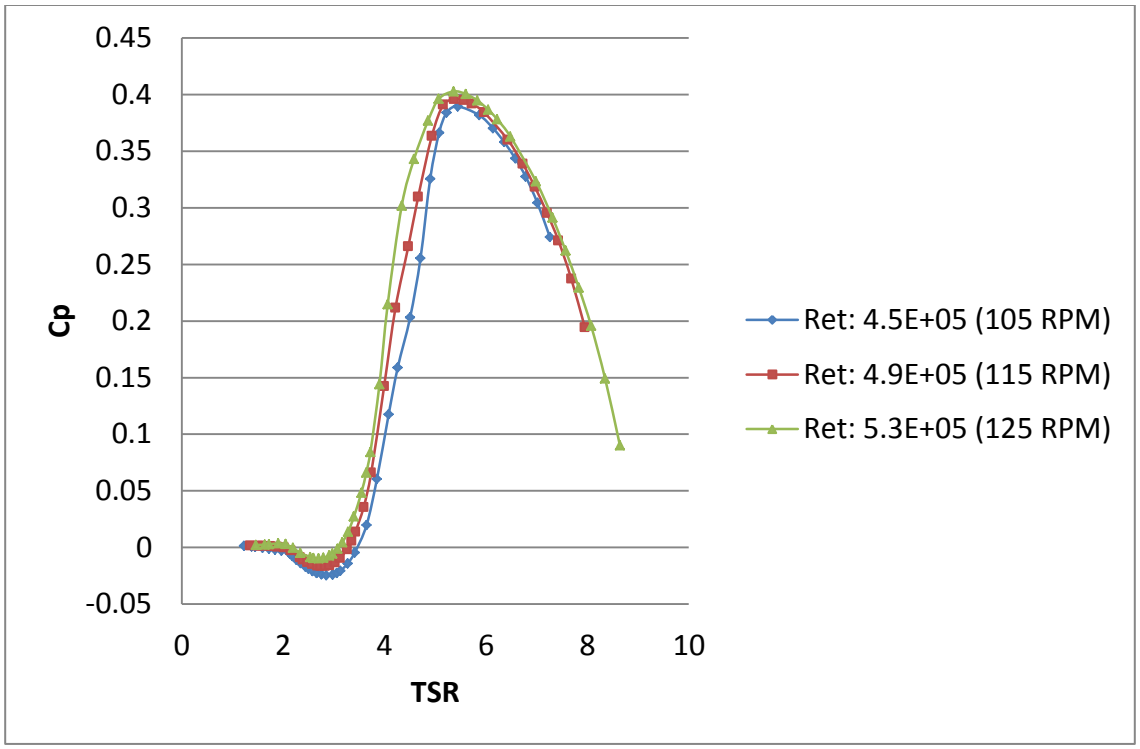

Figure 3-5: Power coefficient *Cp* variations with Re for the test case simulated using the cascade model

The Reynolds number used in this study is based on a linear interpolation method which calculates C_L and C_D from tables. The range of Re available from experiment is 10,000 to 2,000,000. To show the significant differences derived from using the property tables of different Re, Figure 3-6 and Figure 3-7 are plotted which show C_L and C_D versus α for different Re obtained directly from experimental data (and tabular interpolation). Figure 3-8 and Figure 3-9 show *Cp* for different methods of calculating Re; the RPM was fixed at 125, and V_∞ varied between 4.5 to 26 m/s. Figure 3-8 indicates that the simulations based on $Re_{V_{absolute}}$ and $Re_{V_{relative}}$ adequately predict the performance of the turbine at low to moderate TSRs, however tends to over-predict it at high TSRs. While from low to mid TSRs, results based on

Re_w averaged under-predicts the turbine efficiency, and for mid to high TSRs the performance is over-predicted. The case using Re_w under-predicts *Cp* in for all TSRs. It is interesting to note that *Cp* based on Re_t at the largest TSR simulated is seven times larger than that based on Re_w.

Figure 3-10 shows C_L versus α for a TSR of 4.4, this TSR gives the maximum *Cp* of all plots in Figure 3-8. The results in this figure are all based on the same flow conditions; the only difference is how the Reynolds number is calculated. As can be seen in Figure 3-10, irrespective of the simulation Re used, for the same flow conditions and turbine configuration, the computed flow parameters such as the: relative velocity, α, azimuthal torques calculated, etc., are the same before stall develops (see Figure 3-11 for torque versus Θ for various Re). In Figure 3-12, at Θ angles of 0˚, 180˚, and 360˚ the flow is not stalled. This characteristic of momentum models was also observed in the results obtained by the National Renewable Energy Laboratory (NREL), "When used with accurate 2-D airfoil wind-tunnel data at angles of attack below stall, BEM [Blade-Element Momentum] provides reasonably accurate performance prediction (Tangler and Kocurek 2005)."

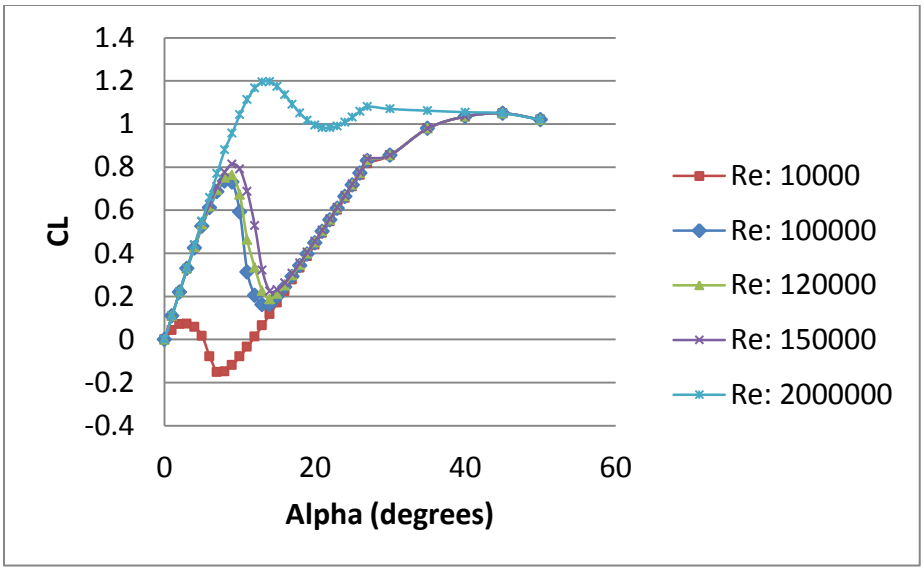

Figure 3-6: C_L vs. angle of attack for different Reynolds numbers

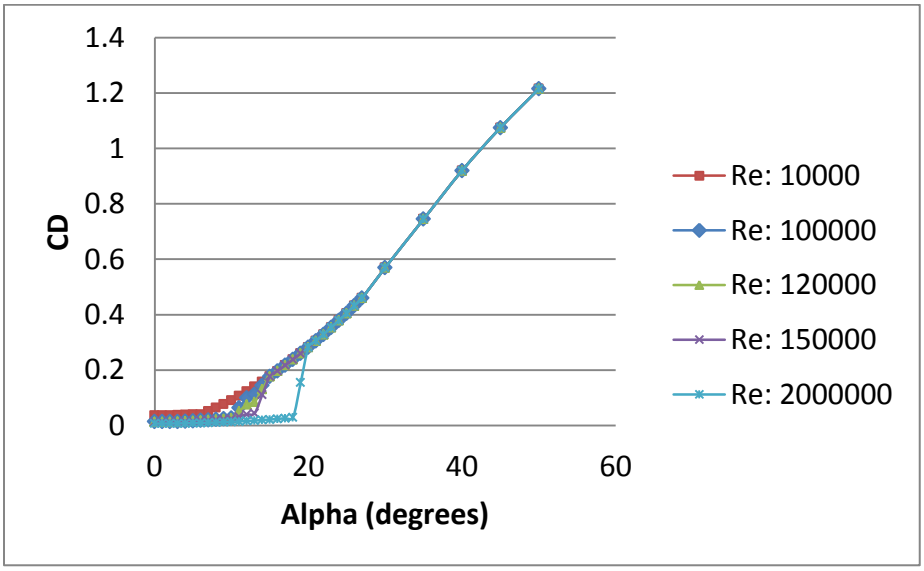

Figure 3-7: C_D vs. angle of attack for different Reynolds numbers

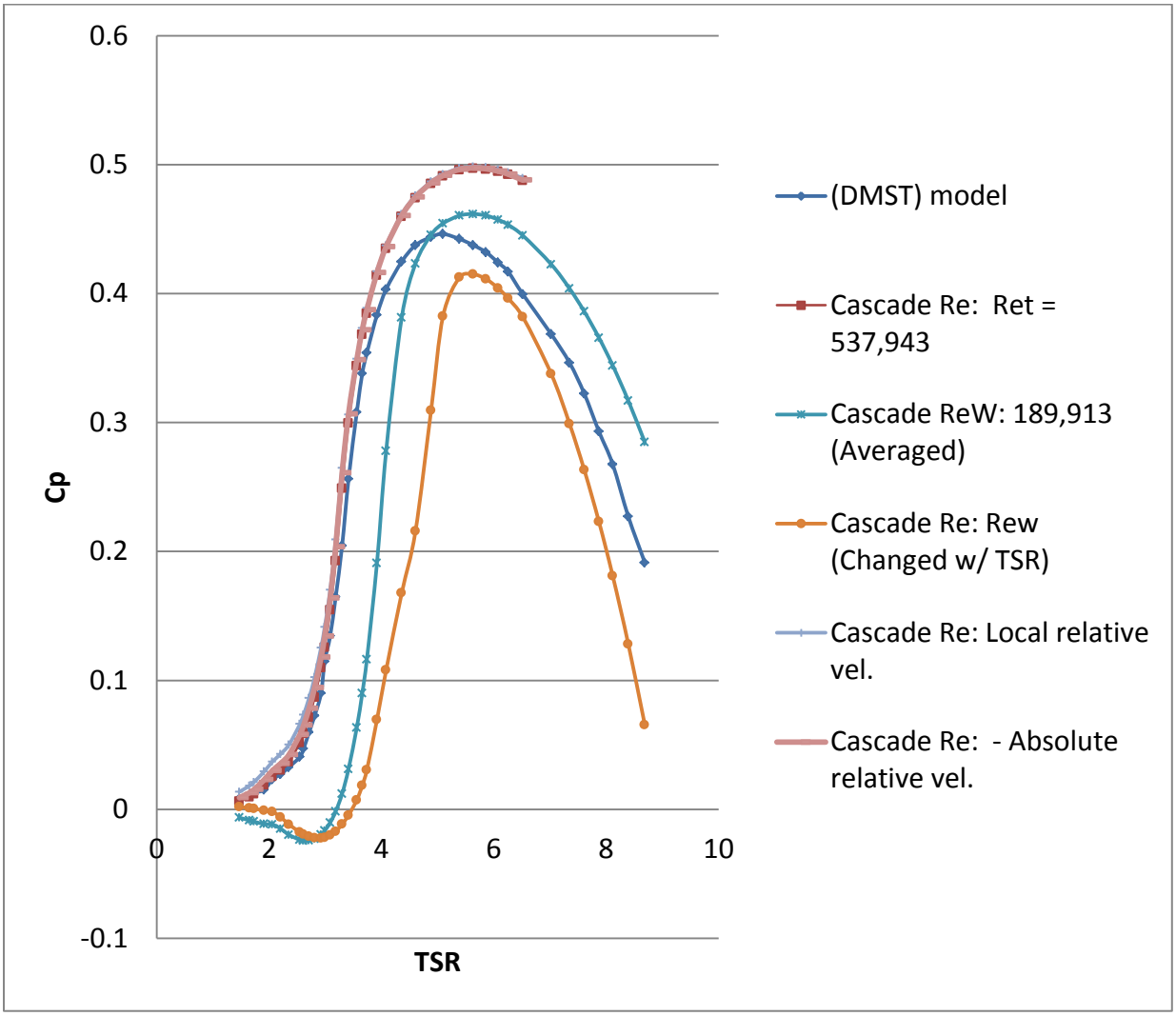

Figure 3-8: *Cp* vs. TSR for Re calculated based on six different methods

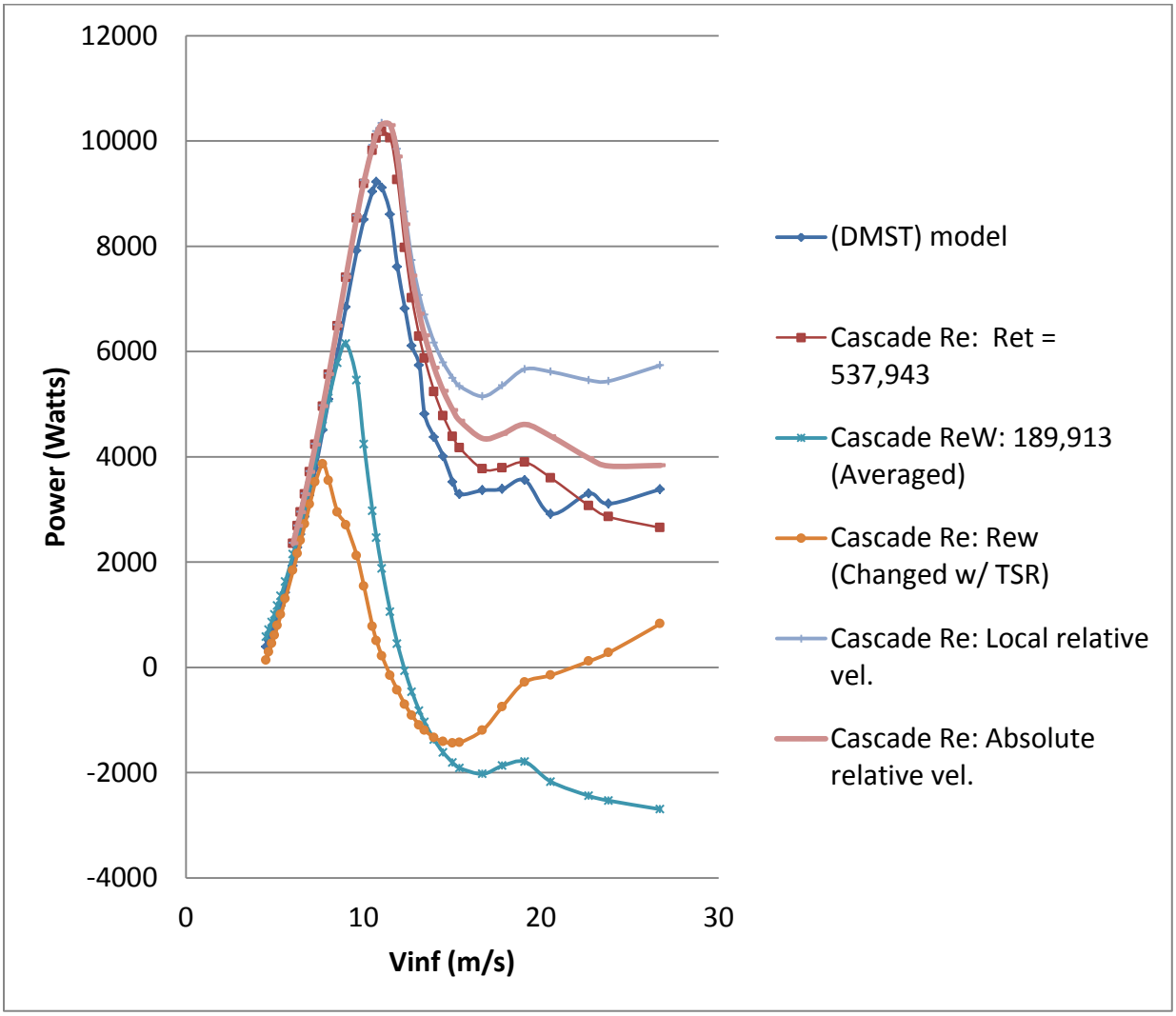

Figure 3-9: Power vs. wind speed for Re calculated based on six different methods

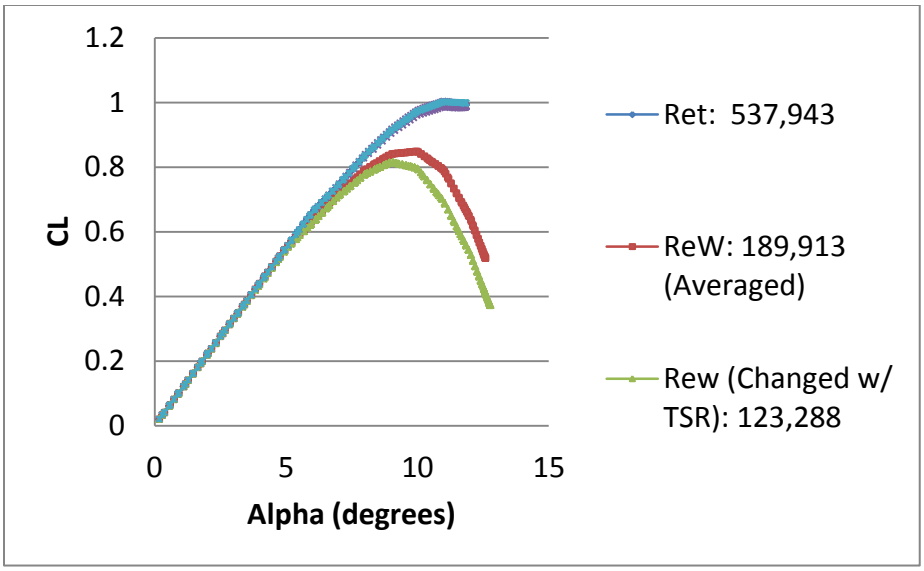

Figure 3-10: C_L vs. alpha at a TSR of 4.4. The RPM simulated was fixed at 125. This figure is plotted after convergence has been achieved for this TSR. This figure shows only the lift coefficients and angle of attacks generated in the upstream of the turbine

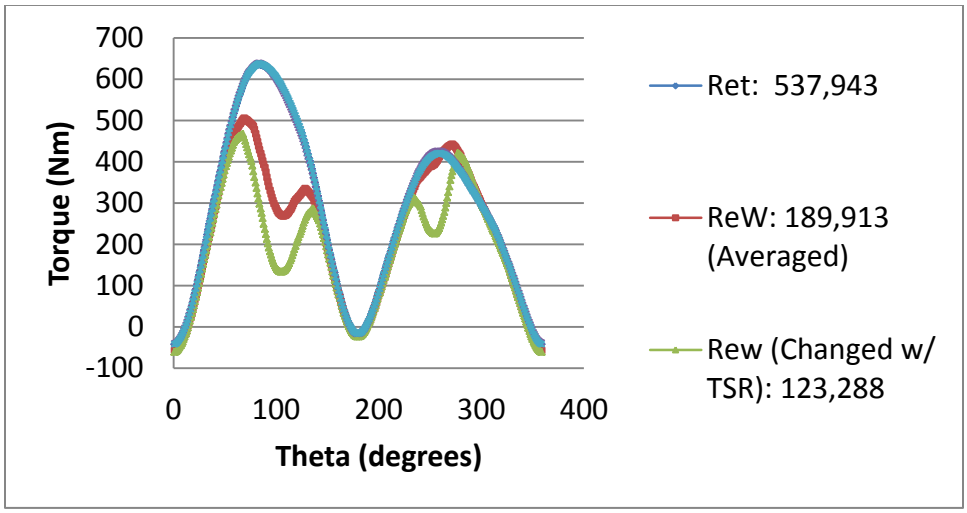

Figure 3-11: Torque vs. Θ at a TSR of 4.4. This figure is plotted after convergence has been achieved for this TSR. The RPM simulated was fixed at 125. This figure shows the torque characteristics for both the up and downstream of the turbine

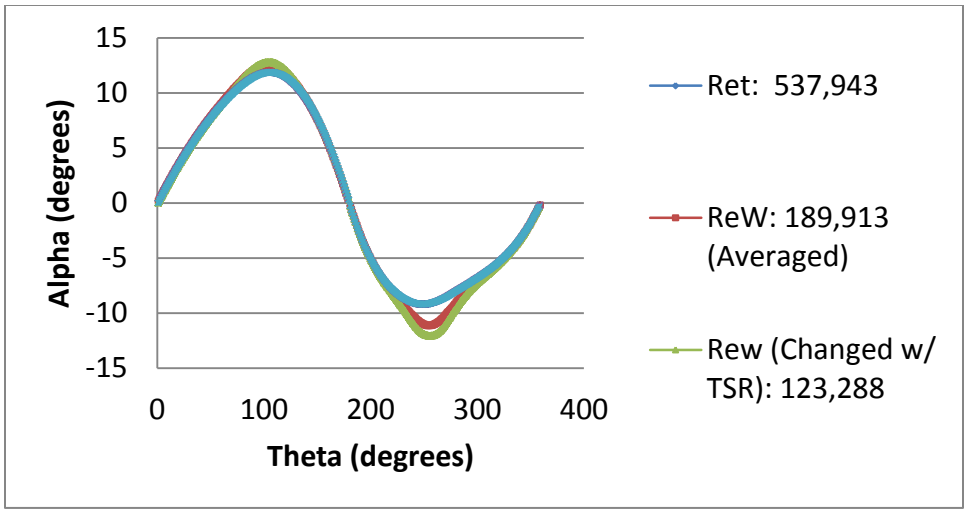

Figure 3-12: Angle of attack vs. Θ at a TSR of 4.4. This figure is plotted after convergence has been achieved for this TSR. The RPM simulated was fixed at 125. This figure shows the angles of attack for both the up and downstream of the turbine

Corrections to C_L and C_D Data

Several corrections that have been proposed to account for deficiencies of using static property data derived from experiments in simulations. The effects of two of these corrections will be observed in this section.

The first correction corrects the experimental data to account for the effects of a finite wing. In experiments to obtain C_L and C_D, a wind tunnel is used with the airfoil's span length usually the width of the wind tunnel. This wing section is classified as a semi-infinite wing. The relevance of this classification is to make the approximation that the effects of the flow in the *z* direction are negligible. In addition, this classification makes the effects of the wing-tip vorticity negligible (Anderson Jr. 2001). In a finite wing, the tip vorticity induces some drag, known as the induced drag, $C_{D,i}$, and with this there is also an induced angle of attack, α_i. Modifications to the data are

made based on the theory of *Elliptical Lift Distribution* which was developed by Ludwig Prandtl and is part of his classic lifting-line theory. For the unstalled conditions, the equations that modify α and the C_D are:

$$\alpha_{New} = \alpha + \alpha_i = \alpha + \frac{C_L}{\pi AR} \quad \text{Eq. 3.9}$$

$$C_{D,New} = C_D + C_{D,i} = C_D + \frac{C_L^2}{\pi AR} \quad \text{Eq. 3.10}$$

where AR is the aspect ratio, $AR = H/C$, H is the height, and C is the chord length.

Due to the nonlinear nature of the C_L and C_D curves at stall conditions, the Elliptical Lift Distribution theory becomes inadequate and should not be used to modify the property data in this region. For post-stall data, a method proposed by Viterna and Corrigan provides a convenient global approach to relate the post-stall C_L and C_D to the overall blade geometry and flow conditions. However, although this method has been used for predicting post-stall airfoil characteristics, an incomplete understanding of the stall process existed at the time of its development (Tangler and Kocurek 2005). The Viterna equations were developed for α_{stall} up to 90˚:

if $AR < 50$, $C_{D,\max} = 1.11 + 0.18AR$ and if AR > 50, $C_{D,\max} = 2.01$,

$$C_D = B_1 \sin^2 \alpha + B_2 \cos \alpha \quad \text{Eq. 3.11}$$

where B_1 and B_2 are:

$$B_1 = C_{D,\max} \quad \text{Eq. 3.12}$$

$$B_2 = \frac{C_{D,stall} - C_{D,\max} \sin^2 \alpha_{stall}}{\cos \alpha_{stall}} \quad \text{Eq. 3.13}$$

$$C_L = A_1 \sin 2\alpha + A_2 \frac{\cos^2 \alpha}{\sin \alpha} \quad \text{Eq. 3.14}$$

where A_1 and A_2 are:

$$A_1 = B_1 / 2 \quad \text{Eq. 3.15}$$

$$A_2 = \left(C_{L,stall} - C_{D,\max} \sin \alpha_{stall} \cos \alpha_{stall}\right) \frac{\sin \alpha_{stall}}{\cos^2 \alpha_{stall}} \quad \text{Eq. 3.16}$$

It should be noted that for the cases simulated so far none of these corrections have been implemented to modify the property tables.

To study the effects of these modifications on the data, C_L and C_D versus α are plotted in Figure 3-13 and Figure 3-14 applying the different corrections. These figures were plotted for Re_t. For the plots without correction and that with Prandtl's correction there is only a slight difference; the average difference between their α values is 0.0074, and the difference in values of C_D is 0.0060. On the hand, when the Viterna correction is applied, there is a significant reduction in the amount of stalling that occurs as can be observed in Figure 3-13 and Figure 3-14. It also reduces the lift coefficient at higher ($\alpha > 24^\circ$) angles of attack. The effect of these corrections on

the turbine performance is shown in Figure 3-15 which shows power versus V_∞. As should be expected, there is only a slight difference in the results for the case using Prandtl's correction and the case with no corrections. However, when the Viterna correction is applied, the power is over-predicted for high wind velocities.

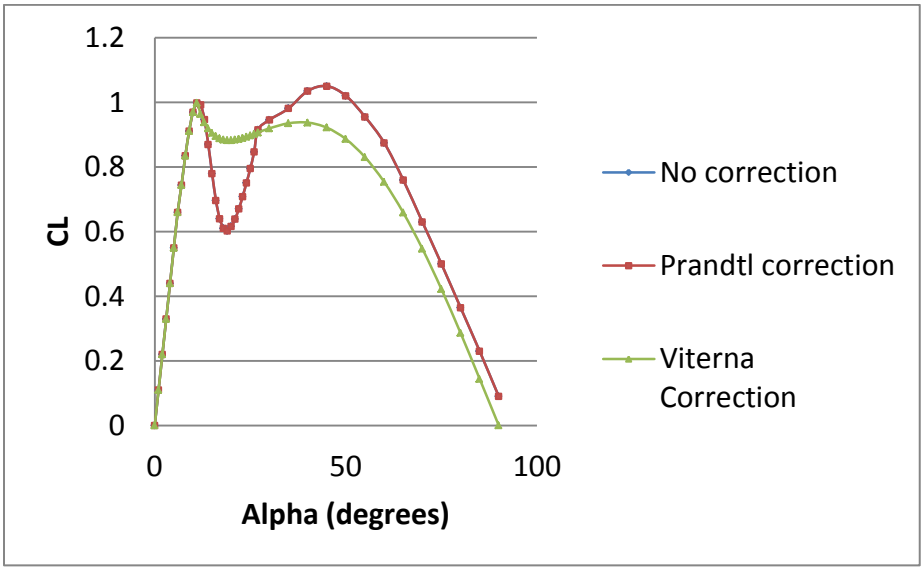

Figure 3-13: C_L vs. angle of attack for the TSR of 4.4. The RPM simulated was fixed at 125

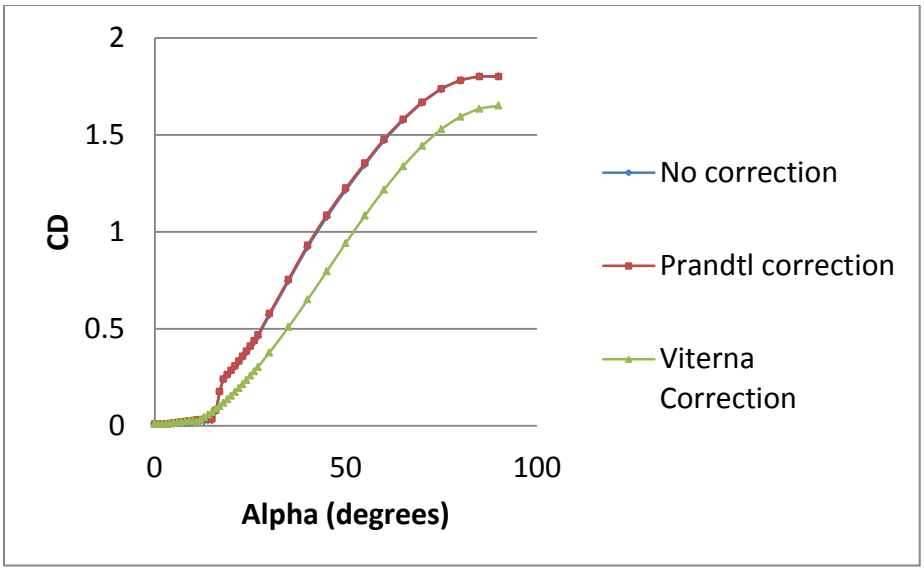

Figure 3-14: C_D vs. angle of attack for the TSR of 4.4. The RPM simulated was fixed at 125

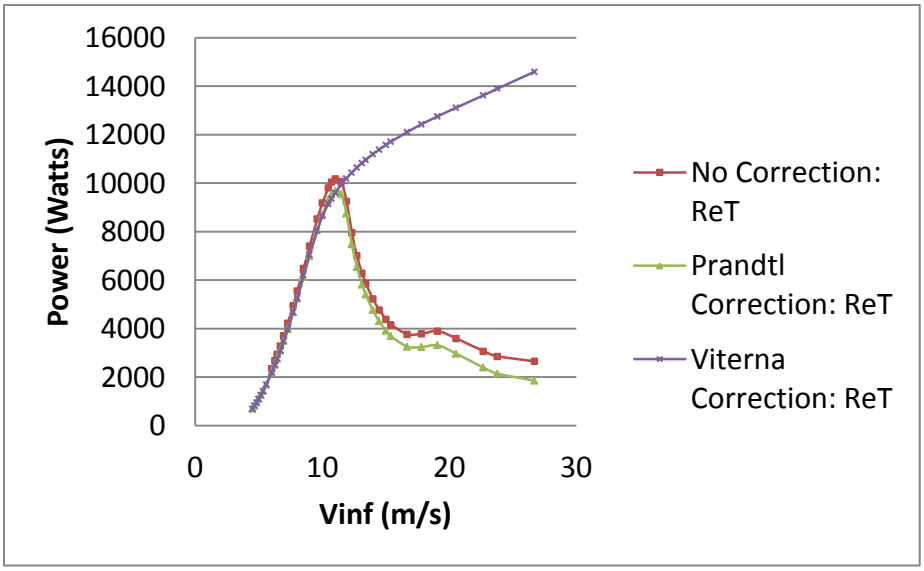

Figure 3-15: Power vs. wind speed for the TSR of 4.4. The RPM simulated was fixed at 125

3.2.3 Torque Characteristics of VAWT

Figure 3-16 shows four points on the *Cp* versus TSR curve for the turbine in Table 3-1, and Figure 3-17, Figure 3-18 and Figure 3-19 present the torque characteristics of these points (for brevity only the upstream is shown, the downstream section has similar behavior). The C_L and C_D coefficients are also plotted versus azimuthal angles to show how they affect the torque produced. The result of the last marked point was not included due to convergence issues for such a heavily loaded turbine and high TSR.

Comparing the torque plots for different TSRs, it can easily be seen why a TSR of 1.65 has the poorest efficiency: the very low to negative torque values at most angular positions which is caused by high amounts of drag generates low power. We can observe in this figure that the torque peaks coincides with the low drag coefficient and with relatively high lift coefficients. Around azimuthal angle of 50˚ stall occurs, resulting in a rapid drop in lift coefficient and a significant increase in drag. Over the remainder of the upstream section, the turbine exhibits a poor lift to drag ratio and aerodynamic efficiency. The plots for TSR of 3.09 follow a similar trend, even though that the aerodynamic efficiencies are better. At TSR of 5.63, the aerodynamic efficiency is superior with almost zero drag and high lift coefficients over the entire upstream section.

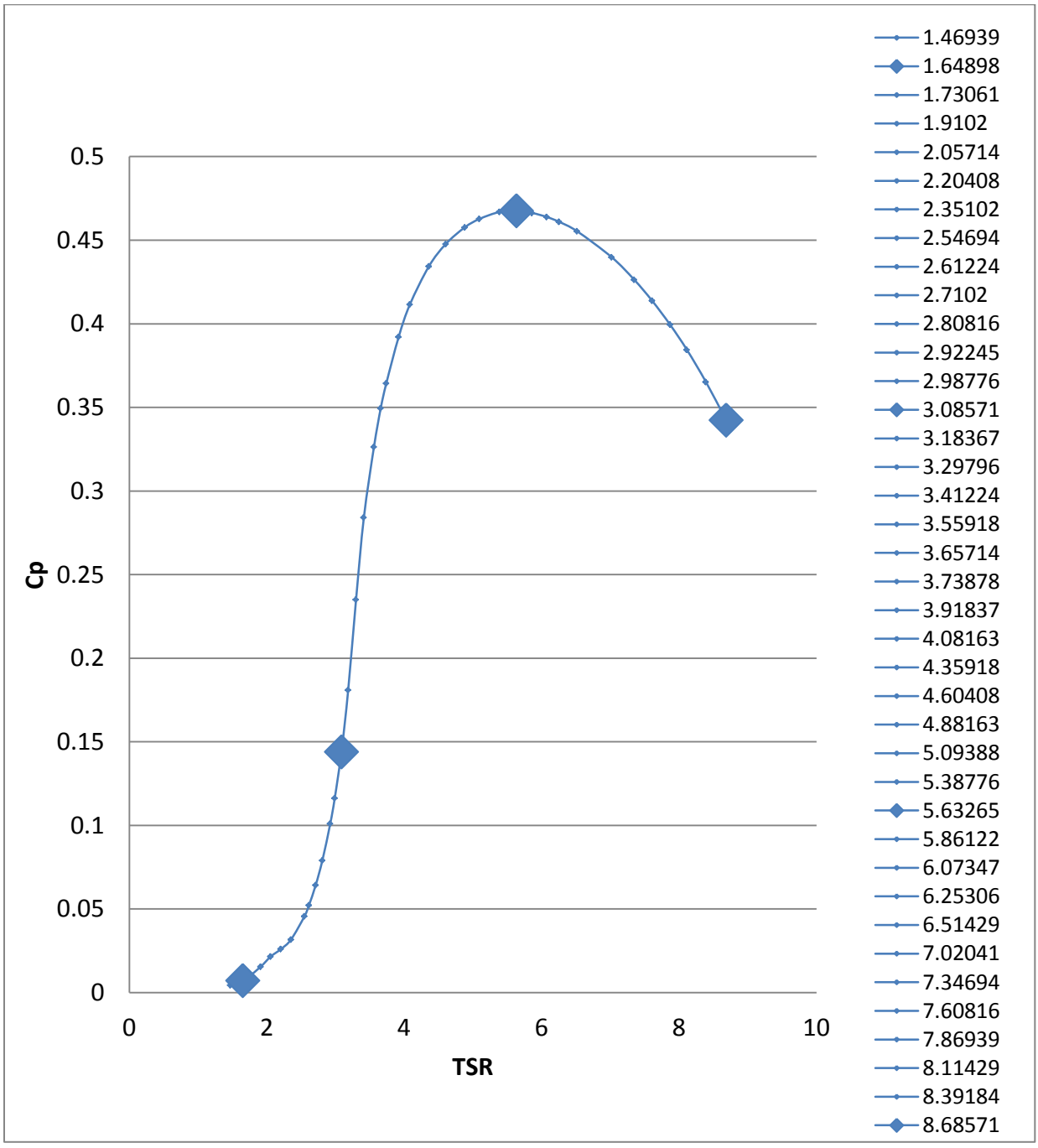

Figure 3-16: *Cp* vs. TSR for the turbine in Table 1, simulated with Re = Re_t.

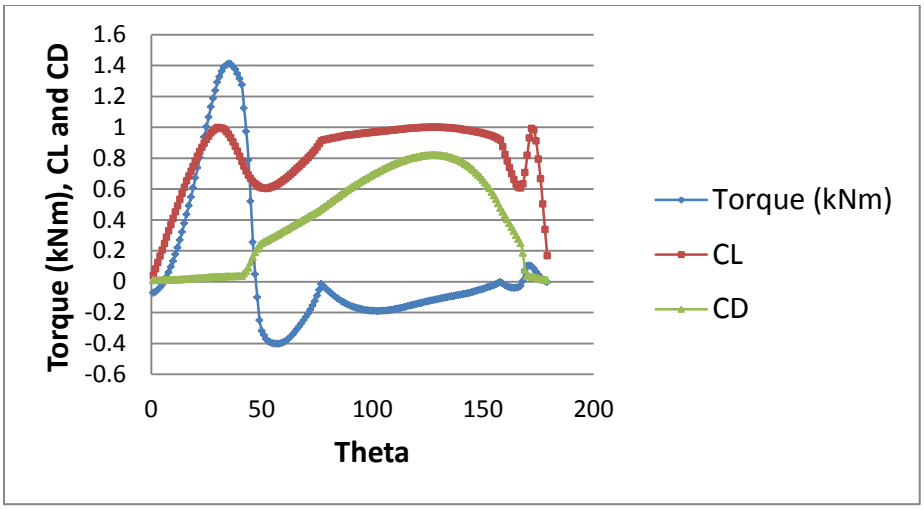

Figure 3-17: Torque vs. Θ for the TSR of 1.65 for the turbine with configuration in Table 3-1, simulated with Re_t. C_L and C_D coefficients are also plotted. For brevity only the upstream section of the turbine has been shown

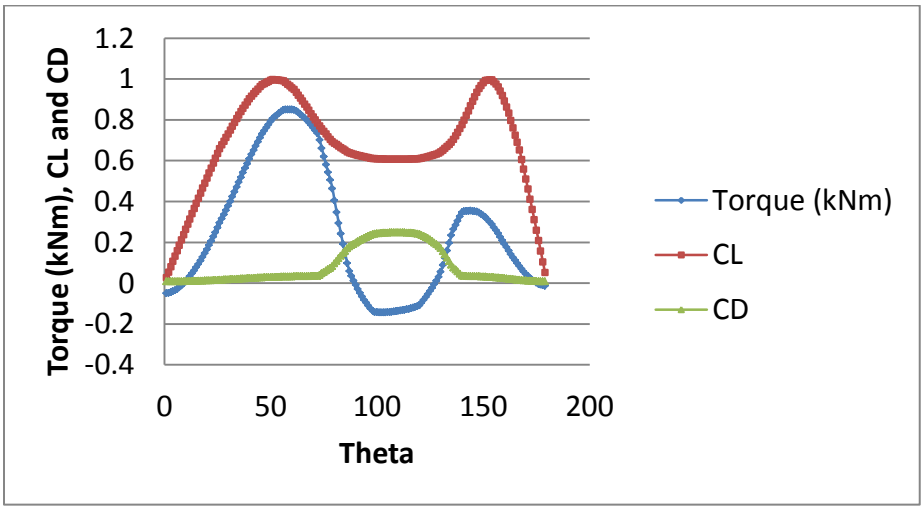

Figure 3-18: Torque vs. Θ for the TSR of 3.09 for the turbine with configuration in Table 3-1, simulated with Re_t. C_L and C_D coefficients are also plotted. For brevity only the upstream section of the turbine has been shown

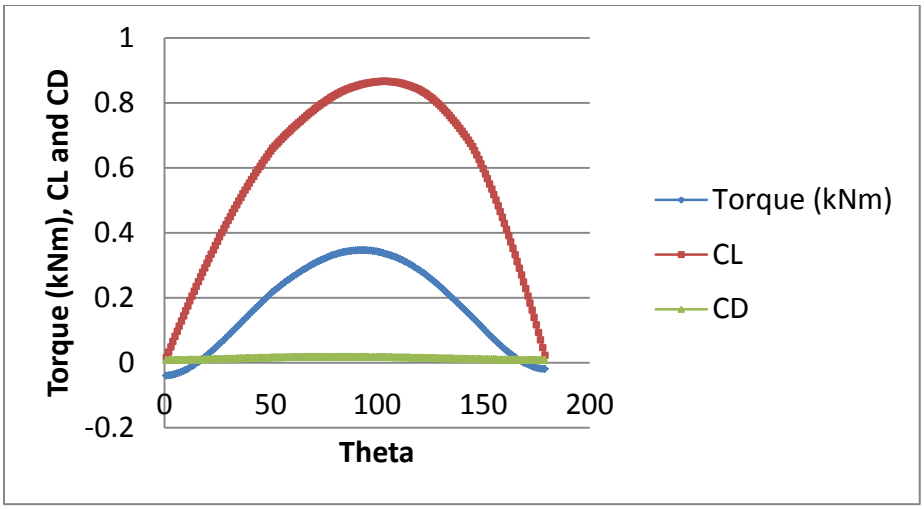

Figure 3-19: Torque vs. Θ for a TSR of 5.63 for the turbine with configuration in Table 3-1, simulated with Re_t. C_L and C_D coefficients are also plotted. For brevity only the upstream section of the turbine has been shown

The self-starting behavior of VAWTs is strongly related to the torque which is generated at each azimuthal angle in the upstream and downstream sections. It is dependent on turbine parameters such as: the airfoil shape, number of blades, solidity, the location of the blade, the blade incidence angle in relation to the wind velocity, and the pitch angle with respect to the wind direction. The term self-starting can has been defined in a number of ways (Dominy, et al. n.d.):

- Ebert and Wood define the starting process as being complete when significant power extraction can be derived from the turbine (Ebert and Wood 1997).
- Kirke says a turbine has self-started if it can accelerate from rest to the point where it starts to produce a useful output (Kirke 1998).
- Lunt adopted a more specific definition which states that a machine has started if it has accelerated from rest to conditions where the blades operate at a steady rotational speed

that exceeds the wind speed, i.e. the tip speed ratio, TSR 1.0 (Lunt 2005).

As has been mentioned previously, one of the draw backs of a VAWT is its inability to self-start even in the presence of high wind speeds (Yao and Habbtamu n.d.). Self-starting is a transient process, and therefore requires a transient analysis of the turbine. The model used in this research is limited in its ability to show the self-starting problems of a VAWT because it models the turbine in steady-state conditions, i.e. the effects of the initial net negative torques that are generated have already been overcome. Figure 3-20 shows the rotational speeds versus time for a VAWT starting from rest. This figure shows the transient nature of a turbine which starts from rest, and accelerates to a steady rotational speed. This tells us that before reaching steady-state the turbine initially goes through several values of TSR, some of which can have very poor torque characteristics. These unfavorable conditions can send the turbine into several states: the turbine blades can experience flow reversal, or it can cause the turbine to oscillate back and forth without actually rotating (in this case the turbine "*rocks"* back and forth) (Dominy, et al. n.d.). This last state was observed in an actual preliminary prototype test conducted here at Michigan State University. At low TSRs, considerably low (often negative) azimuthal torque values are generated. This can be observed in Figure 3-21 for the TSR of 1.65 (and wind speed of 23.8 m/s and an RPM of 125). To understand this behavior, the torque plots are studied closely and the turbine is divided into two sections considered as the locations of blade one and two of a two bladed turbine. For example when blade one is located at 1˚ (upstream), blade two will be 180˚ apart, at 181˚ (downstream). For a TSR of 1.65, at angles of 1˚ and 181˚, the torque is negative, and the turbine starting from rest will accelerate (see Figure 3-21), albeit in the "wrong" direction. Let it be assumed it was designed to rotate in the anticlockwise direction. The torque increases on both blades up to a point when both become positive. When this happens we can

assume that the turbine decelerates from its initial rotational speed. If this condition persists, the angular acceleration in the opposite direction will cause the turbine to rotate in the “correct” clockwise direction. However, blade two soon becomes negative around 213˚, while blade one continues to generate positive torques which peaks at about 33˚. Due to high torques generated by blade one, even with the negative torques on blade two, the turbine may still rotate in the positive clockwise direction.

As blade one approaches 134˚ (a point of negative torque after it had peaked at about 32˚), blade two will be at 315˚ (the peak of blade two’s generated torque). A case now exists where the initial rotational speed starts to decelerate because of a net negative torque. The turbine slows down, and with persistence of this condition it can start to rotate in the opposite direction. When this process is repeated again and again, the turbine experiences the "rocking" phenomenon.

To further illustrate this point, the torques generated on blades one and two are plotted in Figure 3-22 versus Θ ranging from 1˚ to 180˚. This figure shows that from rest both blades generate negative torques which increases to become positive. Then at about 14˚, blade one continues to generate positive torque, but blade two starts generating negative torques, although this torque is not so large. At this angle, there is a net positive torque (Figure 3-22) and the turbine will continue to accelerate. At about 32˚, blade one’s torque begins to drop rapidly, and because negative torque is also being generated by blade two, the turbine will decelerate. This deceleration continues up to around 50˚, where negative torque is being generated on both blades. Around 130˚, blade two starts generating positive torque and blade one is still generating negative torque, which will cause the turbine to start decelerating again. It keeps on decelerating until the torque on blade two is large enough that the net torque generated from both blades is positive. If flow conditions persist and TSR stays low, this process is repeated and hence a

rocking back and forth of the turbine. Start-up is a lesser issue at mid-range TSRs because both blades one and two are always generating positive or negative torques (see Figure 3-23). This explanation assumes this plot is an instantaneous snapshot of what happens during the transient process.

This "rocking" phenomenon was observed in the fluids laboratory at Michigan State University while conducting initial wind tunnel tests on a small straight bladed prototype turbine with two blades. During these tests, the turbine started from very low RPM and TSR for a wind speed of about 7 m/s. With a small push, the turbine started to rotate, but then slowed down, and rotated very slightly in the opposite direction. However, when half of the wind tunnel was blocked the turbine started to rotate consistently, overcoming its initial startup problem. It then accelerated until it reached steady-state conditions. When half of the tunnel was blocked the flow was blocked from seeing the second blade. This reduced the effect of negative torque generated on the second blade.

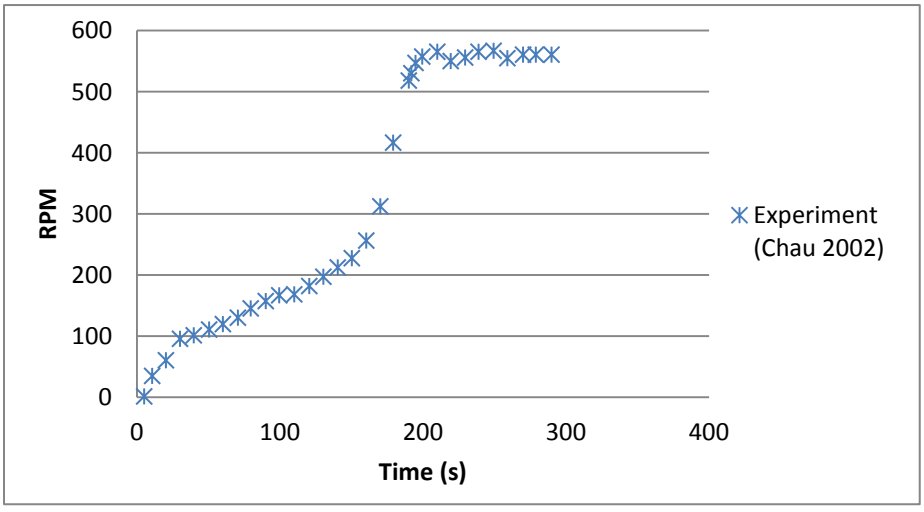

Figure 3-20: RPM vs. time obtained from experiments of a VAWT (Dominy, et al. n.d.)

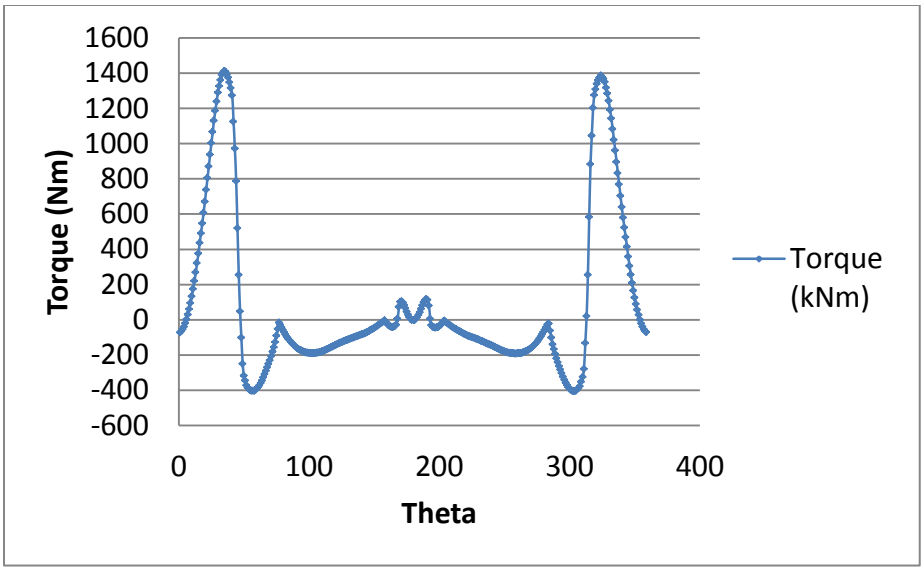

Figure 3-21: Torque characteristic of a VAWT for the TSR of 1.65

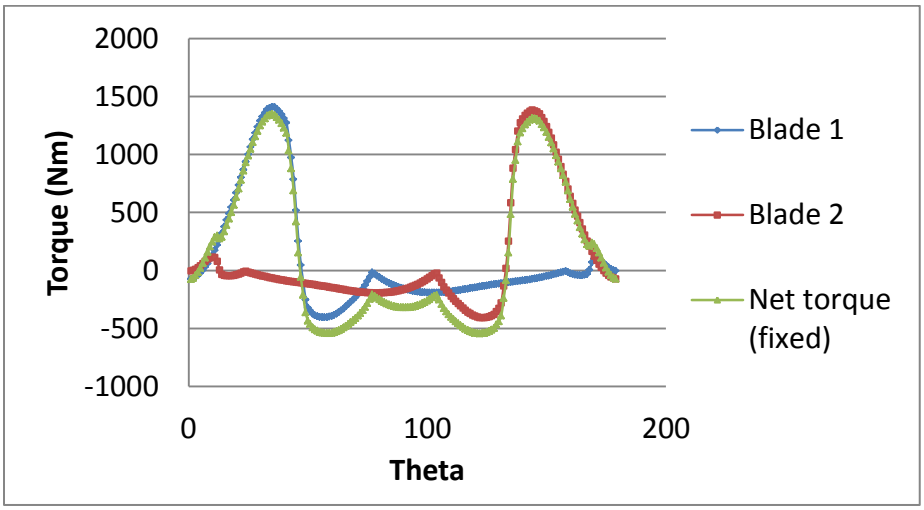

Figure 3-22: Torque characteristic of a VAWT for the TSR of 1.65. Torques on both blades have been plotted on a Θ axis going from 1˚ to 180˚

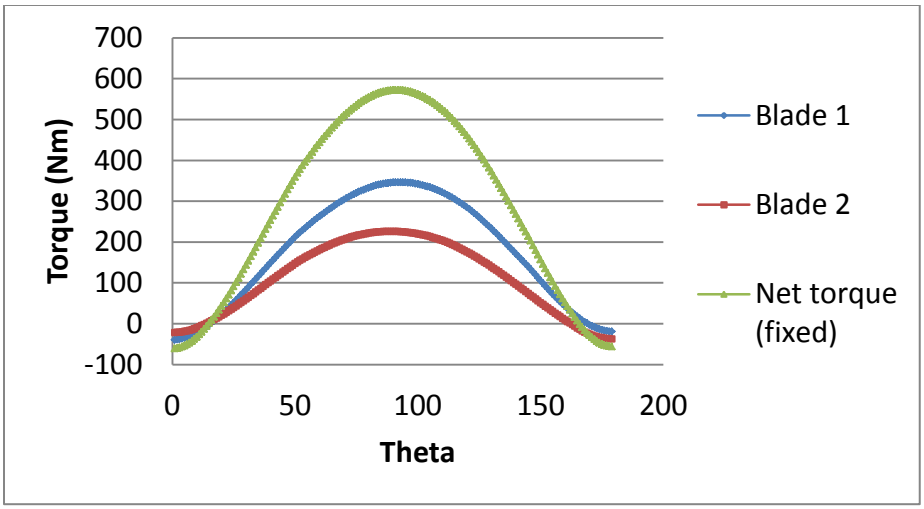

Figure 3-23: Torque characteristic of a VAWT for the TSR of 5.63. Torques on both blades have been plotted on a Θ axis going from 1˚ to 180˚

3.2.4 Effects of Airfoil Shape

This section investigates the effects of various airfoil shapes on turbine performance. Four different airfoils are considered, three of them are symmetric airfoils, and one asymmetric airfoil. Figure 3-24 and Figure 3-25 show the geometry of the four different airfoils studied labeled as: NACA 0012, NACA 0015, NACA 0021, and S809. The data for the symmetric airfoil comes from experiments at Sandia National Laboratories. The asymmetric airfoil studied is one that has been optimized for HAWT at the National Renewable Energy Laboratory (NREL).

Figure 3-26 and Figure 3-27 show the performance of VAWTs using different airfoils. It shows that with an increase in the airfoil thickness there is an increase in the efficiency of the system at lower TSRs; however, for mid to high TSRs, the performance of the turbine is better for thinner airfoils. The performance of the asymmetric airfoil overall was inferior, even if a higher simulation Re was used (the experimental data available was only for a Re of 750,000 as

opposed to 537,943 used with the symmetric turbines). The maximum thickness of asymmetric airfoil, S809, is comparable to that of the symmetric 0021 airfoil, yet the performance of the asymmetric airfoil is lower than that of other airfoils.

In Figure 3-28 the raw C_L and C_D data for the 0012 and 0021 airfoils are shown. Figure 3-29 shows the variation of angle of attack with Θ for TSRs of 2.71 and 5.63 in the upstream. These plots are presented to explain why turbines with different airfoils can have significantly different performance. In Figure 3-29, it is observed that there is only a slight difference between the α values for the same TSRs. The C_L/C_D ratio in Figure 3-30 help to explain why at low TSRs, turbines with the 0012 airfoil perform better than that with 0021, and vice-versa at mid to high TSRs. Figure 3-30 and Figure 3-29 indicate that when stall angles are approached, the aerodynamic efficiency of the turbine drops significantly. At TSR of 2.71, the induced flow over the airfoil is in stall range, explaining why the performance of the turbine at this TSR is poor compared to that at TSR of 5.63. The results for TSRs of 2.71 and 5.63 over the mid-range of Θ show that there is a direct correlation between the *Cp* and the overall aerodynamic efficiency.

The consideration to use a thinner or thicker airfoil may be controlled by, and based on the blade weight. This also determines the base support required to holdup the entire structure. From a manufacturing stand point, it is easier to produce a symmetric airfoil instead of a non-symmetric one.

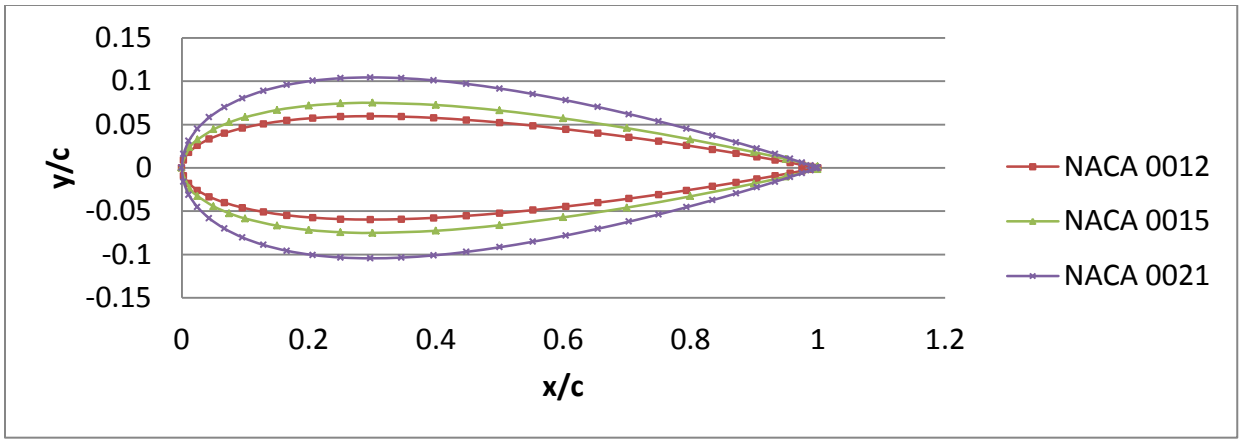

Figure 3-24: The shapes of symmetric airfoils studied – NACA 0012, NACA, NACA 0015, and NACA 0021 (Malcolm's Human Powered Aircraft Site n.d.)

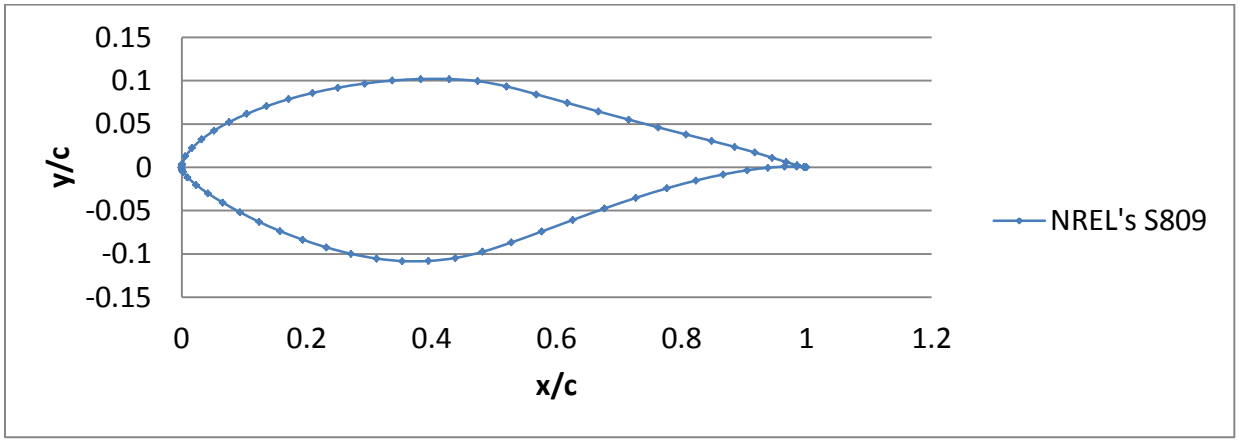

Figure 3-25: The shape of the asymmetric airfoil studied – NREL's S809 (UIUC Airfoil Data Site n.d.)

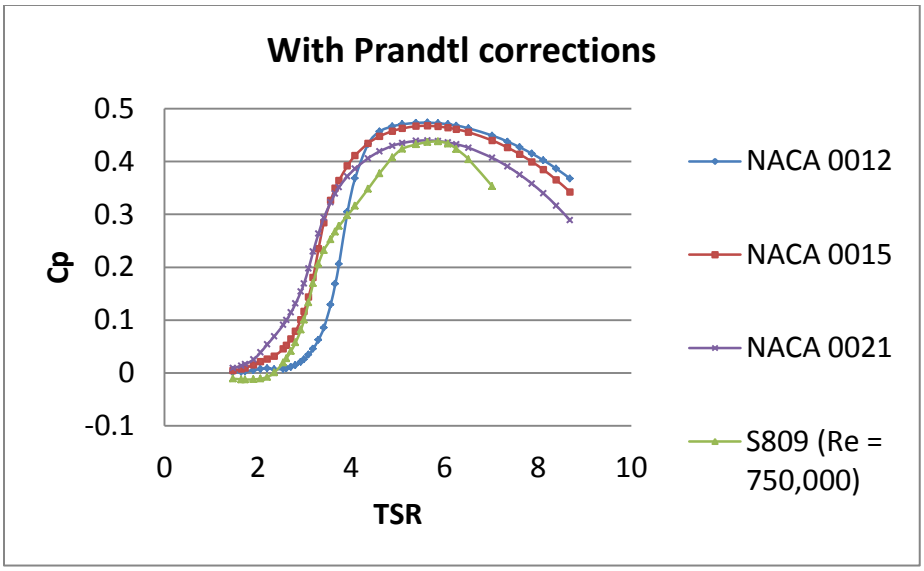

Figure 3-26: *Cp* vs. TSR for the four different airfoils studied

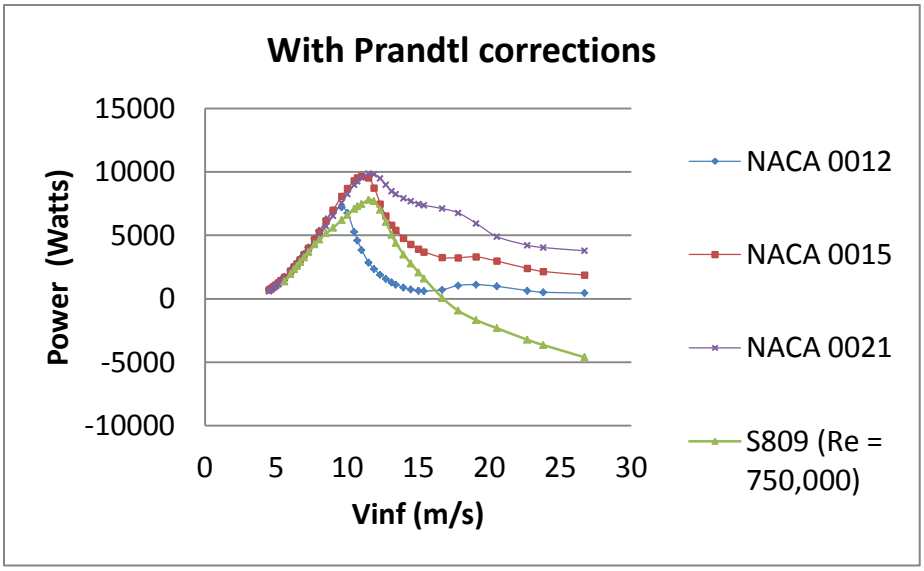

Figure 3-27: Power vs. wind speed V_∞ for the four airfoils studied

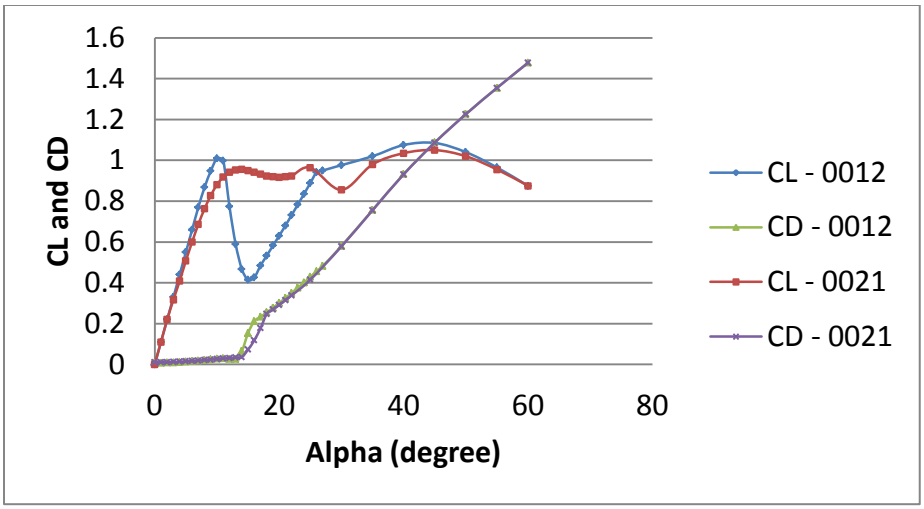

Figure 3-28: C_L and C_D vs. Θ for the NACA 0012 and NACA 0021 airfoils

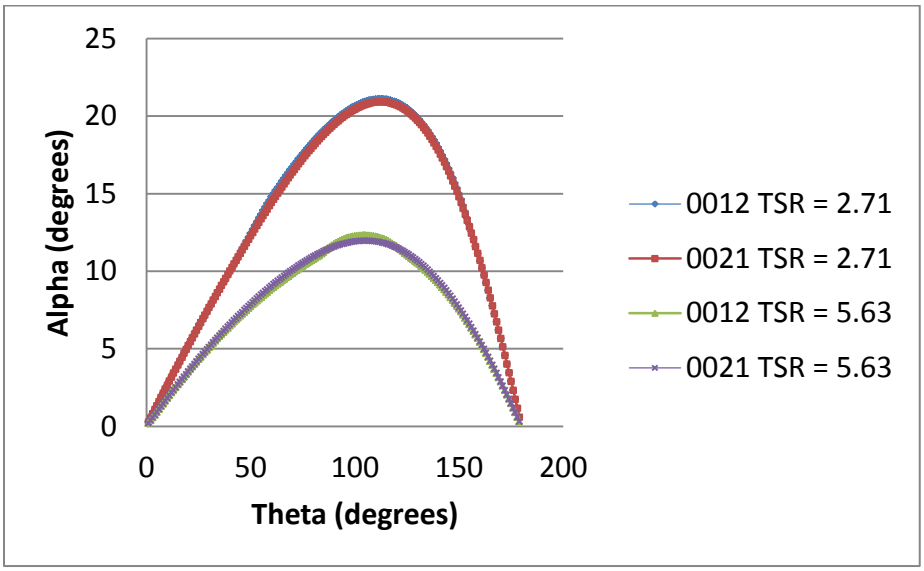

Figure 3-29: The angle of attack vs. Θ for the NACA 0012 and NACA 0021 airfoils at two different TSRs. The plots are for the upstream section only

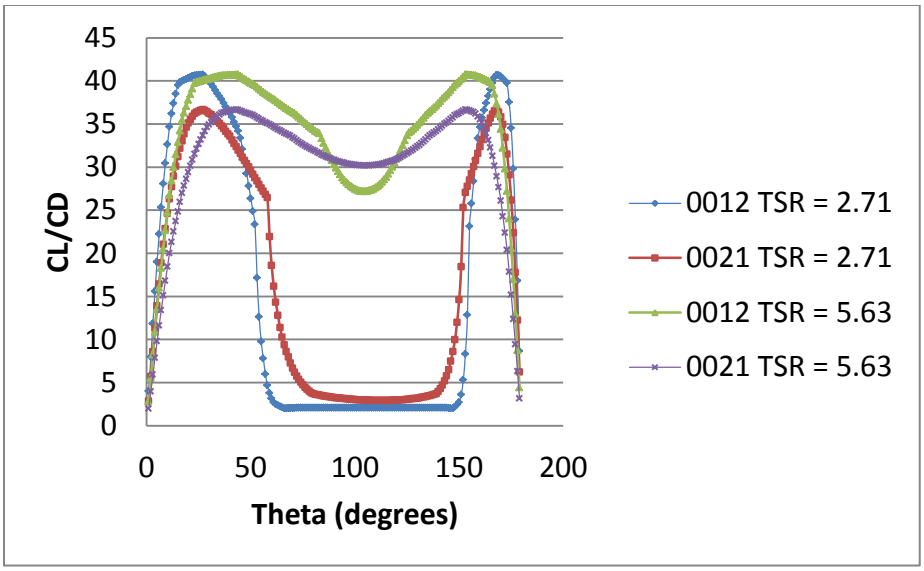

Figure 3-30: C_L/C_D vs. Θ for the NACA 0012 and NACA 0021 airfoils at two different TSRs

3.2.5 Effects of Solidity

Solidity is the ratio of the total turbine planform area to the total swept area. This parameter has a significant effect on the turbine's performance. Solidity, σ, of a VAWT can be defined as:

$$\sigma = \frac{NCH}{RH} = \frac{NC}{R} \qquad \text{Eq. 3.17}$$

Designers commonly change the solidity of a turbine by changing the number of blades. High solidity turbines are used for high torque applications. These turbines generally rotate more slowly. Figure 3-32 illustrates that a turbine with high solidity has a high initial starting torque at low TSR. However, in high speed wind applications turbines which operate at the lowest possible torques are more desirable. The reason for this is easier startup and cheaper gearboxes. Figure 3-31 shows the *Cp* versus TSR for a turbine simulated with a chord length of 0.10 m, and different solidities. The solidity was changed by varying the number of blades in the turbine. There is a key observation that can be made from Figure 3-31 (Burton, et al. 2001): a low

solidity turbine produces a broad, flat performance curve, i.e. *Cp* will change very little over a wide range of TSRs; however, the maximum *Cp* is lower because the drag losses are higher (drag losses are roughly proportional to the cube of the tip speed ratio). In turn, turbines with a high solidity produce a narrower performance curve with a sharper peak, hence making the turbine very sensitive to changes in TSR.

A heavily loaded turbine is said to have a high solidity and for the same value of solidity, a heavily loaded turbine is considered to have a high TSR. As mentioned earlier, the performance of momentum models for heavily loaded turbines is poor. This affects the code's ability to produce a converged solution for higher values of solidity and/ or TSR.

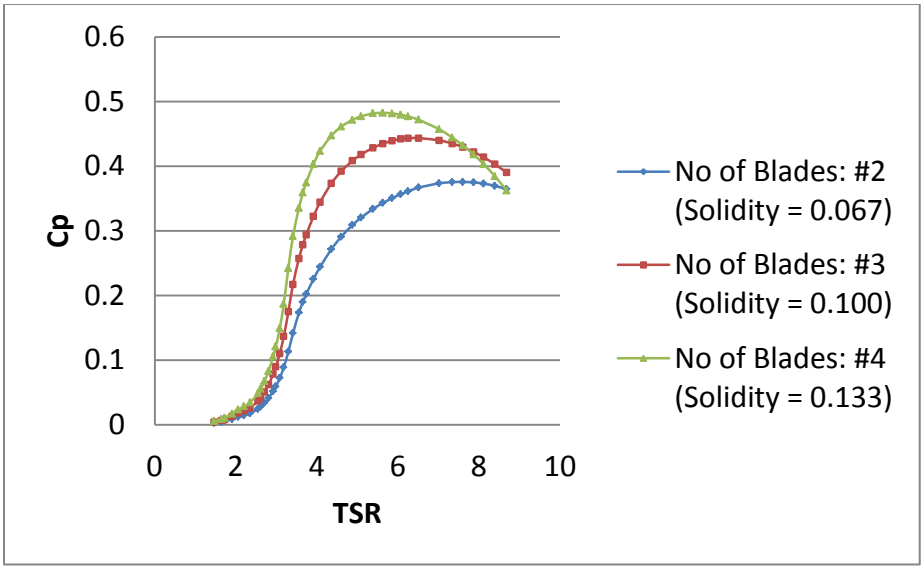

Figure 3-31: *Cp* vs. TSR for turbines with different solidity

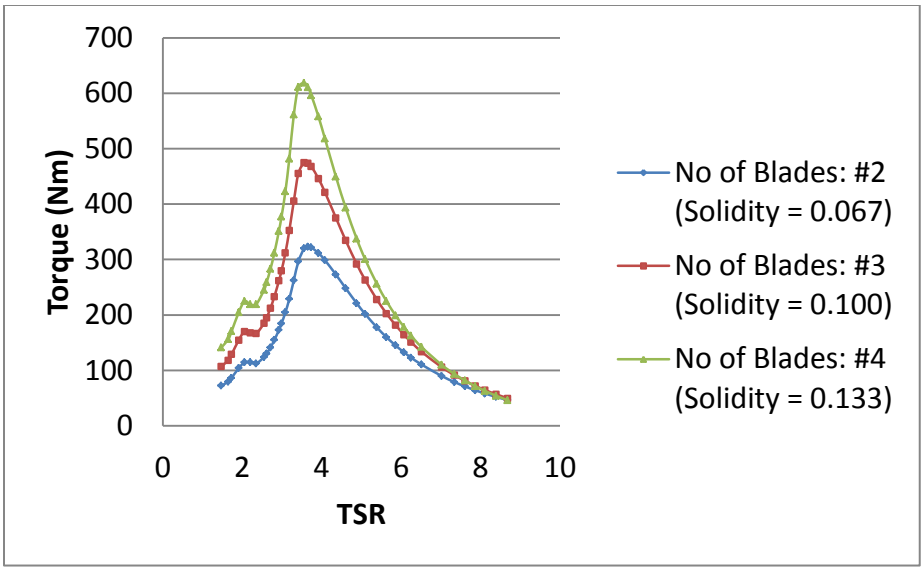

Figure 3-32: Torque vs. TSR for turbines with different solidity

3.2.6 Effects of Wind Shear

The increase in wind velocity with elevation, which is characterized by the wind shear pattern due to the atmospheric boundary layer must be considered for large turbines which extend several meters above ground. A simple model commonly used to simulate the wind shear is the power law model:

$$V(H) = V_{EQ}\left(H / H_{EQ}\right)^{\varepsilon} \qquad \text{Eq. 3.18}$$

The subscript "EQ" are used for variables at the equator (mid-span) of the turbine, and ε represents the *Wind Shear Exponent.* This exponent determines the slope of the wind profile. Figure 3-33 shows the wind distribution at different heights with an equatorial speed of 26.72 m/s.

Figure 3-34 shows the variation of *Cp* with TSR for the turbine simulated with and without wind shear. The conditions for open water and building landscape are compared to a case without

wind shear. From this figure we can conclude that with the presence of wind shear the amount of power available to the turbine increases. Also it can be seen that the turbine performs better if it is placed in a more open terrain (e.g. a smooth, level, grass-coverage) as opposed to one around a lot of obstacles such as buildings. This is why wind farms are often located in open fields far away from city areas. Table 3-2 presents some of the wind model's exponents that are typically used for various terrains. These values are obtained modeling.

Table 3-2: Wind shear exponents for various terrains (The Engineering Toolbox: Wind Shear n.d.)

Terrain	Wind Shear Exponent (ε)
Open Water	0.10
Smooth, level, grass-covered	0.15
Row crops	0.20
Low bushes with a few trees	0.20
Heavy trees	0.25
Several buildings	0.25
Hilly, mountainous terrain	0.25

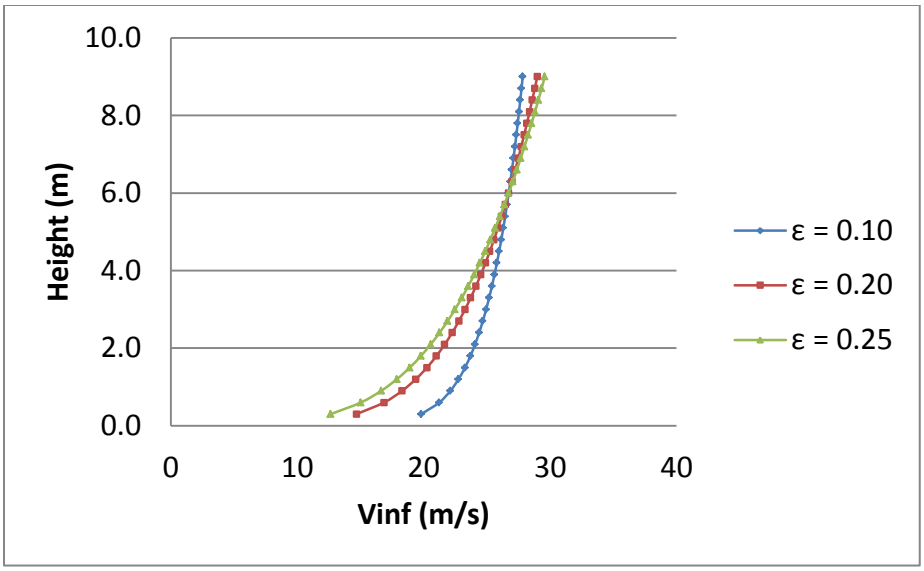

Figure 3-33: Wind speed variations with the height for three different wind shear exponents

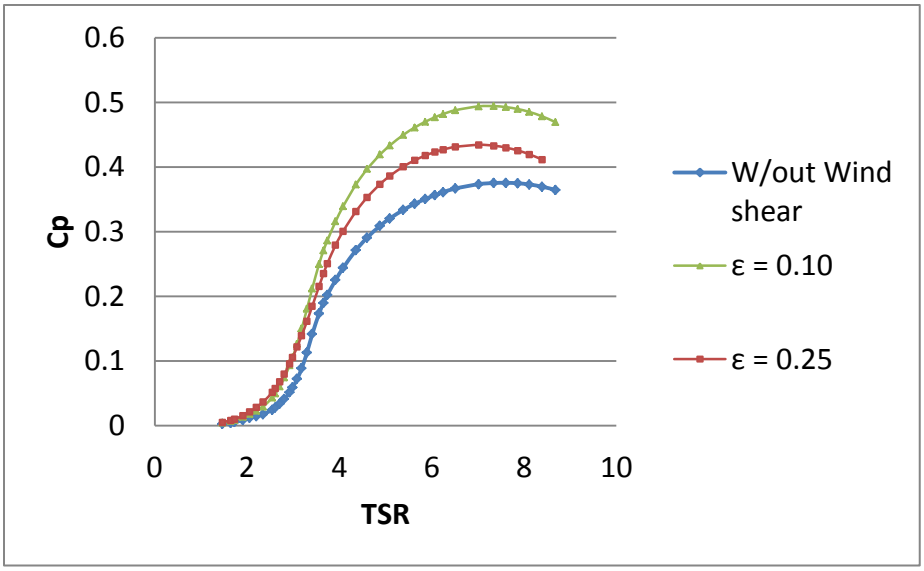

Figure 3-34: *Cp* vs. TSR for a turbine with and without wind shear. The wind shear exponents used were 0.1 and 0.25

Chapter 4: VAWT with Variable Blade Pitch

4.1 Introduction

All simulations carried out so far have been for a turbine with fixed blade pitch set to zero degree. A pitch angle of zero degree corresponds to the chord line of the airfoil being aligned with the tangent of the circular path the airfoil makes as it rotates. Based on the flow conditions and geometry of the turbine and blades, the torque characteristic and hence power and performance can be negatively affected. This section aims to study how the performance of a turbine can be controlled by varying the blade pitch. Also by varying the pitch angle, we can potentially solve the self-starting problem that hinders the operation of VAWT. To carry out this study with the cascade model, the equations of W_{0u}, α_{0u}, W_{0d}, and α_{0d} must be modified to include the pitch angle:

$$\alpha_0 = \tan^{-1}\left[\frac{V_n}{V_c}\right] = \tan^{-1}\left[\frac{[R\omega\tan\beta + V_d\sin(\theta-\beta)]\cos\phi}{\mu\left(R\omega/\cos\beta\right) + V_d\cos(\theta-\beta)}\right] \quad \text{Eq. 4.1}$$

$$W_0 = \sqrt{V_c^2 + V_n^2} \quad \text{Eq. 4.2}$$

In the above equations, variables with subscripts "*c*" and "*n*" represent the upstream and downstream values of the chord-wise and normal velocity components. For β equal to zero, the original equation is recovered.

Other researchers have used various methods to optimize the turbine by varying the pitch. This includes the work by I. Paraschivoiu which optimizes the turbine by creating the best variation in pitch angle through a genetic algorithm (Paraschivoiu, Trifu and Saeed 2009). The second

approach optimizes the turbine by restricting the turbine's blade to have a pre-specified angle of attack (Staelens, Saeed and Paraschivoiu 2003). These two methods have their merits; however, the current study uses a unique optimization approach by finding the best pitch angle at every azimuthal angle which gives the turbine the best torque.

4.2 Results and Discussion

Before the results of the current research are presented, it is important to understand how the optimization is performed. This optimization technique uses the same cascade model used in previous section. In this section only a one blade, straight-blade wind turbine is considered. The reason for choosing this setup is to simplify the aerodynamic problem, and limit the errors that can be associated with other blades interacting with each other. This is especially important due to simplicity of the model and its inability to capture the flow physics. During simulations, for every azimuthal angle, the blade pitch is varied from 0° to a maximum specified angle of 90° and the results recorded. With every pitch angle selection, the iteration is done until convergence is achieved before advancing to the next Θ angle. For example, if $\Theta = 1^{\circ}$, at the start of iteration, $\beta = 0^{\circ}$ is selected, and with a guess of V_d, the steps explained in the previous chapter are taken until there is convergence in V_d. Once convergence is reached for the chosen Θ, β is increased by one degree and the process is repeated until $\beta = 90^{\circ}$. After this, Θ is advanced by one degree, and then the pitch angle variation is repeated; this is done for all Θ from 0° to 360°. At every level of convergence, all variables are stored in an array to be used later for optimization purposes. After this raw data has been obtained, the optimization is performed based on the tangential force or torque. For every azimuthal angle, the pitch angle that generated the highest tangential force/ torque is selected, and the corresponding values of α, β, normal force, C_L, and C_D are recorded.

For this analysis, three wind speeds are used: 6, 7, and 8 m/s. These velocities have been selected because they represent typical velocities experienced by wind turbines in the field. All calculations are conducted with fixed Reynolds number of Re = 80,000.

The torque characteristics for the fixed and variable pitch turbines for the three wind speeds are plotted in Figure 4-1, Figure 4-2, and Figure 4-3. As expected, variable pitch turbines generate significantly more torque throughout the turbine's operation. The main observations are the higher values of positive torques for variable pitch blades, and the fact that the turbine which varies its blade orientation also has the advantage of self-starting without any difficulties. These plots represent the best torque that the optimization process was able to obtain, within the limitations of the code. Figure 4-3 shows the torque variation with angular position for the variable pitch case to have some spikes; this is due to some convergence issues.

Based on the optimizations performed, the improvements in *Cp* for these three wind speeds are computed and shown in Table 4-1.

Table 4-1: Turbine efficiency for fixed and variable pitch turbines

V_∞	***Cp* (fixed)**	***Cp* (variable)**
6 m/s	0.2896	0.7944
7 m/s	0.2502	0.4951
8 m/s	0.0487	0.2092

From this table it can be seen that there are definite improvements in efficiency of the system when the blade pitching is optimized.

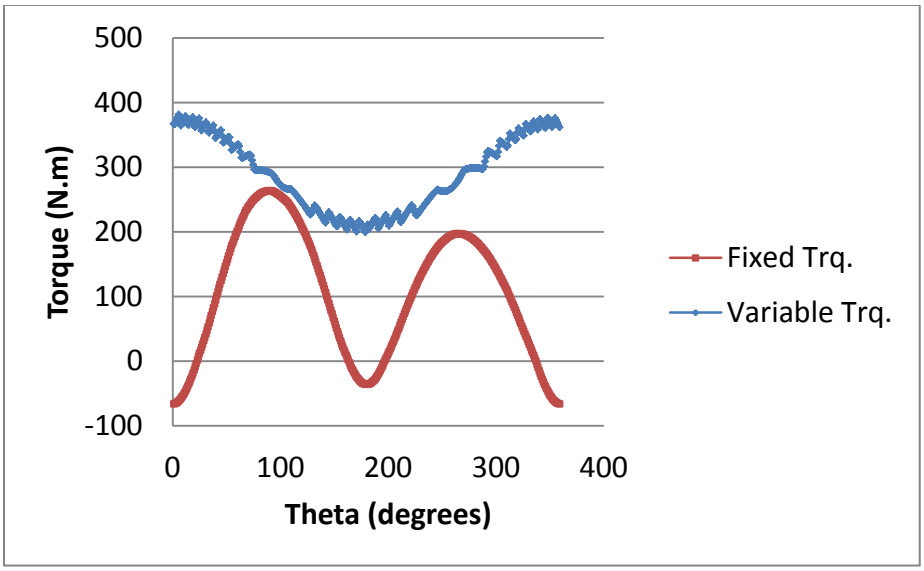

Figure 4-1: Torque vs. Θ for simulations with fixed and variable pitch blades. These plots are for wind speed V_∞ of 6 m/s

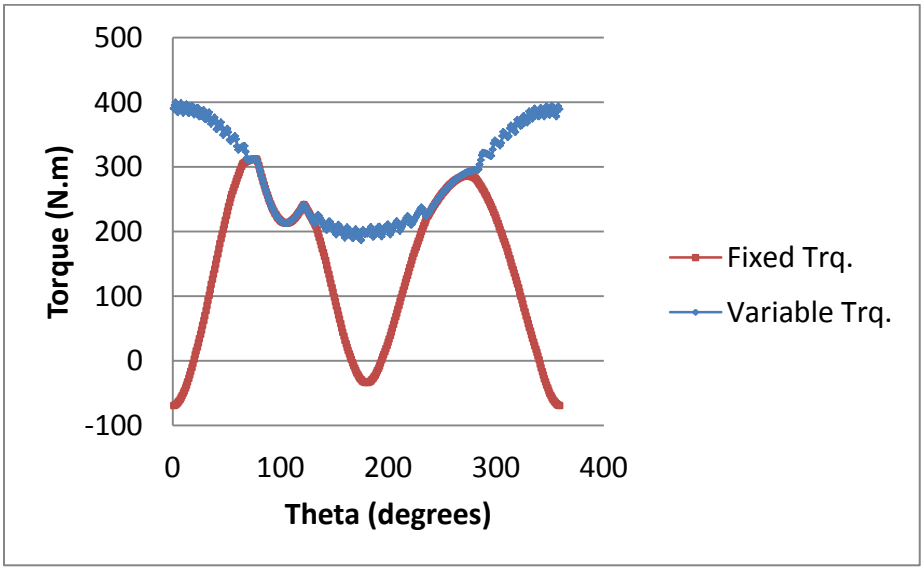

Figure 4-2: Torque vs. Θ for simulations with fixed and variable pitch blades. These plots are for wind speed V_∞ of 7 m/s

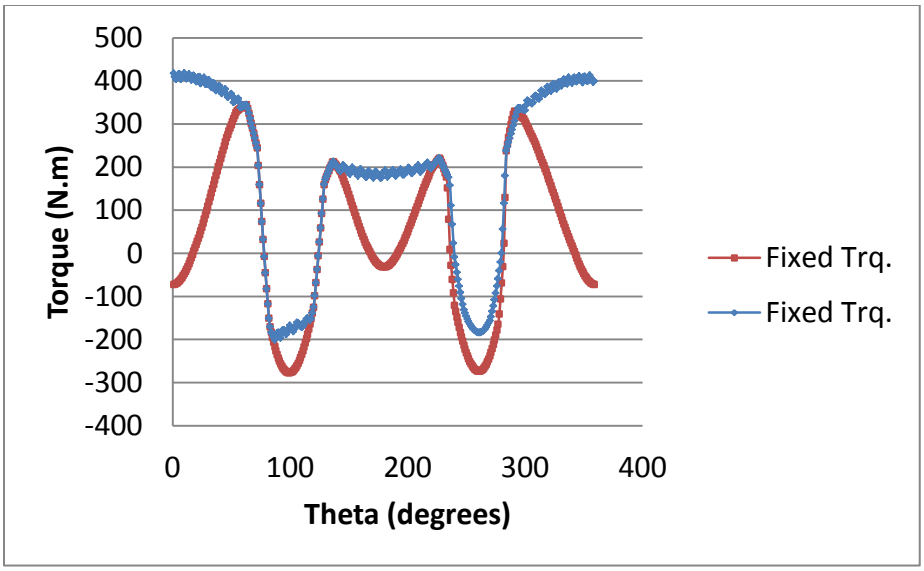

Figure 4-3: Torque vs. Θ for simulations with fixed and variable pitch blades. These plots are for wind speed V_∞ of 8 m/s

By observing C_L and C_D against angle of attack, α, it is possible to infer what angles the airfoil's relative velocity must make to get the optimal performance: from basic aerodynamics it is known that C_L increases linearly with α until stall. Figure 4-4 shows the angle of attack variations with the angular positions of the turbine for a wind speed of 6 m/s. At this wind speed relatively high efficiencies are achieved, even for a turbine with fixed pitch. For a turbine to give the optimal performance, it will be essential that it avoids stall conditions and be at an angle of attack that gives the best lift based on the input conditions (typically occurs just before the stall). From the simulation, for all Θ and β combinations, the maximum angle of attack was 32.34˚ and the minimum was -30.88˚ (based on the simulated flow condition, and geometry of turbine). Looking at Figure 4-4 it can be observed that the angle of attack varies between 8.08˚ and 9.34˚ (at the upstream section), and -9.34˚ and -8.04˚ (at the downstream section) for the variable blade pitch case. Figure 4-5 shows the plot of α against C_L for Re of 80,000. This figure has been

plotted within the range of maximum and minimum α observed in our simulation for the given flow conditions and geometry. It can be observed that for positive α angles, between 7˚ and 9˚ reasonably high values of lift are generated that will allow the turbine to generate high powers. A similar conclusion can also be made for negative α angles, between -7˚ and -9˚ which also generates reasonably high lifts.

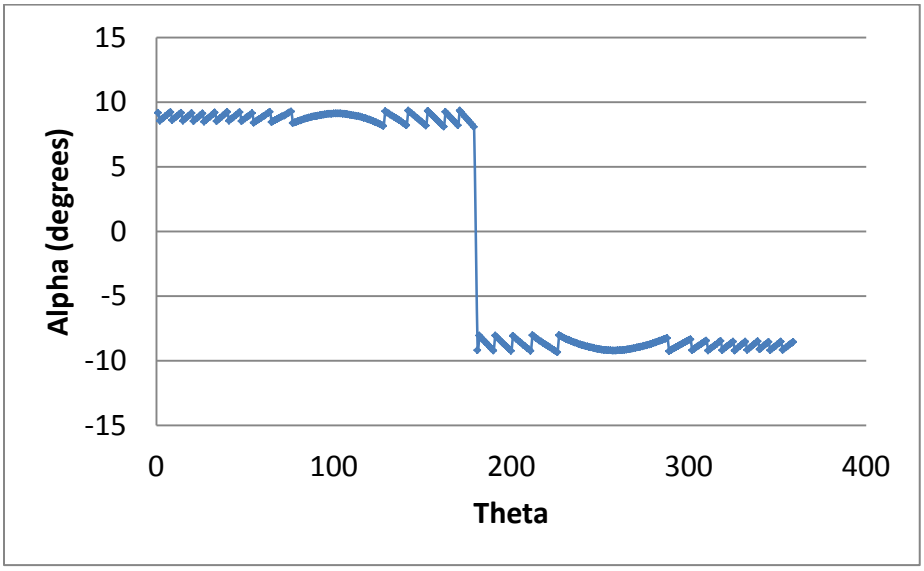

Figure 4-4: The variation of angle of attack α against Θ using the optimization scheme. This plot is for a wind speed V_∞ of 6 m/s

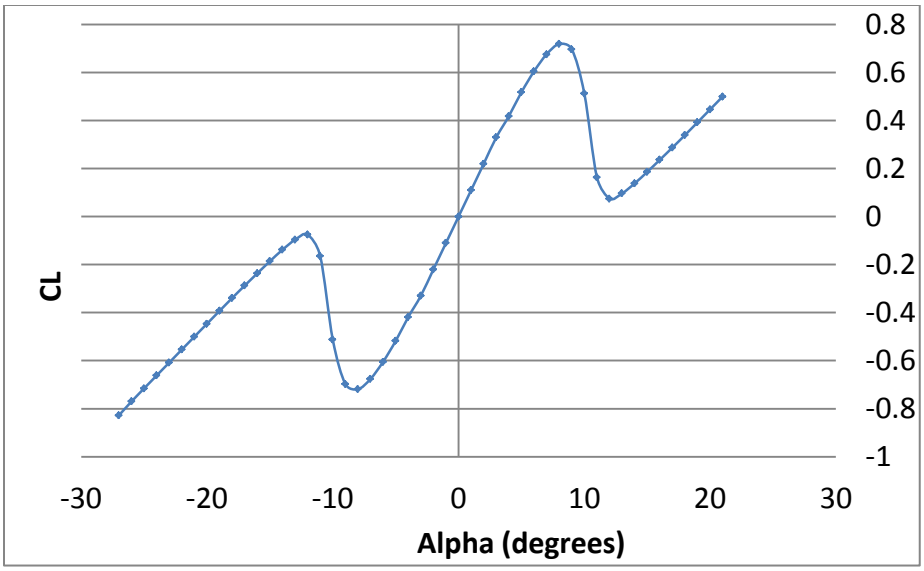

Figure 4-5: C_L vs. angle of attack α for Re = 80,000

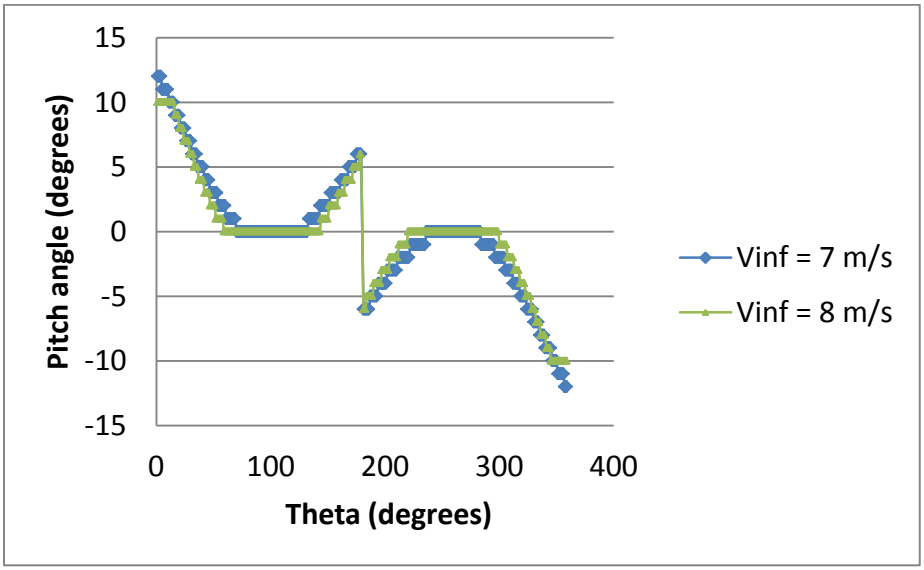

Figure 4-6: Pitch angle vs. Θ for the variable pitched blade at two wind speeds to show the differences in pitch angle needed to optimize the turbine

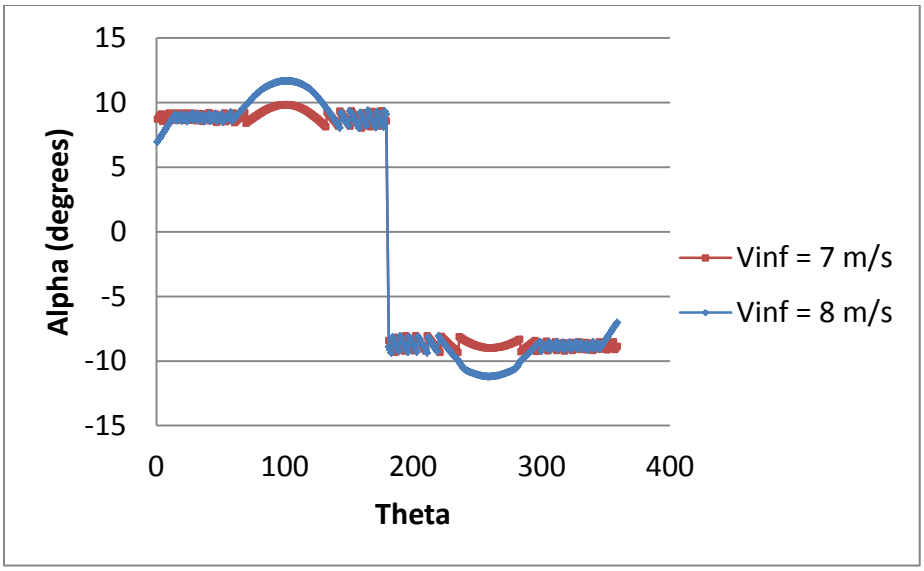

Figure 4-7: Angle of attack α vs. Θ for the variable pitch blades

For the optimized variable pitch turbine there is a sharp (step) change in angles between the upstream and downstream sections of the turbine (Figure 4-6 and Figure 4-7). These step changes may be mechanically unfeasible to achieve; therefore, in order to soften this transition a tangent hyperbolic smoothing technique has been applied to the pitch variations. Figure 4-8 shows the results obtained with this modification.

In summary, it is believed that a variable pitch system should be used to start the vertical axis wind turbines, but once steady-state conditions has been achieved, it may be "turned-off" to reduce the number of moving parts, which can constitute further maintenance issues. If moving mechanisms for variable pitching is not an issue, the variable pitch system may be operated for all operating conditions to always obtain higher power outputs and improved efficiencies. To achieve this however, a control mechanism which monitors and reacts to inflow conditions must be developed.

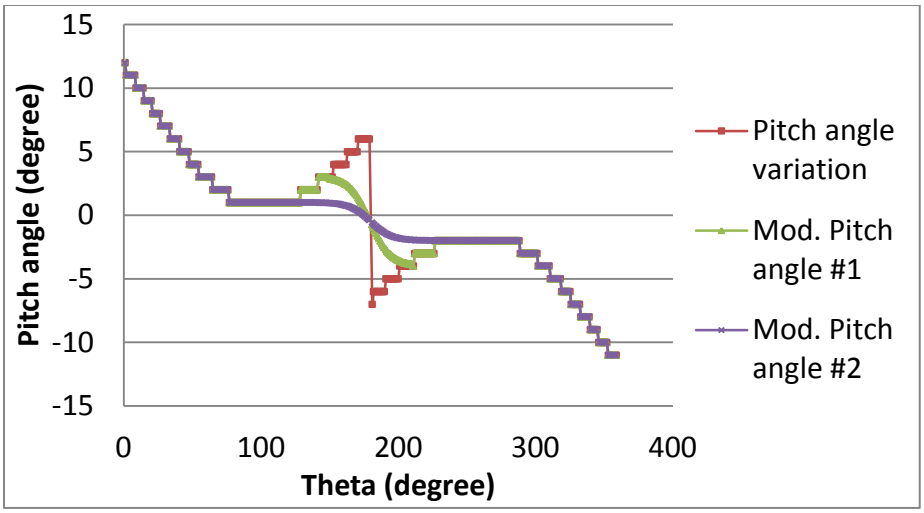

Figure 4-8: Pitch angle vs. Θ for the variable pitch blade with the tangent hyperbolic smoothing being applied to optimized pitch results (V_∞ = 6 m/s)

Chapter 5: Horizontal Axis Wind Turbines

5.1 Introduction

This chapter is focused on the results we have obtained from simulations using FAST for horizontal axis wind turbines (HAWT). The specifications for the simulated HAWT are given in Table 5-1.

Table 5-1: The geometry and parameters of the simulated HAWT

Parameter	Value
Rotor diameter	10.00 m
Hub Height	12.19 m
Rated Power	20 kW
Blade chord length	Tapered
Airfoil type	S809
Number of blades	2
Blade Length	5.03 m
Initial blade pitch	4.815˚
Simulation RPM	71.9

The effects of tip losses as well as hub losses were included in these calculations. As mentioned before, the subroutine, AeroDyn, performs the aerodynamic calculations on a spanwise basis. Here the plots are shown for the mid-blade element (9^{th} out of 18 sections). Even though each individual section has a different twist angles, in this chapter, the blade pitch represents that of the entire blade section. Lastly, note that the Reynolds numbers shown in the results are to the sixth power.

5.2 Effects of Wind Speed

From the FAST simulations and results in Figure 5-1 to Figure 5-8 we observe that:

- As the wind speed increases, the power also increases until the speed reaches a peak value, after which the power starts to reduce. Furthermore, as the RPM increases, the peaks are reached at higher wind speeds.
- The average (steady-state) C_L typically increases with wind speed. However, C_L values are generally lower for higher RPMs.
- The average (steady-state) C_D value increased with wind speed. The magnitude of C_D also reduces with increasing RPM.
- *Cp* values reduced with increasing wind speeds, and the magnitude of the *Cp* increased with increasing RPM.
- The angle of attack increased with the increasing wind speed, and the magnitudes reduced with increasing RPMs.
- As the wind speed increased, the dynamic pressure also increased, and its magnitude also increased with increasing RPM.

- Figure 5-7 illustrates the aerodynamic efficiency, C_L/C_D, of the turbine. The turbine is most efficient at lower wind speeds, and reduces in efficiency with increasing wind speed.

Note: The graphs below simulate a wind turbine with blade pitch angle of 4.815˚ and a nacelle yaw angle of 0˚. The graphs show different parameters at three at three different RPM values: 50, 71.9 and 85.

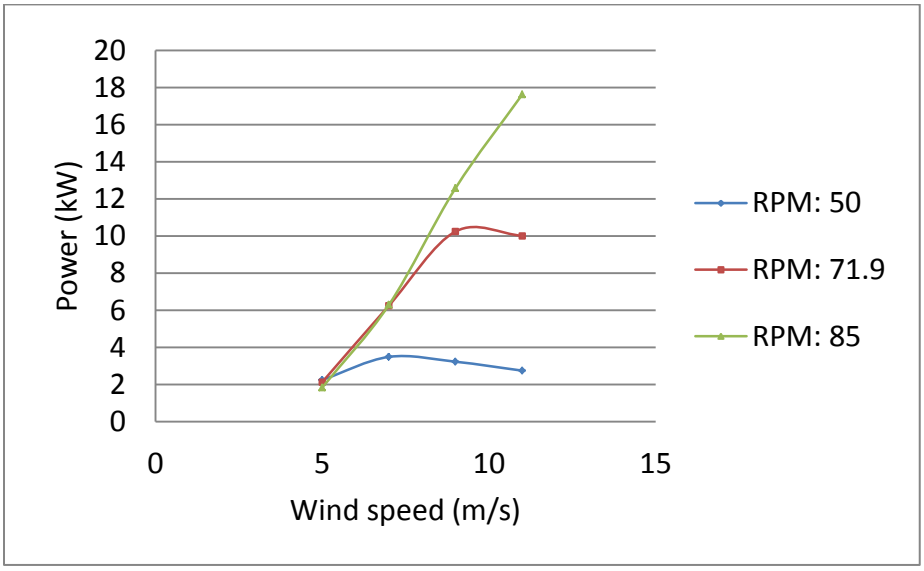

Figure 5-1: The variation of power with wind speed for three RPM values

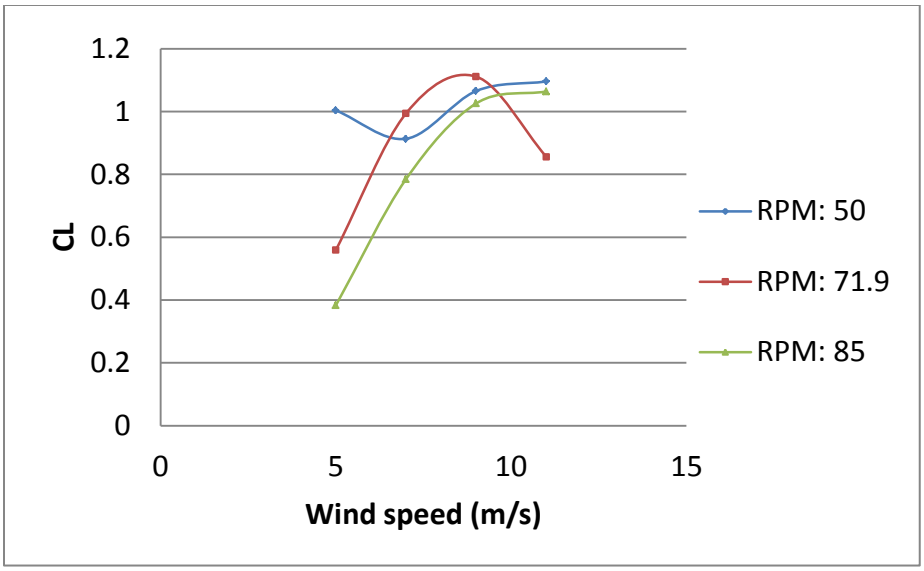

Figure 5-2: Averaged C_L at different wind speeds and RPM values

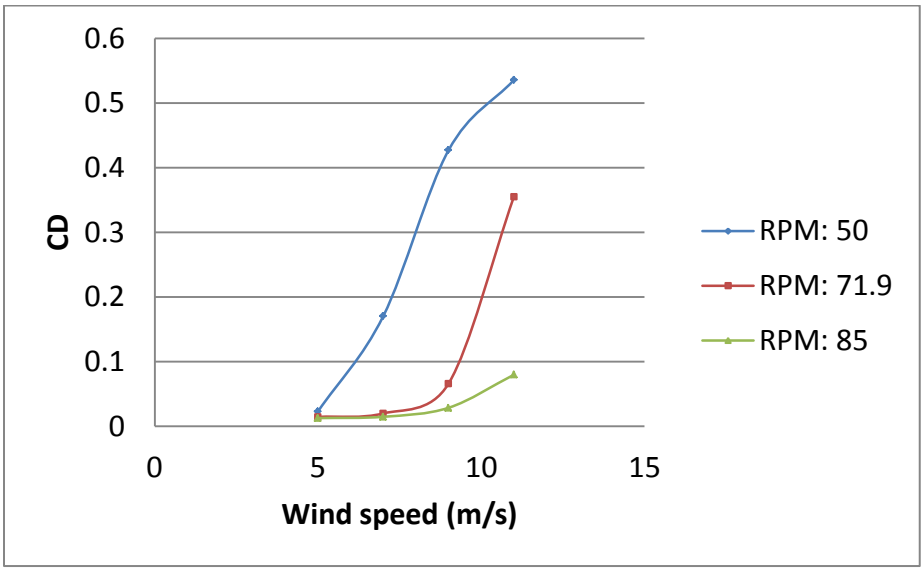

Figure 5-3: Averaged C_D at different wind speeds and RPM values

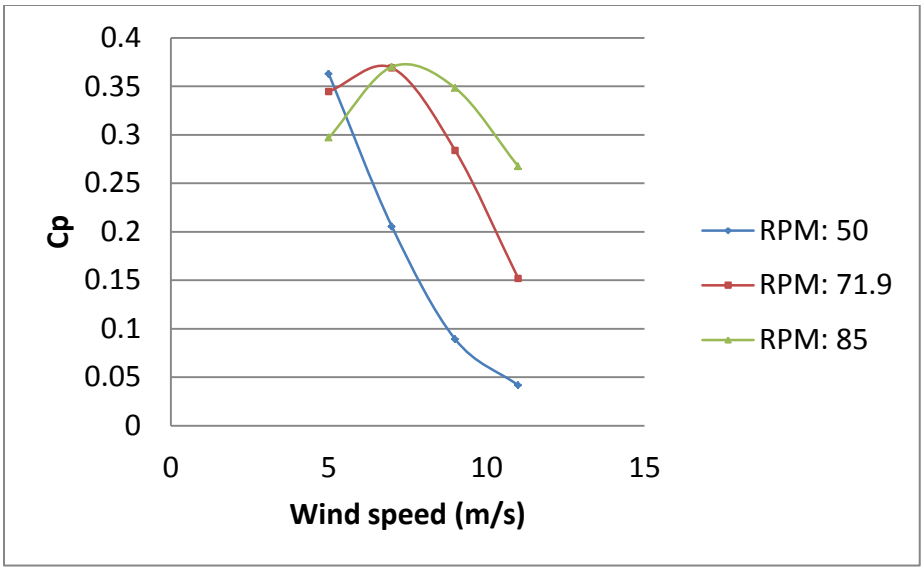

Figure 5-4: The coefficient of power C_p at different wind speeds and RPM values

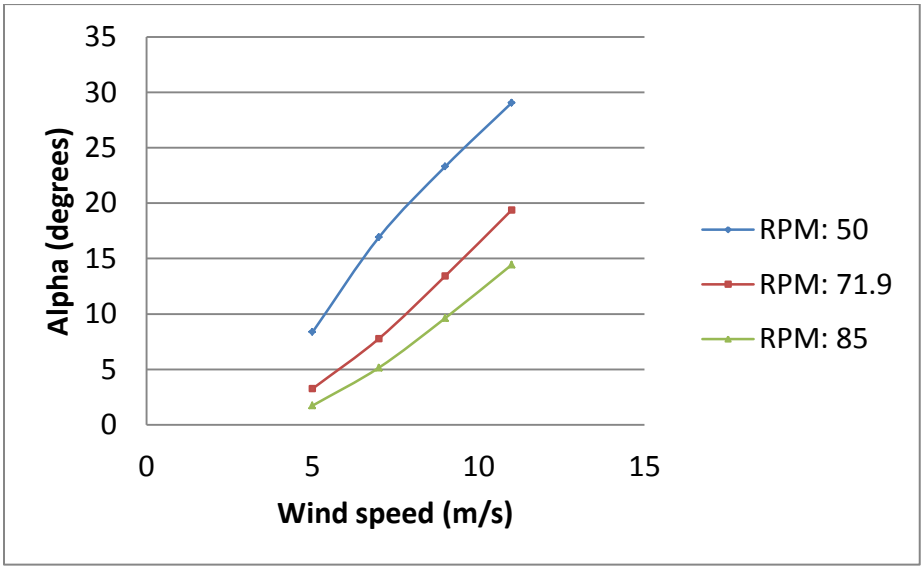

Figure 5-5: The angle of attack vs. wind speed for different RPM valued

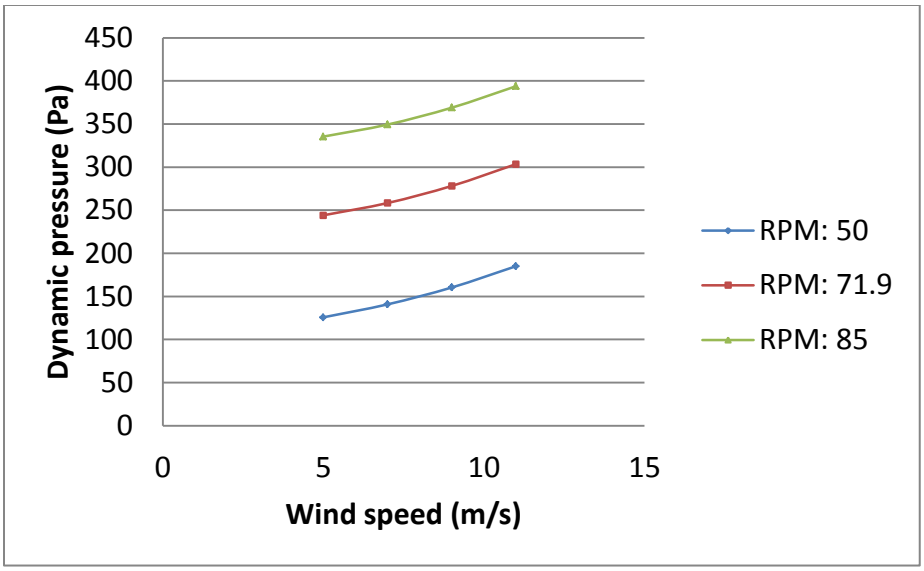

Figure 5-6: The dynamic pressure vs. wind speed for different RPM valued

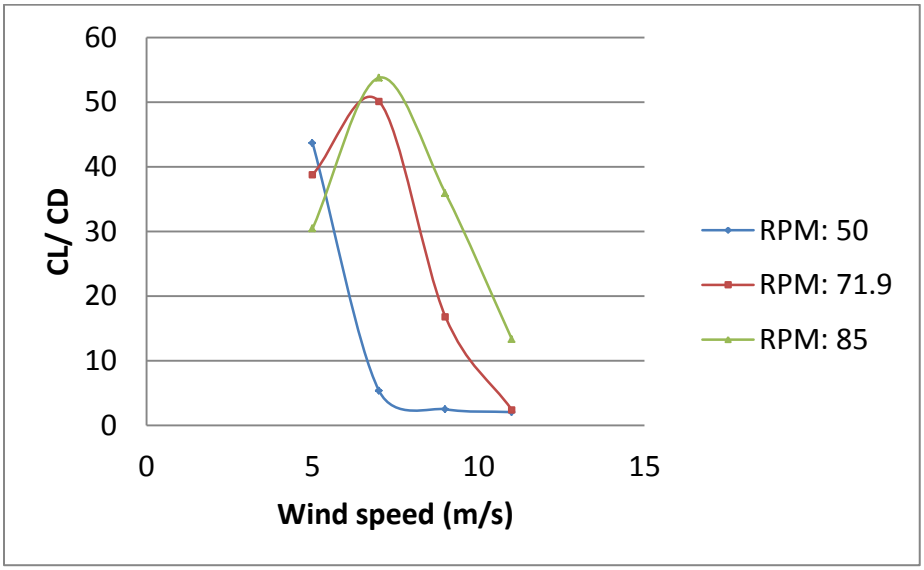

Figure 5-7: Aerodynamic efficiency vs. wind speed for different RPM valued

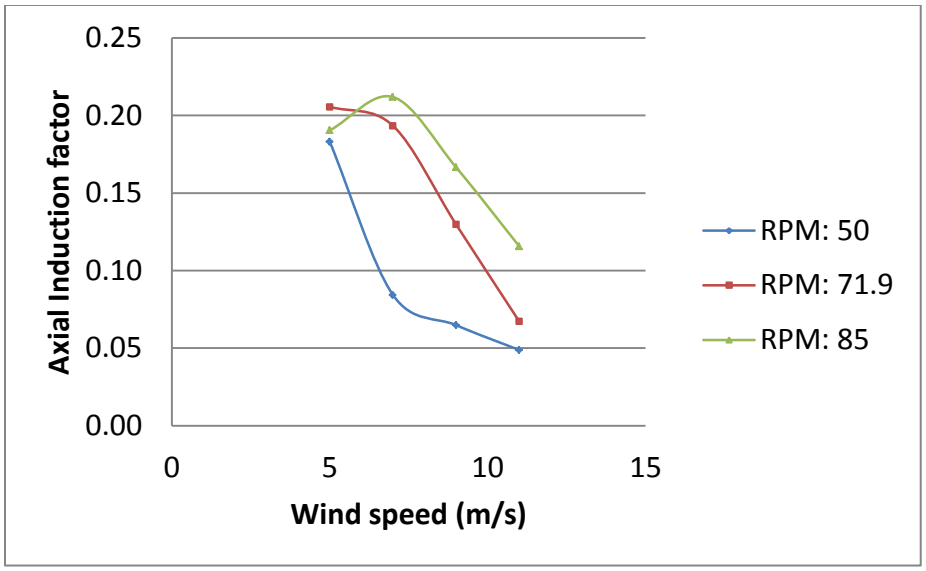

Figure 5-8: The axial induction factor *a* vs. wind speed for different RPM valued

We expect that as the wind speed increases, the angle of attack, α, should also increase. Generally α increases linearly between 0˚ and 15˚ - 20˚ after which stalling occurs. At stall, there is significant increase in drag with a reduction in lift. The plots above helps to illustrate this general trend. Studies have shown that during regular operation a wind turbine, they often operate in a dynamic stall state. One effect of dynamic stall is to delay the onset of stalling to a higher α value than for static aerodynamic conditions (Leishman 2002). FAST uses a semi-empirical model: the Beddoes-Leishman model which was initially developed to analyze dynamic stall in helicopters.

5.3 Effects of RPM

From the FAST simulations and results in Figure 5-9 to Figure 5-14 we observe that:

- Power increased with increase in RPM, and the magnitude increased with increasing pitch angles. However, from my simulations, at a pitch of 10˚ there was a significant drop in power after an RPM of about 50.

- For low RPMs, more favorable C_L results were obtained at a mid-range pitch angle, and at higher RPMs. A lower angle generated better results. At pitch angle of 10˚ as the RPM increased there is a significant drop in C_L.
- The C_D reduced with increasing RPM, but approached a constant value at high RPMs. Also, it should be noted that the magnitude of C_D reduced with increasing pitch angle.
- *Cp* varied in a similar manner to the power.
- The angle of attack, α, reduced with increasing RPM, and the magnitude of α reduced with increase in the pitch angle.
- The C_L/C_D ratio is also plotted for a fixed wind speed, and pitch. The changes in α are achieved by changing the RPM of the wind turbine. Similar trends to those observed in Section 5.2 are seen.

Note: The graphs below simulate a wind turbine with steady inflow wind speed of 7m/s and a nacelle yaw angle of 0 deg. The graphs show the effects of RPM on different parameters at three different pitch angles: 4.815, 6 and 10˚.

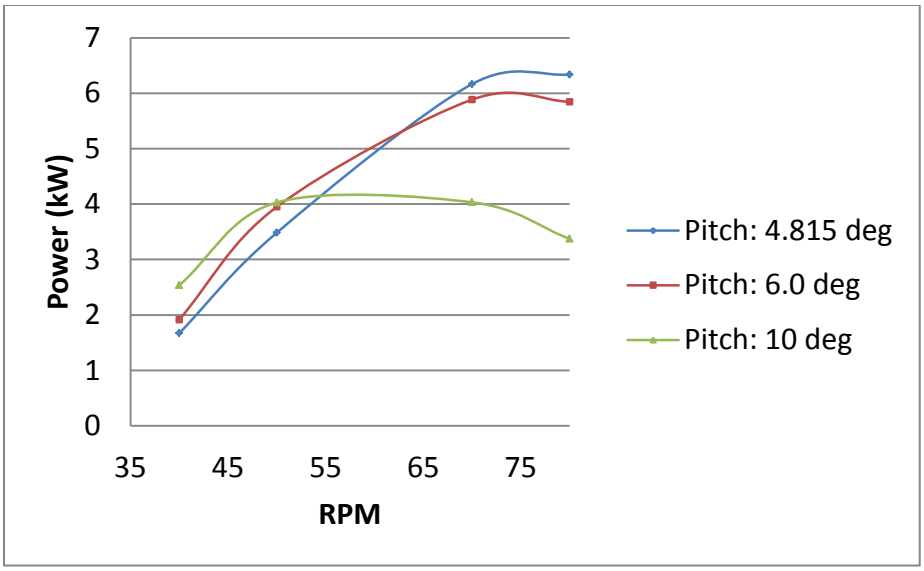

Figure 5-9: Plot of power against RPM for different pitch angles

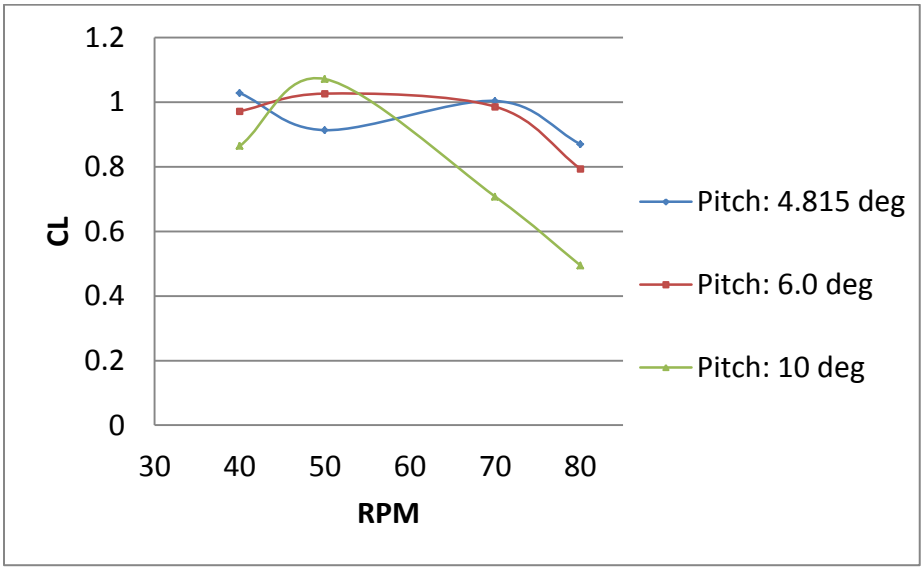

Figure 5-10: C_L vs. RPM for different RPM and pitch angles

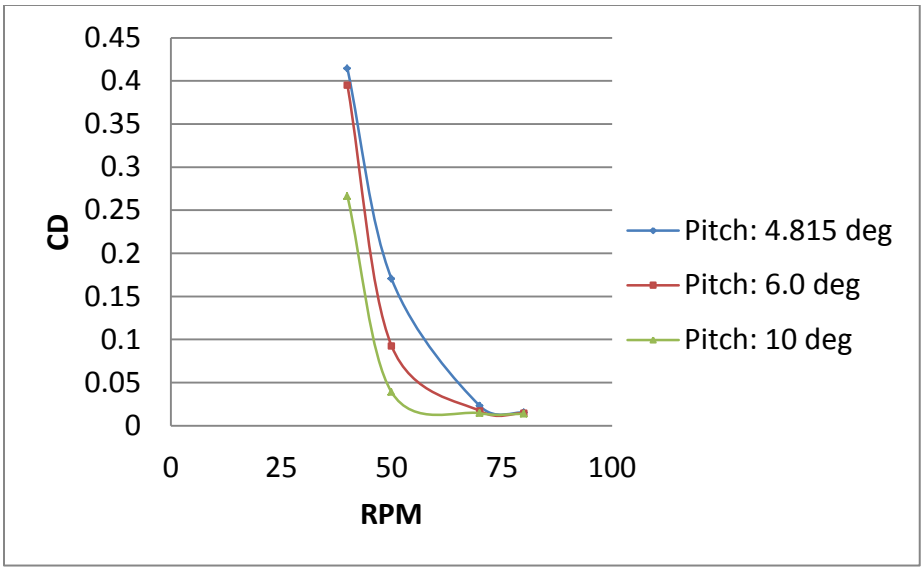

Figure 5-11: C_D vs. RPM for various RPMs and various pitch angles

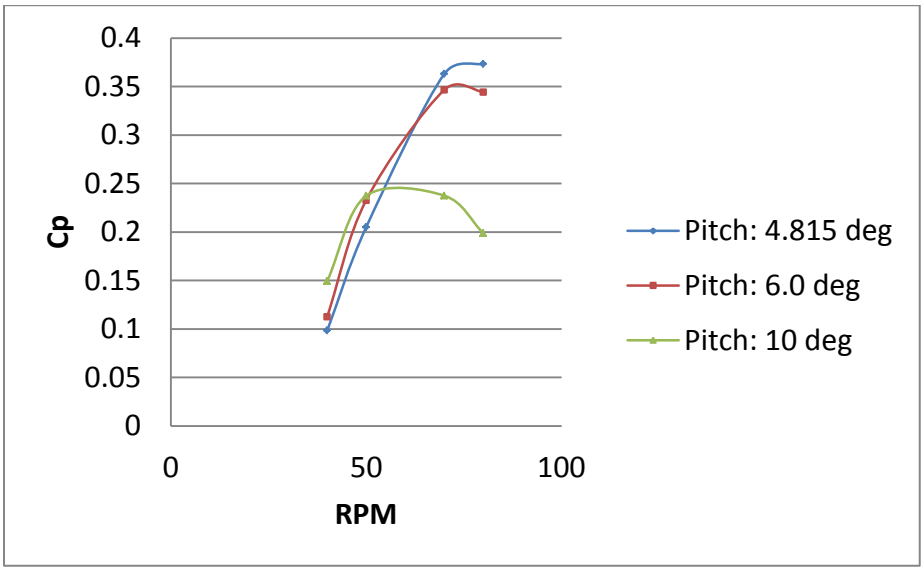

Figure 5-12: *Cp* vs. RPM for different pitch angles

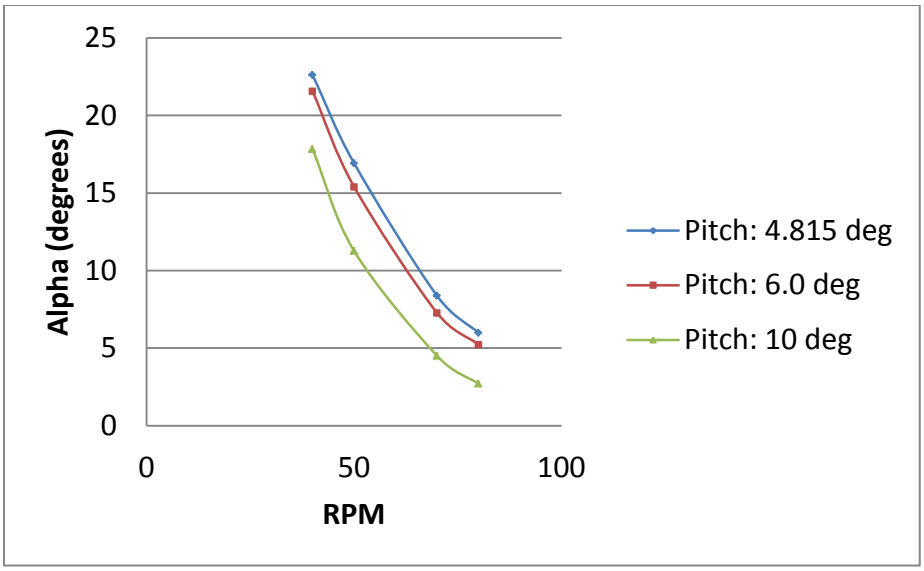

Figure 5-13: Plots of angle of attack, α, vs. RPM for different pitch angles

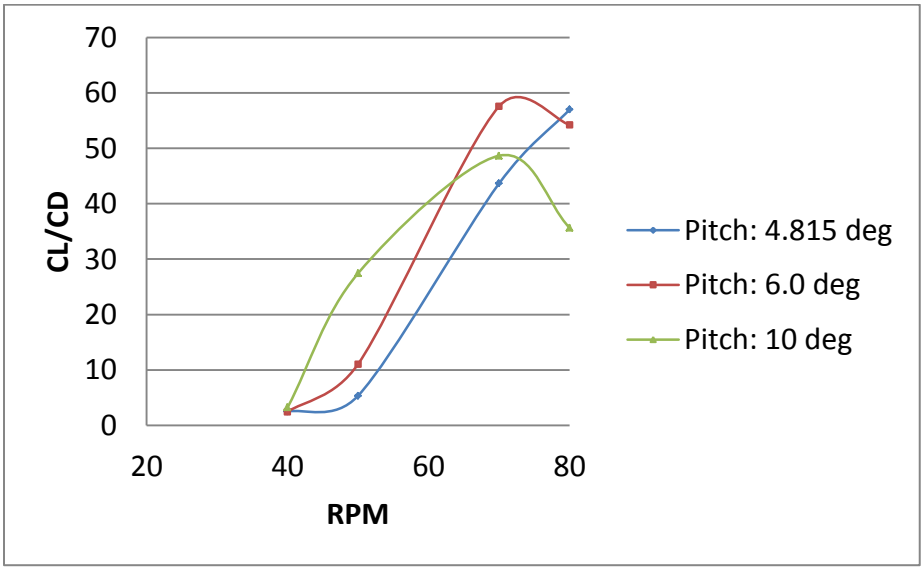

Figure 5-14: C_L/C_D ratio for various RPM values at different pitch angles

From the actuator disk theory for HAWTs, the torque on each annular ring is given by the change in angular momentum. The change in angular momentum is obtained by multiplying the mass flow rate, the change of tangential velocity and the radius of the turbine. The toque per annular ring is represented by δQ and is calculated as:

$$\delta Q = \rho \delta A_{CS} V_{\infty} (1-a) 2\Omega a' r^2 \qquad \text{Eq. 5.1}$$

From this equation we see that the torque of a wind turbine should increase linearly with the RPM. The power generated relates to torque as:

$$Power = Torque \times 2\pi \times RPM \qquad \text{Eq. 5.2}$$

The power per annular ring is δP, then,

$$\delta P = \rho \delta A_{CS} V_{\infty} (1-a) 2\Omega^2 a' r^2 \qquad \text{Eq. 5.3}$$

This tells us that the power (and Cp) increases with the squared of RPM. This we seen in Figure 5-9.

5.4 Effects of Pitch Angle

From the FAST simulations and results in Figure 5-15 to Figure 5-20 we can observe that:

- Power reduced with increasing pitch angles. The magnitude increased with increase in wind speed. However, at a wind speed of 11 m/s the power did increase with increasing pitch angles, until about 10˚, before it leveled out and began to decrease.
- C_L reduced for increasing pitch angle, and the magnitude increased with increasing wind speeds. There was an exception for the wind speed at 11 m/s, where the C_L increased

with increasing pitch angle.

- C_D reduced with increasing pitch angle and the magnitude increased with increase in wind speed.
- *Cp* reduced with increase in pitch angle. Again an exception was at the wind speed of 11 m/s were *Cp* increased with increasing pitch.

The angle of attack decreased with increasing pitch angle. *Note: The graphs below simulate a wind turbine with a constant RPM of 71.9 and a nacelle yaw angle of 0˚. The graphs show the effects of pitch angle on different parameters at three different wind speeds: 6, 9, and 11 m/s.*

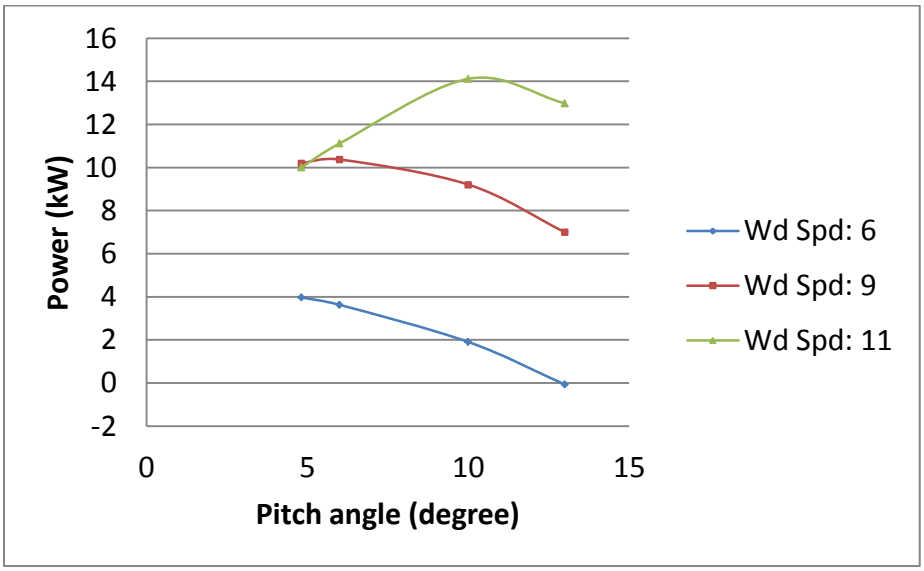

Figure 5-15: Power vs. pitch angle for different wind speeds

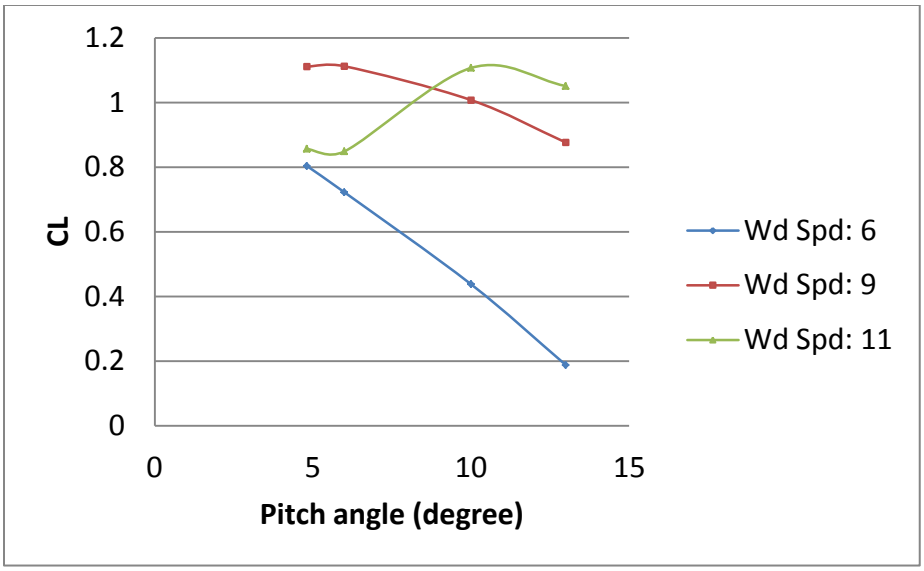

Figure 5-16: C_L vs. blade pitch angle for different wind speeds

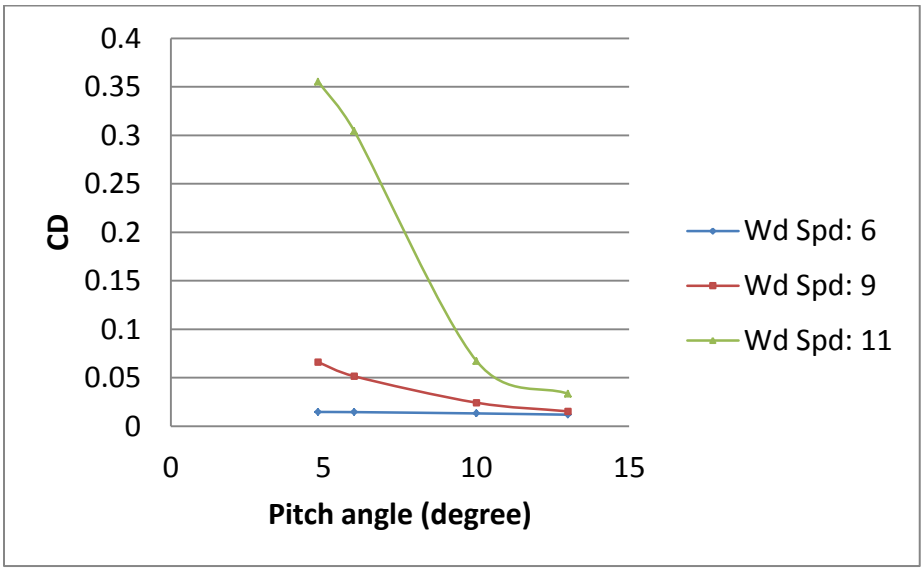

Figure 5-17: C_D vs. the blade pitch angle for different wind speeds

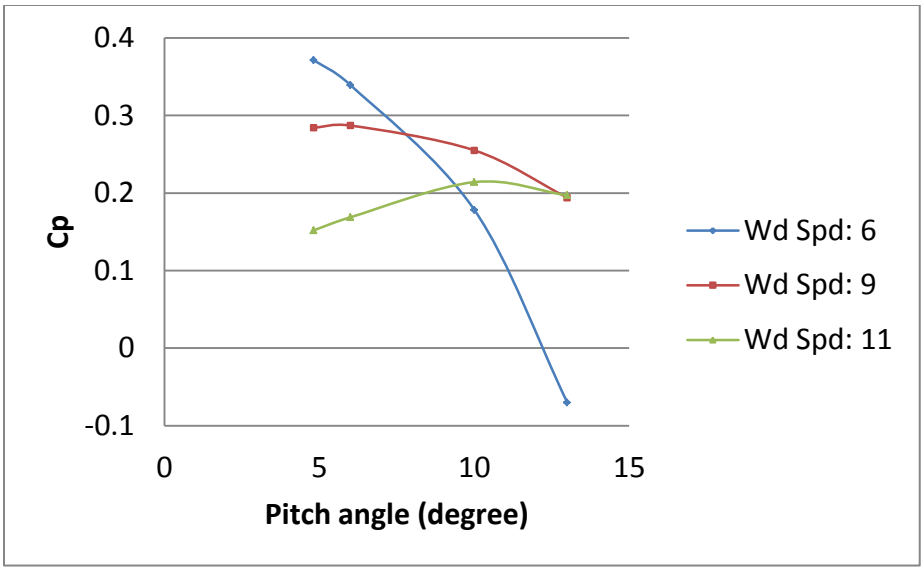

Figure 5-18: *Cp* vs. blade pitch angle for different wind speeds

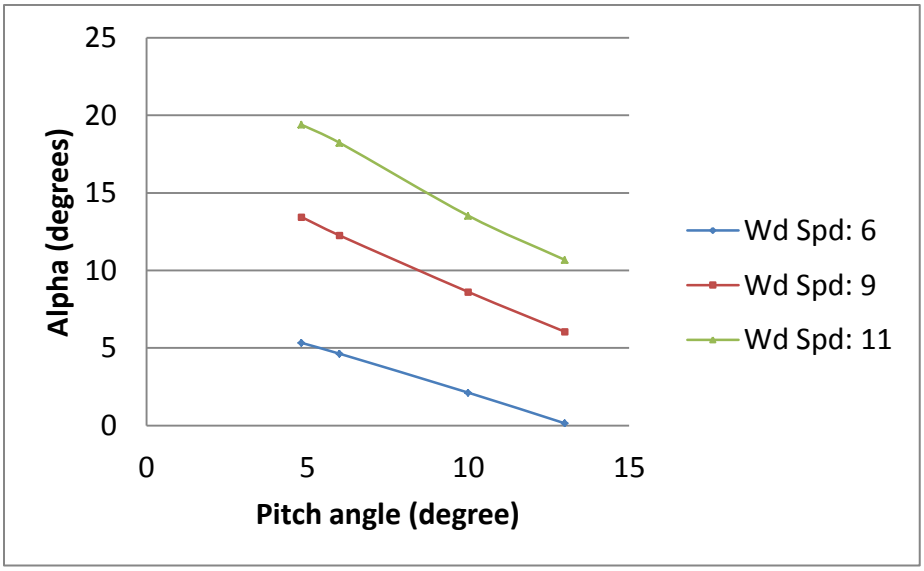

Figure 5-19: Angle of attack vs. blade pitch angle for different wind speeds

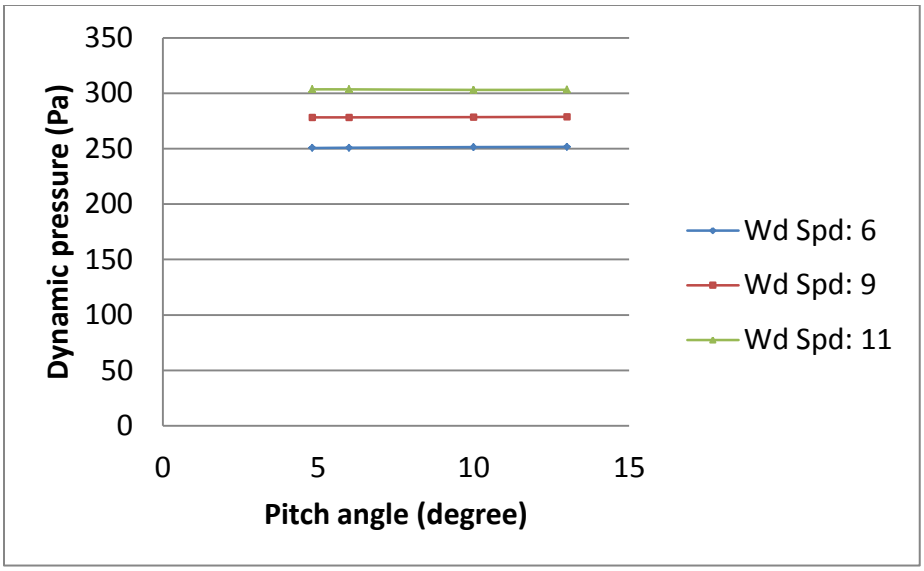

Figure 5-20: Dynamic pressure vs. pitch angle

5.5 Variation of Parameters along the Blade Span

This section presents the results of the spanwise variation of the aerodynamic parameters.

The effects of blade pitch angle:

The results of the effects of pitch angle on the spanwise parameters are presented in Figure 5-21 to Figure 5-28.

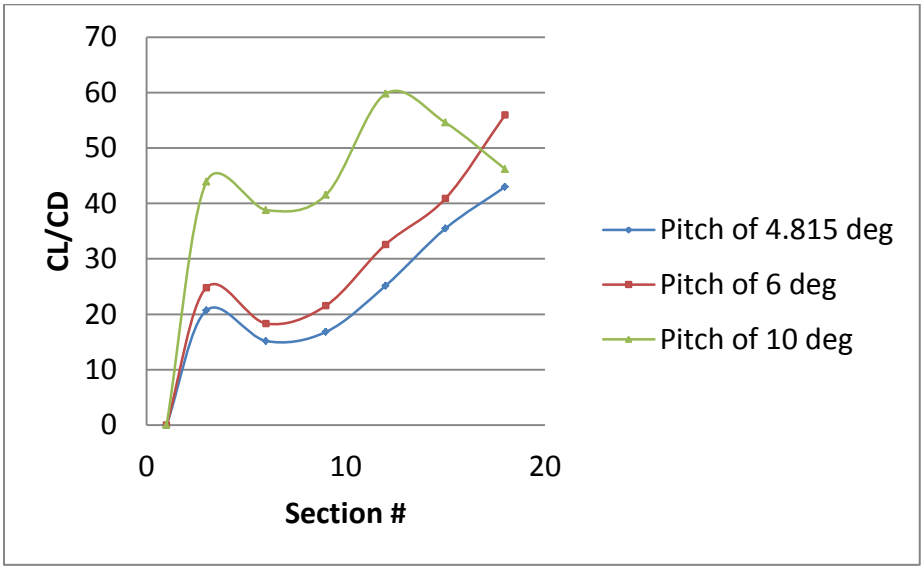

Figure 5-21: The $C_{L/}\ C_D$ ratio at the different sections of the blade

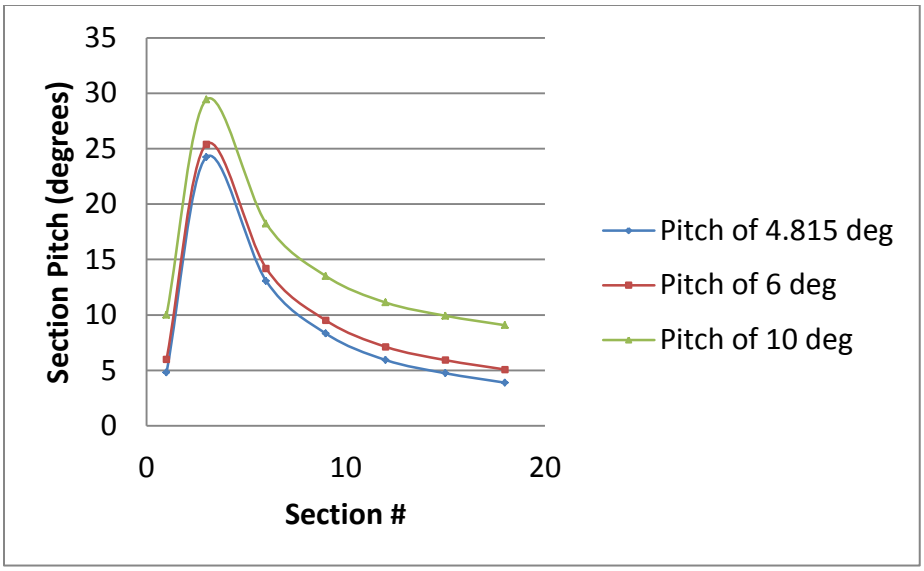

Figure 5-22: Section pitch angle at the different sections of the blade

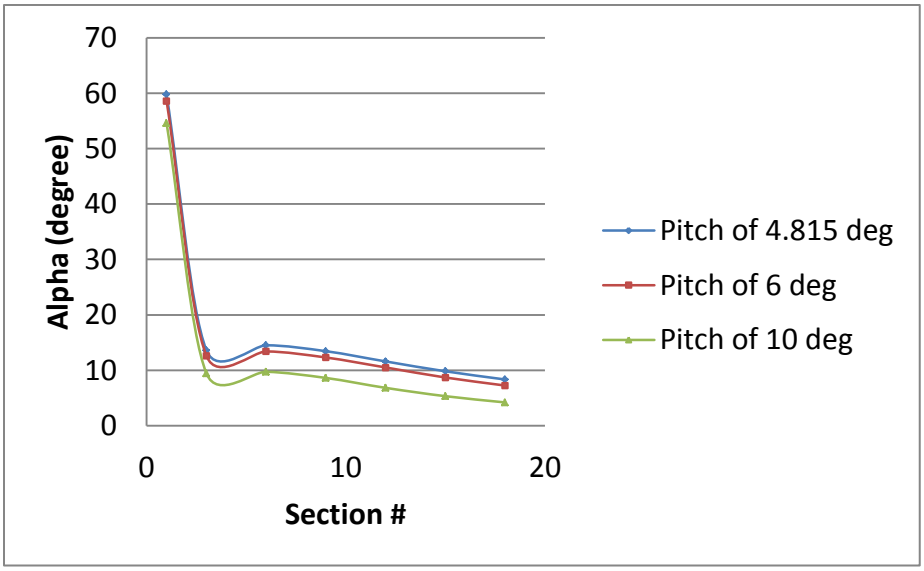

Figure 5-23: The angle of attack at the different sections of the blade

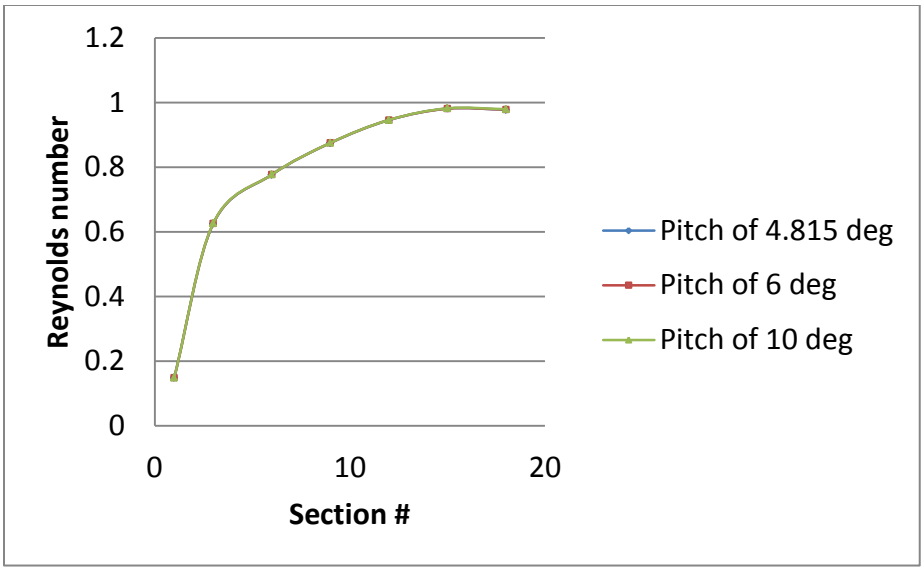

Figure 5-24: Re at the different sections of the blade

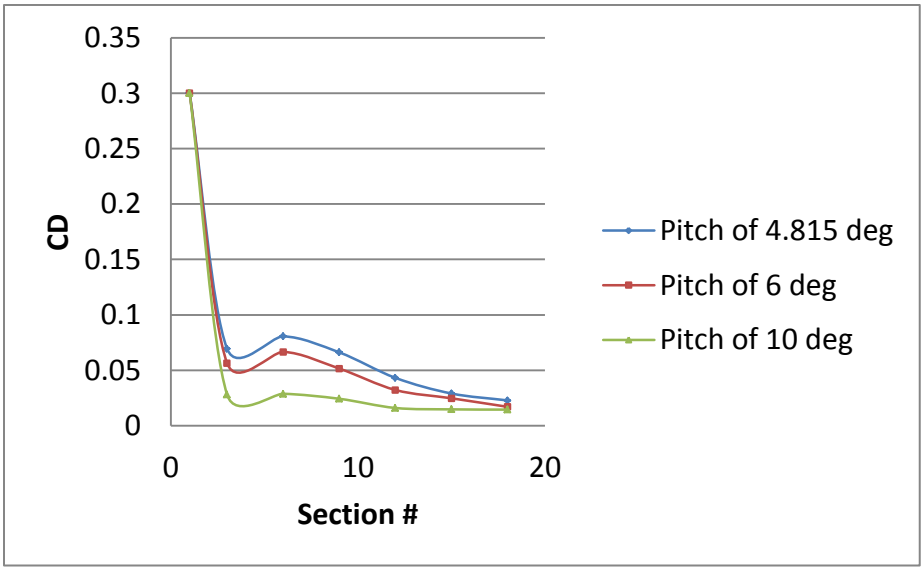

Figure 5-25: C_D at the different sections of the blade

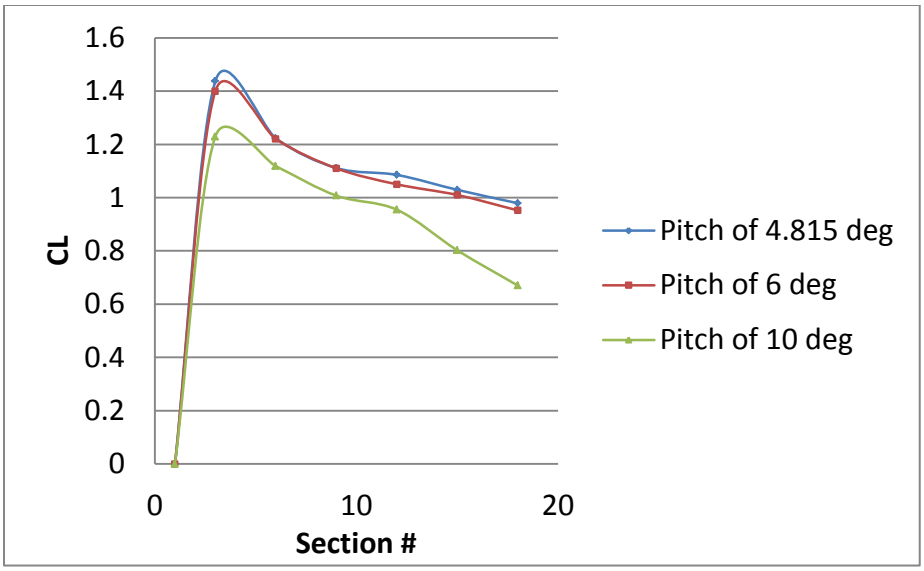

Figure 5-26: C_L at the different sections of the blade

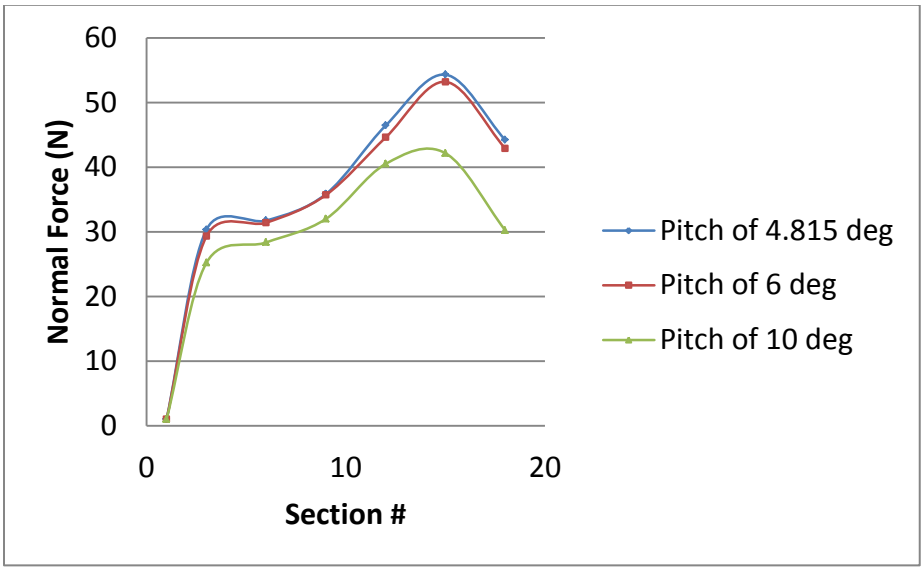

Figure 5-27: Normal force at the different sections of the blade

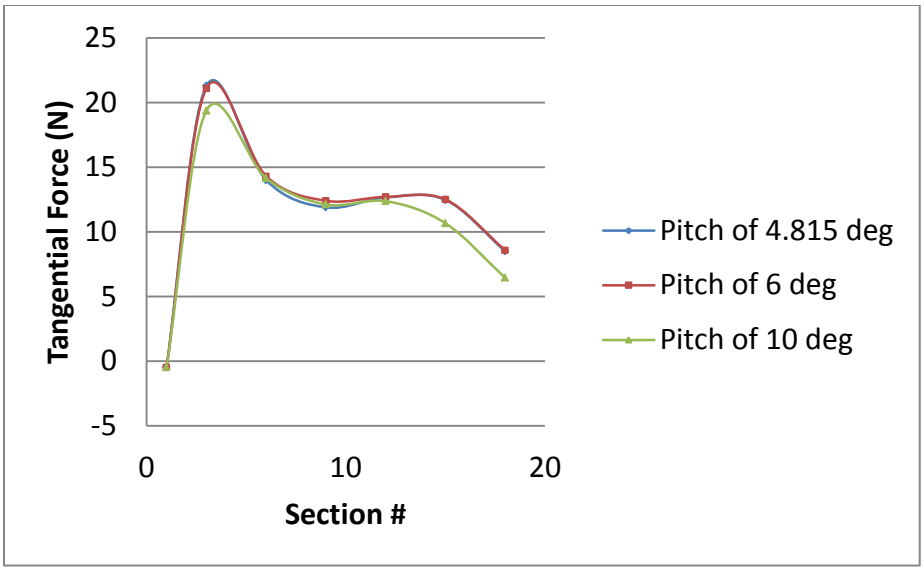

Figure 5-28: Tangential force at the different sections of the blade

The Effects of Wind speed:

The results of the effects of wind speed on the spanwise parameters are presented in Figure 5-29 to Figure 5-35.

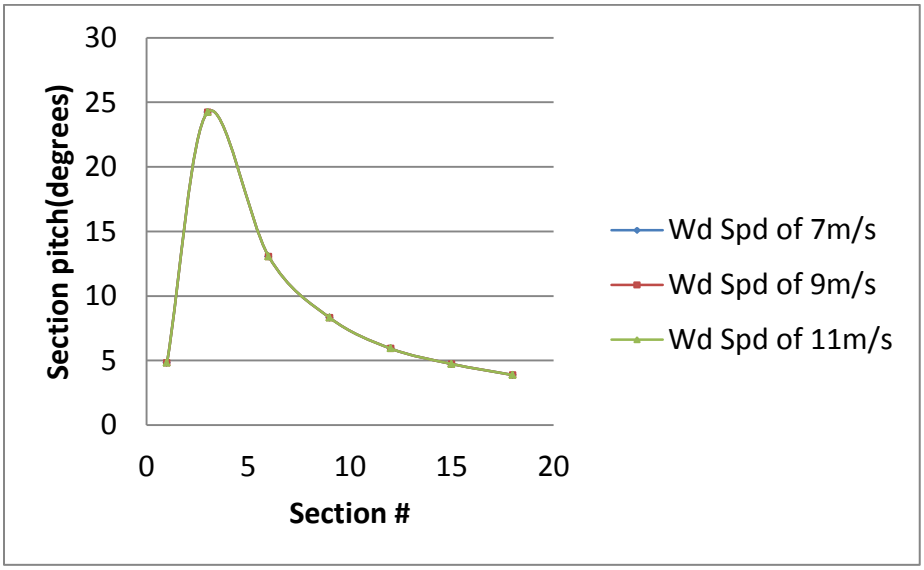

Figure 5-29: Section pitch angle at the different sections of the blade

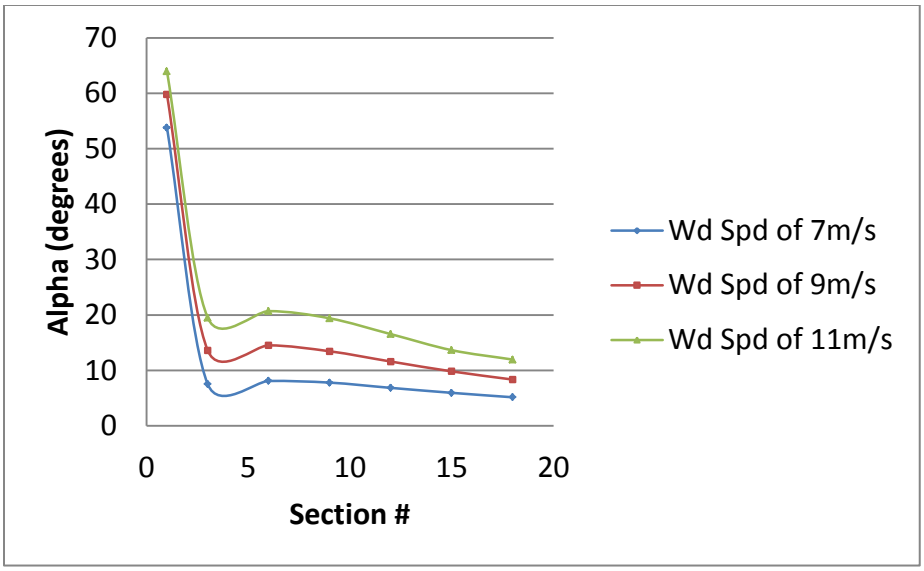

Figure 5-30: Angle of attack at the different sections of the blade

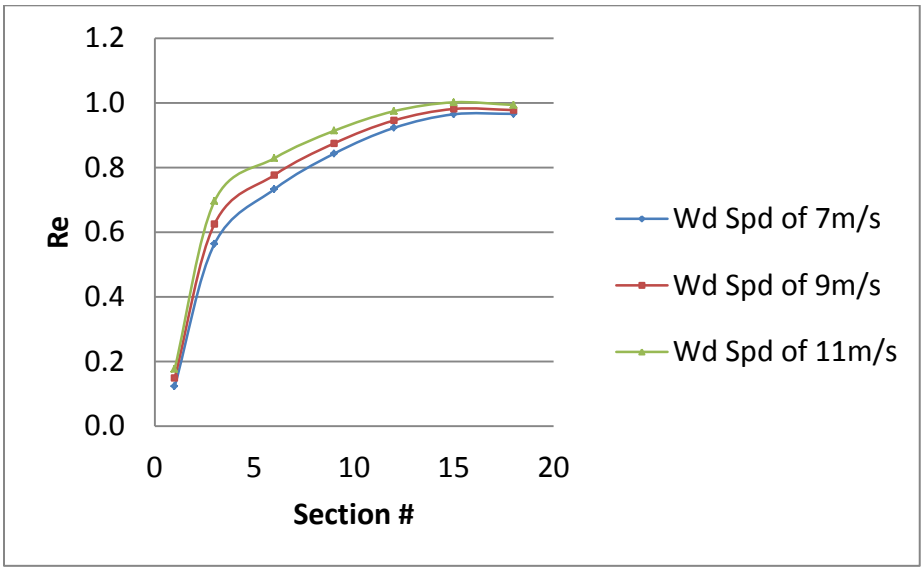

Figure 5-31: Re at the different sections of the blade

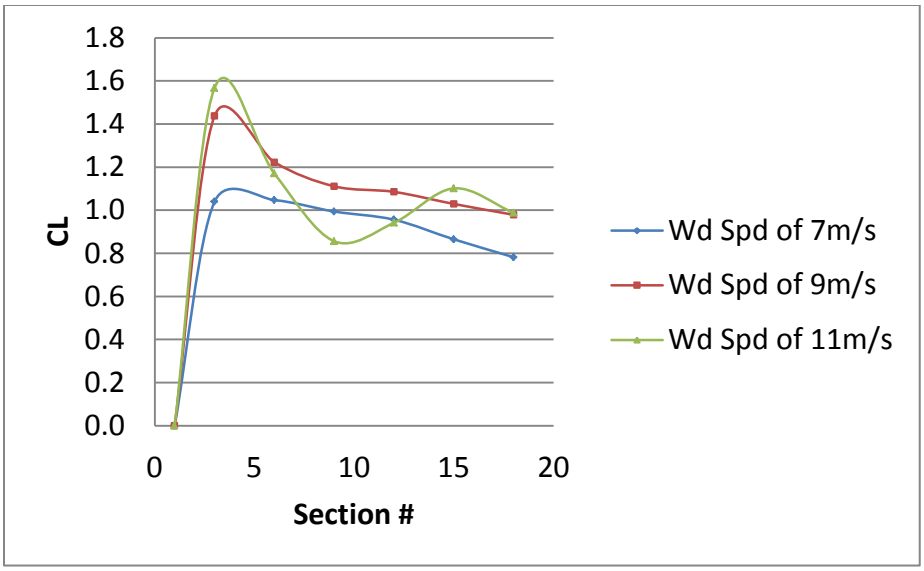

Figure 5-32: C_L at the different sections of the blade

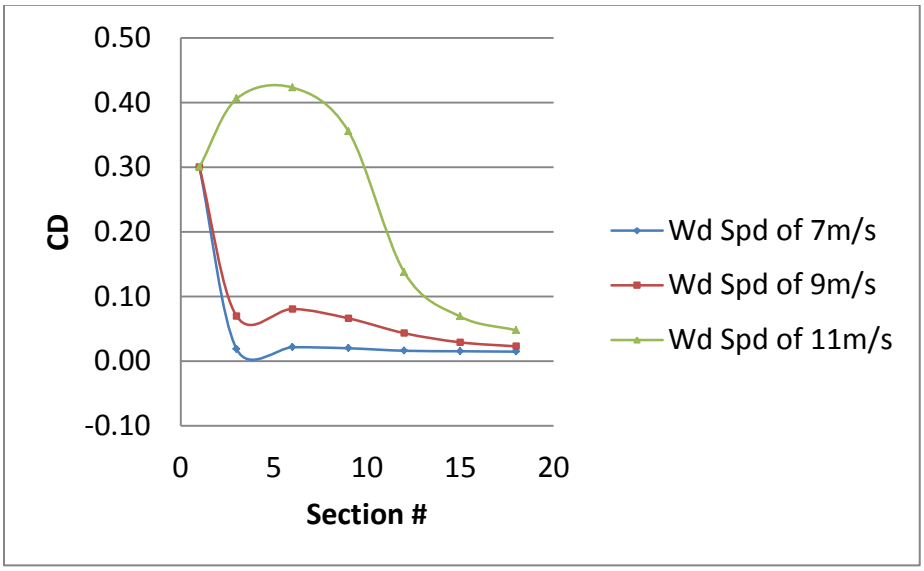

Figure 5-33: C_D at the different sections of the blade

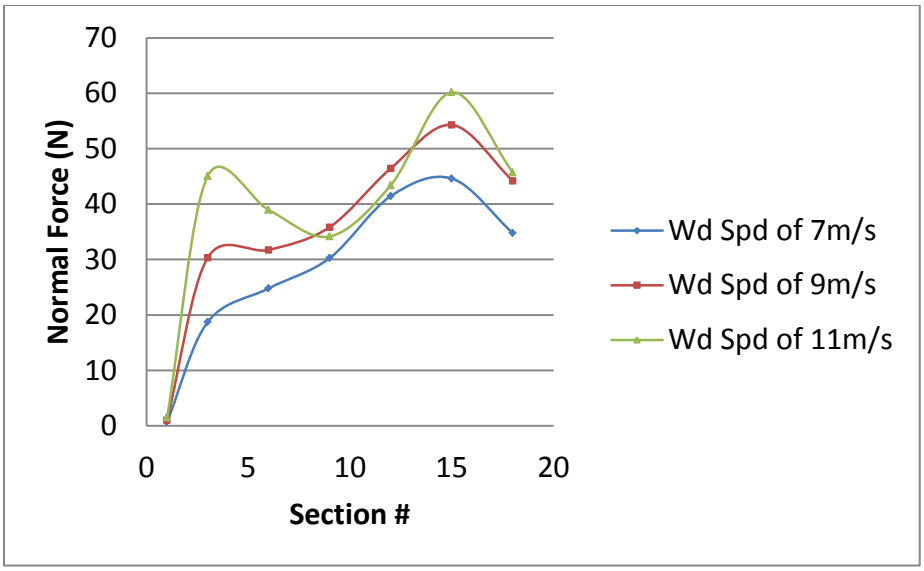

Figure 5-34: Normal force at the different sections of the blade

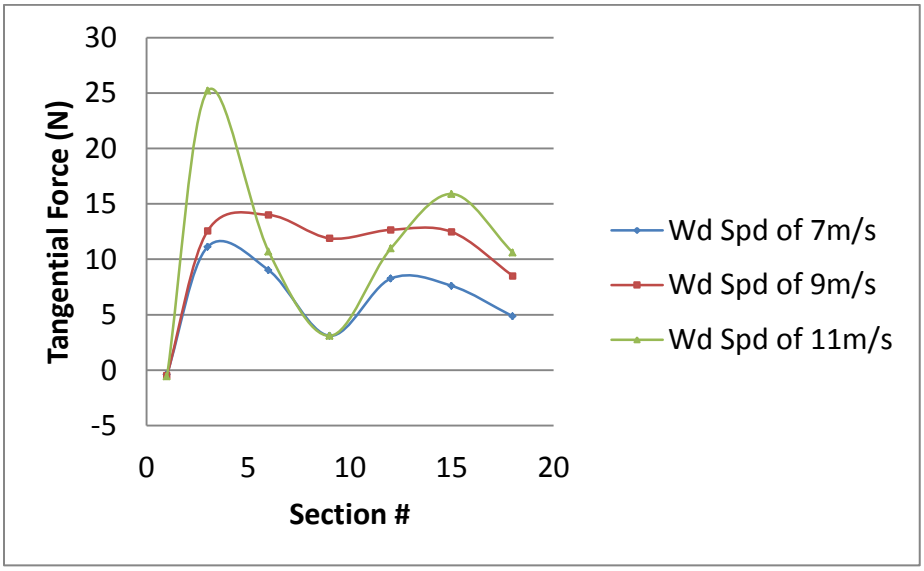

Figure 5-35: Tangential force at the different sections of the blade

Effects of RPM:

The results of the effects of RPM on the spanwise parameters are presented in Figure 5-36 to Figure 5-42.

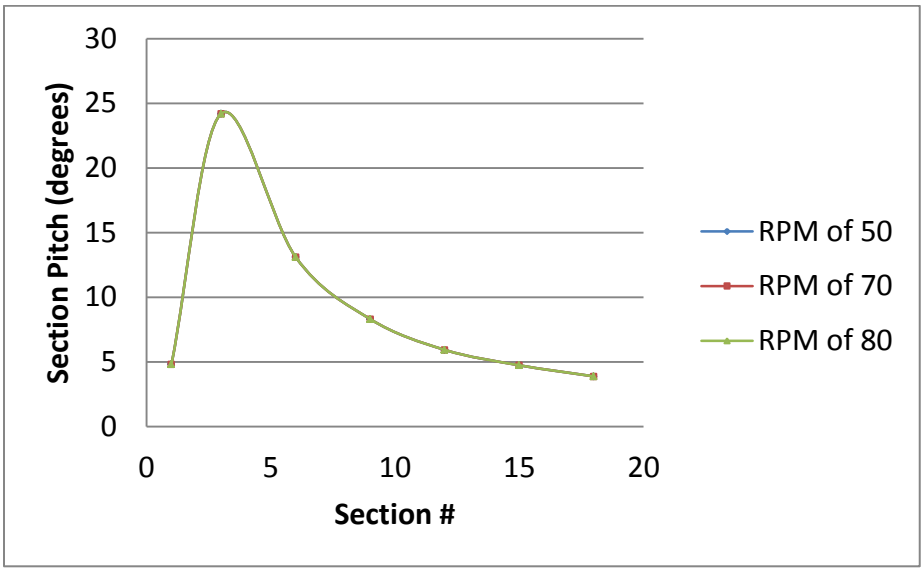

Figure 5-36: Section pitch at the different sections of the blade

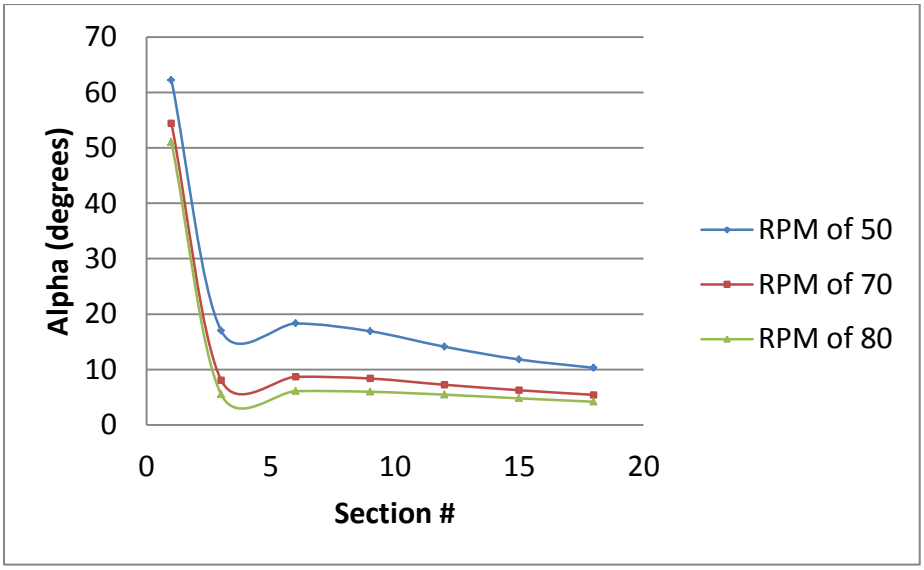

Figure 5-37: Angle of attack at the different sections of the blade

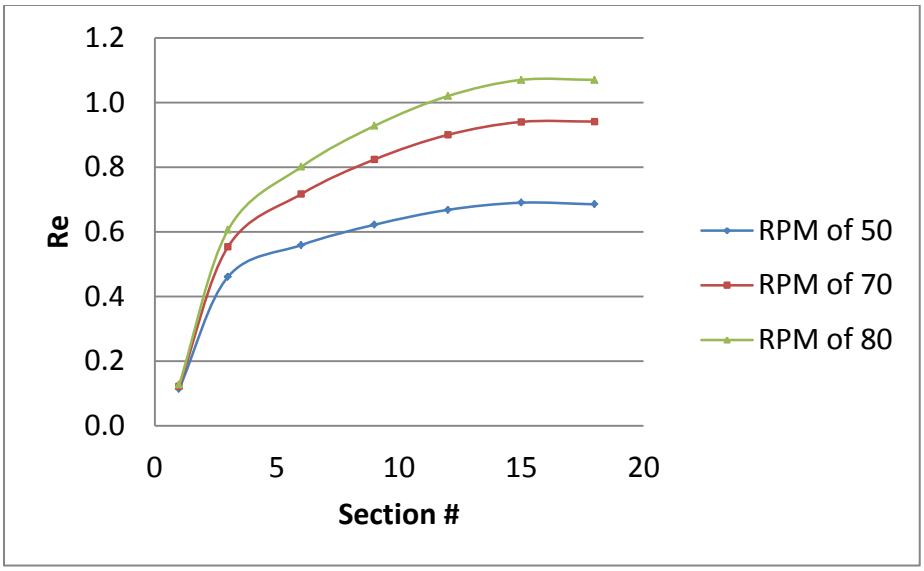

Figure 5-38: Re at the different sections of the blade

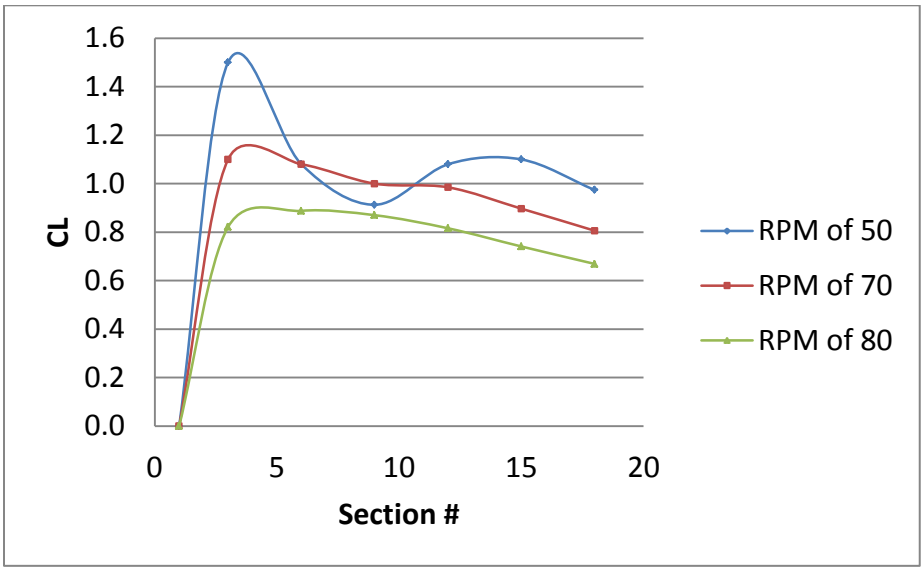

Figure 5-39: C_L at the different sections of the blade

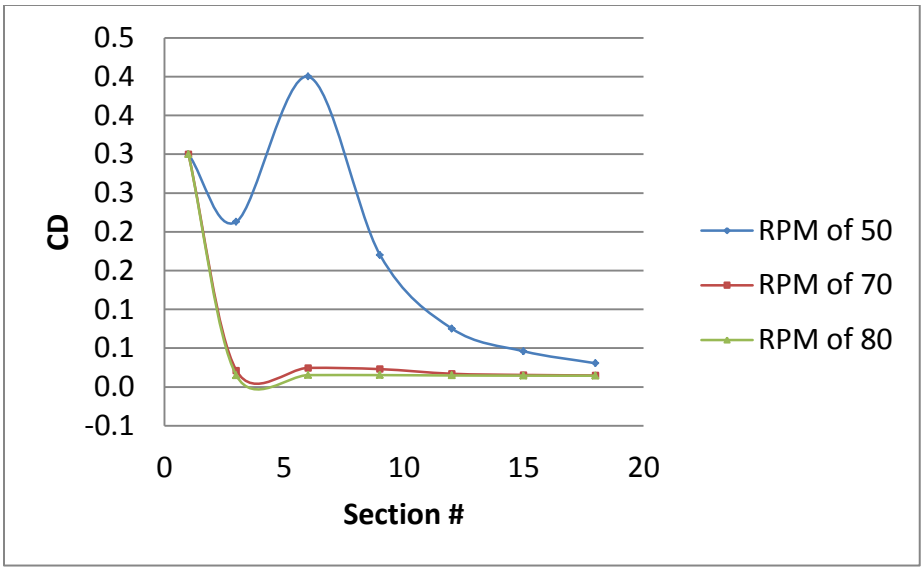

Figure 5-40: C_D at the different sections of the blade

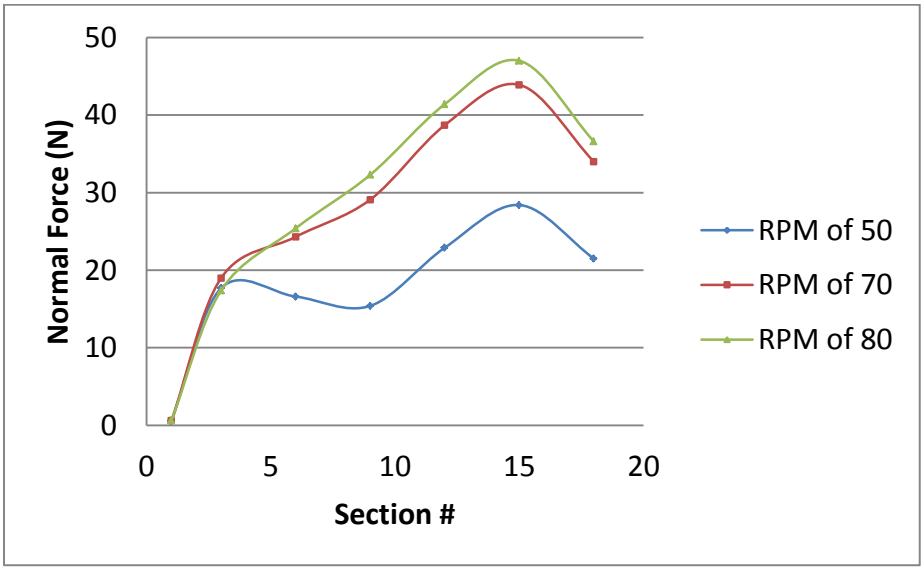

Figure 5-41: Normal force at the different sections of the blade

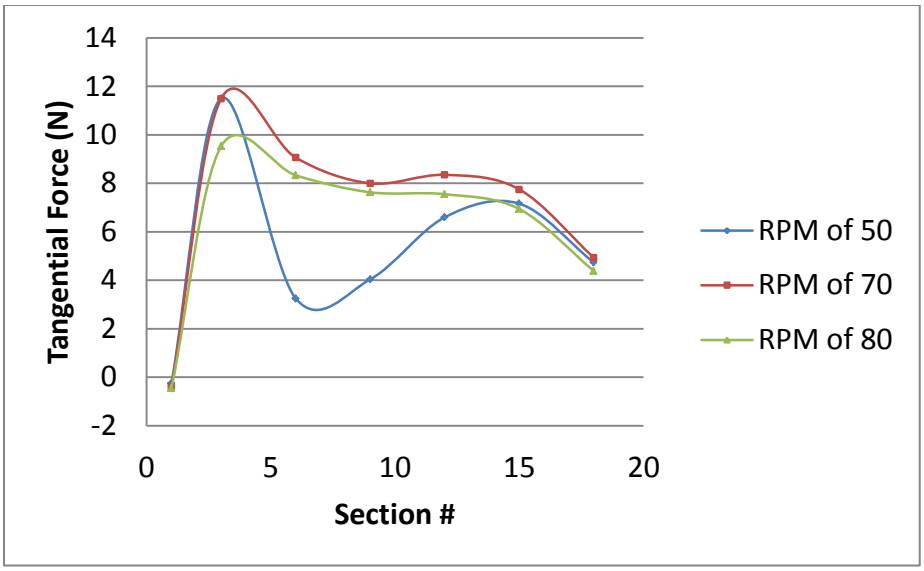

Figure 5-42: Tangential force at the different sections of the blade

Chapter 6: Summary and Conclusions

This research is focused on the aerodynamic analysis of horizontal and vertical axis wind turbines. The effects of the parameters that affect the performance of VAWTs has been studied both globally and in-depth to understand some physical features of how these turbines operate. Some key points have been made on how the torque characteristics affect the startup behavior and power production.

As part of this research, a computational model has been developed to qualitatively study, the behavior of VAWTs; the results presented are based on the outputs of this model. The model was developed and applied to study VAWTs in order to enhance the knowledge and understanding of their aerodynamics and how various operating parameters will affect the efficiency and power produced. Both fixed pitch and variable pitch blades are considered. From the variable pitch results we can conclude that the problem of self-start can be solved by developing new mechanisms. This research has provided a new and unique way of achieving the first step in developing efficient VAWTs. A variable pitch system, both for improved self-start capabilities and improved power generation will help the wind industry to advance turbine designs. Some of the conclusions made from the results are presented below:

- The results show that more research is needed to characterize the Reynolds number for wind turbines. The selection of the Re significantly affects the accuracy of the simulation results, whether a momentum or vortex model is used, as C_L and C_D data are very sensitive to Re. For example, in the equation of Re, the numerator has a length quantity (the characteristic length of the flow), flow visualization experiment is needed to

understand what length (blade chord length, or rotor diameter, etc.) best represents that of a turbine.

- Empirical models which take into consideration the transient nature of wind turbines are necessary to better understand the turbine's torque performance. Knowing how much torque is generated at every azimuthal angle with time will help in understanding how turbines start, and will assist in the development of proper control systems for the optimized machines.
- The success of any empirical model for wind turbines depends on the accuracy of lift and drag property data for the flow conditions experienced. More experiments are needed for variable angle of attack blades. Currently, most empirical models use property data from steady-state static experiments; however, the flow conditions seen by a VAWT are significantly different because of the turbine's rotational velocity, its blade's orientation and how it interacts with the wind, and the fact that at every azimuthal angle, the blade angle of attack changes. The results presented in this thesis, although they consider changes in flow conditions, the underlying data tables they use were unchanged which may lead to errors in results. Results from the variable pitch blade will especially benefit unsteady C_L and C_D data because of the very complicated flow structures that occurs by blade pitching. The results presented here may over-predict the power and efficiencies that are experienced by an actual turbine as the rapid changes which affect the flow structure may reduce the actual amount of lift and torque generated by a highly unsteady flow over the blade when compared to a static case.
- The cascade model considers circulation as one of its calculated variables; however, the assumption applied to simplify the problem may be inadequate to represent the physics

of circulation around the airfoil's profile. In essence, circulation in this model is calculated as a consequence of the inflow and outflow velocities parallel to the longitudinal section of the airfoil. What is therefore proposed is to use a similar formulation as presented in the theory section above; however, after the initial guess is made for V_d and the iteration process proceeds, instead of calculating the circulation (which is ultimately used to find the component of circulation velocity on the airfoil profile) based on those two velocity components, the panel method could be used to calculate it. In order to implement this, at every iteration of V_d a panel method subroutine may be called to calculate the circulation around the airfoil, given the flow conditions; the resulting value of circulation which satisfies the Kutta-Joukowski theorem is then applied to more accurately calculate V_Γ, the velocity due to circulation in the cascade. This approach is proposed because the panel method would serve as a better model in predicting the circulation, thus improving the overall performance of the cascade theory. A drawback to this approach will be the poor performance of the panel method at stall angles.

- The model used in analysis does not consider the interactions of one blade on another, hence the assumption of a reference blade being selected and the other blades are assumed to have similar aerodynamic characteristics. It is believed that for a more complete analysis the effects of one blade which alters the flow conditions for other blades needs to be considered.
- Ultimately, in order to better understand the basic flow physics for wind turbines, a computational fluid dynamics (CFD) approach is necessary.

HAWT, FAST results show significant effects of the flow/ turbine parameters on turbine power and efficiency.

Bibliography

Bibliography

American Wind Energy Association. n.d. http://www.awea.org/faq/vawt.html (accessed 2011).

Anderson Jr., John D. *Fundamentals of Aerodynamics.* McGraw-Hill Higer Education, 2001.

Bhimarasetty, Aravind, and Raghuraman N. "A simple method for potential flow simulation of cascades." *Indian Academy of Sciences*, 2010: 649–657.

Brownlee, Baron Gene. *A Vortex Model for Vertical Axis Wind Turbine.* Thesis, n.d.

Burton, Andy, David Sharpe, Nick Jenkins, and Ervin Bossanyi. "Wind Energy Handbook." 1. Wiley, 2001.

Dominy, R., P. Lunt, A. Bickerdyke, and J. Dominy. "Self-starting capability of a Darrieus turbine." *Proceedings of the Institute of Mechanical Engineers, Power and Energy, Volume 221, Part A.* n.d.

Ebert, P. R., and D. H. Wood. "Observations of the starting behaviour of a small horizontal-axis wind turbine." *Renew. Energy*, 1997: 12(3), 245–257.

Giguère, P., and M.S. Selig. *Design of a Tapered and Twisted Blade for the NREL Combined Experiment Rotor.* Subcontractor Report: National Renewable Energy Laboratory, 1999.

Hirsch, H, and A.C. Mandal. "A cascade theory for the aerodynamic performance of Darrieus wind turbines." *Wind Engineering*, 1987: 164-75.

Islam, Mazharul, David S.K., and Amir Fartaj Ting. "Aerodynamic models for Darrieus-type straight-bladed vertical axis wind turbines." *ScienceDirect* (ScienceDirect), 2008.

Jose, Zayas. "Wind Energy: Background, Technology, Opportunities, and Material Challenges; Sandia National Laboratories, 2010 Material Challenges in Alternative & Renewable Energy." 2010. http://ceramics.org/wp-content/uploads/mcare/wind_zayas.pdf (accessed 2011).

Kirke, B.K. *Evaluation of self-starting vertical axis wind turbines for stand-alone applications. PhD thesis.* Griffith University, Australia, 1998.

Leishman, J.G. *Challenges in Modeling the Unsteady Aerodynamics of Wind Turbines.* Maryland: AIAA, 2002.

Lunt, P. A. V. *An aerodynamic model for a vertical-axis wind turbine.* UK: MEng project report, School of Engineering, University of Durham, 2005.

Malcolm, D.J., and A.C. Hansen. *WindPACT Turbine Rotor Design Study.* NREL report, 2006.

Malcolm's Human Powered Aircraft Site. n.d. www.library.propdesigner.co.uk/index.html.

Mandal, A.C., and J.D. Burton. "The effects of dynamic stall and flow curvature on the aerodynamics of Darrieus turbines applying the Cascade model." *Wind Eng 1994*, 1994: 267 - 82.

Manwell, James F., Jon G. McGowan, and Anthony L. Rogers. In *Wind Energy Explained: Theory, Design and Application*, 10. Wiley, 2002.

McCroskey, W. J., K. W. McAlister, L.W. Carr, S. L. Pucci, O. Lambert, and R. F. Indergrand. "Dynamic Stall on Advanced Airfoil Sections." *Presented at 36th Annual forum and Technology Display of American Helicopter Society (Washington, D.C.).* 1980.

Migliore, P.G., Wolfe W.P., and Fanucci J.B. "Flow Curvature Effects on Darrieus Turbine Blade Aerodynamics." *Journal of Energy Vol. 4, No. 2*, 1980.

Noll, R.B, and N.D. "Dynamic Stall of Small Wind Systems." February 1983.

Paraschivoiu, I., O. Trifu, and F. Saeed. "H-Darrieus Wind Turbine with Blade Pitch Control." *Hindawi Publishing Corporation, International Journal of Rotating Machinery, Volume 2009, Article ID 505343*, 2009.

Paraschivoiu, Ion. "Double-multiple streamtube model for Darrieus wind turbines." *Second DOE/NASA wind turbines dynamics workshop NASA CP-2186.* Cleveland, OH,, 1981. 19 - 25.

Scholz., Prof. Dr-Ing. N. "Aerodynamics of Cascade." Neuilly sur Seine, France: Advisory Group for Aerospace Research and Development., n.d.

Staelens, Yann, F. Saeed, and I. Paraschivoiu. "A Straight-Bladed Variable-Pitch VAWT Concept for Improved Power Generation." *ASME 2003 Wind Energy Symposium* . Reno: ASME, 2003. 146-154.

Strickland, J.H. "A performance prediction model for the Darrieus turbine. International symposium on wind Energy Systems." Cambridge, UK, 1976. C3-39-59.

Swamy, Kmm, and R Senthil Kumaran. "Estimation of Turbomachinery Flow Losses Through Cascade Testing." Scientists Propulsion Division, National Aerospace Laboratories, 07 18, 2009.

Tangler, J, and J.D. Kocurek. "Wind Turbine Post-Stall Airfoil Performance Characteristics Guidelines for Blade-Element Momentum Methods." *NREL, 43rd AIAA Aerospace Sciences Meeting and Exhibit.* 2005.

Templin, R. *Aerodynamic Performance Theory for the NRC Vertical-Axis Wind Turbine.* Technical Report, National Aeronautical Establishment Laboratory Technical Report LTR- LA-160, National Research Council, 1974.

Templin, R.J. "Aerodynamic performance theory for the NRC vertical-axis wind turbine." *NRC Lab. Report LTR-LA-190.,* 1974.

The Engineering Toolbox: Wind Shear. n.d. http://www.engineeringtoolbox.com/wind-shear-d_1215.html.

UIUC Airfoil Data Site. n.d. www.ae.illinois.edu/m-selig/ads/coord_database.html.

Wilson, R.E., and P.B.S. Lissaman. *Applied aerodynamics of wind power machhines.* Oregon State University., 1974.

Worstell, W.H. *Sandia Report: Aerodynamic Performance of the 17 Meter Diameter Darrieus Wind Turbine.* Sandia National Laboratory, 1978.

Yao, Yingxue, and B. Habbtamu. "Effects of Camber Airfoil on Self-Starting of Vertical Axis Wind Trubines." *Journal of Environmental Science and Technology, Volume 4, No. 2*, n.d.